

SANDIA REPORT

SAND2007-6191
Unlimited Release
Printed October 2007

The mechanics of soft biological composites

B.L. Boyce, J.M. Grazier, R.E. Jones, and T.D. Nguyen

Prepared by
Sandia National Laboratories
Albuquerque, New Mexico 87185 and Livermore, California 94550

Sandia is a multiprogram laboratory operated by Sandia Corporation,
a Lockheed Martin Company, for the United States Department of Energy's
National Nuclear Security Administration under Contract DE-AC04-94-AL85000.

Approved for public release; further dissemination unlimited.

Issued by Sandia National Laboratories, operated for the United States Department of Energy by Sandia Corporation.

NOTICE: This report was prepared as an account of work sponsored by an agency of the United States Government. Neither the United States Government, nor any agency thereof, nor any of their employees, nor any of their contractors, subcontractors, or their employees, make any warranty, express or implied, or assume any legal liability or responsibility for the accuracy, completeness, or usefulness of any information, apparatus, product, or process disclosed, or represent that its use would not infringe privately owned rights. Reference herein to any specific commercial product, process, or service by trade name, trademark, manufacturer, or otherwise, does not necessarily constitute or imply its endorsement, recommendation, or favoring by the United States Government, any agency thereof, or any of their contractors or subcontractors. The views and opinions expressed herein do not necessarily state or reflect those of the United States Government, any agency thereof, or any of their contractors.

Printed in the United States of America. This report has been reproduced directly from the best available copy.

Available to DOE and DOE contractors from
U.S. Department of Energy
Office of Scientific and Technical Information
P.O. Box 62
Oak Ridge, TN 37831

Telephone: (865) 576-8401
Facsimile: (865) 576-5728
E-Mail: reports@adonis.osti.gov
Online ordering: <http://www.osti.gov/bridge>

Available to the public from
U.S. Department of Commerce
National Technical Information Service
5285 Port Royal Rd
Springfield, VA 22161

Telephone: (800) 553-6847
Facsimile: (703) 605-6900
E-Mail: orders@ntis.fedworld.gov
Online ordering: <http://www.ntis.gov/help/ordermethods.asp?loc=7-4-0#online>



SAND2007-6191
Unlimited Release
Printed October 2007

The mechanics of soft biological composites

B.L. Boyce
Microsystems Materials Department
Sandia National Laboratories
P.O. Box 5800 - MS 0889
Albuquerque, NM 87123
blboyce@sandia.gov

J.M. Grazier
Microsystems Materials Department
Sandia National Laboratories
P.O. Box 5800 - MS 0889
Albuquerque, NM 87123
jmgrazi@sandia.gov

T.D. Nguyen
Mechanics of Materials Department
Sandia National Laboratories
P.O. Box 969 - MS 9409
Livermore, CA 94551
tdnguye@sandia.gov

R.E. Jones
Mechanics of Materials Department
Sandia National Laboratories
P.O. Box 969 - MS 9409
Livermore, CA 94551
rjones@sandia.gov

Abstract

Biological tissues are uniquely structured materials with technologically appealing properties. Soft tissues such as skin, are constructed from a composite of strong fibrils and fluid-like matrix components. This was the first coordinated experimental/modeling project at Sandia or in the open literature to consider the mechanics of micromechanically-based anisotropy and viscoelasticity of soft biological tissues. We have exploited and applied Sandia's expertise in experimentation and mechanics modeling to better elucidate the behavior of collagen fibril-reinforced soft tissues.

The purpose of this project was to provide a detailed understanding of the deformation of ocular tissues, specifically the highly structured skin-like tissue in the cornea. This discovery improved our knowledge of soft/complex materials testing and modeling. It also provided insight into the way that cornea tissue is bio-engineered such that under physiologically-relevant conditions it has a unique set of properties which enhance functionality. These results also provide insight into how non-physiologic loading conditions, such as corrective surgeries, may push the cornea outside of its natural design window, resulting in unexpected non-linear responses. Furthermore, this project created a clearer understanding of the mechanics of soft tissues that could lead to bio-inspired materials, such as highly supple and impact resistant body armor, and improve our design of human-machine interfaces, such as micro-electrical-mechanical (MEMS) based prosthetics. Through this study,

Keywords: biomechanics, bovine cornea, anisotropy, viscoelasticity

This page intentionally left blank.

Acknowledgment

We wish to thank Dr. Richard Regueiro (CU-Boulder) for providing the initial impetus and guidance for this work, Bob Chambers (SNL) for insight conversations on viscoelasticity, and Dr. Stephen D. McLeod (Department of Ophthalmology, UCSF), and Prof. Christine Wildsoet (Department of Vision Science, UCB) for helpful discussions regarding this project. We also wish to thank Dr. D. Bammann and Prof. R. Ogden for insightful discussions on continuum theories of modeling material anisotropy and inelasticity under finite-deformations. This work was funded by the Laboratory Directed Research and Development program at Sandia National Laboratories. Sandia is a multiprogram laboratory operated by Sandia Corporation, a Lockheed Martin Company, for the United States Department of Energy under contract DE-ACO4-94AL85000.

Contents

1	Introduction	15
2	Stress-Controlled Viscoelastic Tensile Response of Bovine Cornea	17
2.1	Introduction	17
2.2	Materials and Methods	18
2.3	Results	22
2.4	Discussion	26
3	A Nonlinear Viscoelastic Model for the Tensile Behavior of Bovine Cornea	33
3.1	Introduction	33
3.2	Method	36
3.2.1	Model Formulation	36
3.2.2	Flow rate	41
3.2.3	Parameter Fitting	42
3.3	Results of Uniaxial Tensile Simulations	45
3.4	Discussion	49
4	Modeling the Anisotropic Finite-Deformation Viscoelastic Behavior of Soft Fiber-Reinforced Composites	53
4.1	Introduction	53
4.2	Model Developments	56
4.2.1	Kinematics	56
4.2.2	Isotropic Invariants and the Free-Energy Density Function	58

4.2.3	Constitutive Model for N fiber-families	60
4.2.4	Constitutive Model for Two Fiber-Families	64
4.3	Numerical Implementation	67
4.3.1	Numerical Integration of the Evolution Equations	67
4.3.2	Consistent Tangent Moduli	69
4.4	Linearization for the Small-Strain Limit	73
4.5	Viscoelastic Evolution of the Matrix Phase	75
4.6	Fiber Flow Stress for an Orthotropic Fiber Arrangement	76
4.7	Numerical Examples	77
4.7.1	Uniaxial tensile creep response	78
4.7.2	Simple shear relaxation response	80
4.7.3	Inflation of composite tube	82
4.8	Discussion	83
5	Cornea Deformation Under Physiological Inflation Conditions	87
5.1	Introduction	87
5.2	Method	88
5.3	Results	94
5.4	Discussion	97
5.5	Summary and Conclusions	99
	References	113

List of Figures

2.1	(a-c) Dicing of a cornea into a medial tensile strip along the nasal-temporal axis. (d) In-vitro tensile testing using pneumatic serrated grips in an oBSS bath.	19
2.2	Stress-controlled loading regimen and typical deformation response for (a) multiple stress-rate loading cycles with alternating recovery segments, and (b) a constant-stress creep hold.	20
2.3	(a-c) Strain response during loading and unloading at three different loading rates. (d) Recovery at a dwell stress of 14 kPa after the 35 kPa/s loading cycles. All results correspond to the loading regimen shown in Figure 2.2a.	23
2.4	The average tensile stress-strain response of bovine cornea tissue in the nasal-temporal orientation at each of three different strain rates.	24
2.5	The creep response along the nasal-temporal direction at three different hold stresses where the error bars represent one standard deviation.	28
2.6	Fit to (a) the instantaneous response data and (b) the low stress creep data normalized by the initial strain.	29
2.7	Comparison of average stress-strain responses of cornea tensile strips from this study and Refs. [35, 45] and in the vicinity of 10%/min.	30
2.8	Comparison of creep response using strains normalized by their initial values	31
3.1	Generalized Maxwell rheological model for the viscoelastic behavior of the stroma.	36
3.2	Probability density function for the preferred in-plane orientation of collagen fibrils developed by [69] for the human cornea for (a) the central cornea region, and (b) a region in the limbus. The 0° and 90° orientations corresponds to the nasal-temporal and inferior-superior meridians.	43

3.3	A sequence of simulations showing (a) the initial fit of the elastic parameters ($\bar{\alpha} = \alpha^{\text{eq}} + \sum_k^3 \alpha_k^{\text{neq}}, \beta$) using the 350 kPa/s rate data, and (b) fits of α_1^{neq} and α_2^{neq} to the 100 kPa creep data; a prediction of the 500 kPa creep data using only the $\alpha_1^{\text{neq}}, \alpha_2^{\text{neq}}$ fit; and fits of τ_2 and $(\alpha_3^{\text{neq}}, \tau_3)$ to the 500 kPa creep data.	44
3.4	Uniaxial creep strain curves obtained from experiments and simulation at three different applied engineering stresses for the central portion of corneal strips cut along the nasal-temporal (NT) direction. The error bars indicate a ± 1 standard deviation from the bin-averaged experimental data. The nonlinear viscoelastic model is fitted to 100 kPa and 500 kPa creep data and used to predict 350 kPa data.	46
3.5	Cyclic strain-time plot obtained from uniaxial tension experiments and simulations at three different stress rates: (a) 350 kPa/s for the NT orientation, (b) 35 kPa/s for the NT orientation, (c) 3.5 kPa/s for the NT orientation, and (d) 35 kPa/s comparing the NT and IS orientations. Error bars indicate a ± 1 standard deviation from the bin-averaged experimental data. The nonlinear viscoelastic model is fitted to the loading curve of 350 kPa/s and creep data and used to predict response of lower stress rates.	47
3.6	Anisotropic behavior of nonlinear viscoelastic model calculated for the fibril density function in eq. (3.24): (a) stress-strain response at 500kPa/s and (b) reduced relaxation function for $\lambda = 1.04$ and reduced creep function for 500kPa. The angles $\theta = 5\pi/3$ and $\theta = \pi/3$ indicates orientations with highest and lowest fibril density.	48
4.1	Rheological model of viscoelastic behavior of soft fiber-reinforced composite.	59
4.2	Uniaxial tensile creep: (a) creep strain in the loading direction ε_{22} for case 1 of both models, (b) ε_{22} for cases 2 and 3 of both models, (c) ε_{11} for all cases of Model I, (d) ε_{11} for all cases of Model II, (e) ε_{33} for all cases of Model I, and (f) ε_{33} for all cases of Model II.	79
4.3	Simple shear relaxation: (a) shear stress in the loading direction σ_{12} for case 1 of both models, (b) σ_{12} for cases 2 and 3 of both models, (c) σ_{11} for all cases of Model I, (d) σ_{11} for all cases of Model II, (e) σ_{33} for all cases of Model I, (f) σ_{33} for all cases of Model II.	81
4.4	Stress relaxation for Model II subject to simple shear out of the plane of the fiber families: (a) shear stress σ_{13} along the loading direction (b) normal stress σ_{11} along the loading direction.	82

4.5	Schematic of thick-wall cylinder composed of two laminates of different fiber windings. The tube is inflated by applying a cyclic internal pressure while holding the ends fixed.	85
4.6	Cyclic inflation of laminate cylinder: (a) internal pressure vs. volume change, (b) the radial and hoop stresses, σ_{rr} and $\sigma_{\theta\theta}$, as a function of radial distance.	85
5.1	(a) Solid model of the cornea adapter ring interfacing with the saddle-shaped corneo-scleral junction. (b) The bovine globe being affixed to the adapter ring prior to removal of the posterior sclera and internal tissues	89
5.2	Solid model of the key elements in the cornea inflation apparatus.	91
5.3	The inflation regimen. Note that the final cycle F was performed in displacement control rather than pressure control. This permitted characterization of both creep and relaxation.	93
5.4	(a) Graphite flakes and transmission illumination of the cornea, (b) View of the illuminated speckled cornea from one of the DIC cameras	93
5.5	(a) DIC determination of the initial shape of a cornea along with (b) corresponding oblique view	94
5.6	Finite element mesh of the cornea, the red regions are held fixed, to approximate the permeation of the glue into the stiffer scleral tissue, and the inner surface is pressurized.	100
5.7	Typical displacement components U, V, and W, at a pressure of 8 <i>kPa</i>	101
5.8	Typical out-of-plane displacement, W, at 6 different pressures.	102
5.9	Averaged configuration at 3.6 <i>kPa</i> and after preconditioning	103
5.10	Cycle A : averaged displacements at t= (a) 11s, 5.07 <i>kPa</i> ; (b) 22s, 6.53 <i>kPa</i> ; (c) 33s, 8.00 <i>kPa</i> ; (d) 44s, 6.53 <i>kPa</i> ; (e) 55s, 5.07 <i>kPa</i> ; (f) 66s, 3.60 <i>kPa</i> ;	104
5.11	The average apex displacement at a function of applied pressure during triangular loading cycles A, B, and C, corresponding to pressurization rates of 0.036, 0.0045, and 0.29 <i>kPa/s</i> , respectively. Error bars indicate 1 standard deviation.	105
5.12	A comparison of average apex displacement for two nominally identical cycles in the loading regimen.	105
5.13	Creep and relaxation during cycles E and F, respectively.	106

5.14	Local mid-periphery displacement values compared to the apex displacement.	107
5.15	Response to pressures $0 - 32 \text{ kPa}$	108
5.16	Comparison of the apex displacement for the three regimens.	108
5.17	Comparison of the experimental apex displacement to the nominal model and one with increased fibril density.	109
5.18	Fibril density at selected points across the cornea	109
5.19	Simulated vertical displacements showing strong center cornea and relatively weak periphery	110
5.20	Displacements of the central region only: (a) total displacements for a primarily NT-IS oriented fibril density, and (b) the deviations of this deformation map with an isotropic (in-plane) arrangement of fibrils . . .	111
5.21	Applanation of a human cornea	111
5.22	Applanation reaction force due to loading at 1.0 mm/s and 10.0 mm/s .	112

List of Tables

2.1	The loading rate and orientation dependence of the maximum strain observed at the peak of the 500 <i>kPa</i> triangular stress profile. Each value represents an average of 12 observations.	22
4.1	Integration algorithm for $\lambda_{\alpha_{n+1}}^v$ for N fiber-families model.	67
4.2	Integration algorithm for $\mathbf{C}_{F_{n+1}}^v$ for N fiber-families model.	68
4.3	Integration algorithm for $\mathbf{C}_{F_{n+1}}^v$ for the two fiber-families model.	70
4.4	Algorithmic anisotropic moduli for the two fiber-families model.	71
4.5	Parameters for Models I and II for uniaxial creep of orthotropic fiber-reinforced composite.	78

Chapter 1

Introduction

The field of biomechanics has seen an explosion in interest and scholarly output over the past decade. This trend is not surprising given the overwhelming importance of mechanical behavior in the function of many tissues, the rise in funding, and the focus on multidisciplinary research. This project was designed to provide a fundamental understanding of the mechanics of soft, hydrated tissue while giving Sandia a beach-head in this important field and the potential to impact clinical practice and diagnosis, design of mimetic materials and modeling of mechanically-induced tissue damage. Soft biological tissues are some of the most complex structural materials known to man: they are typically nonlinear viscoelastic with multiple characteristic time-scales, anisotropic due to their composite nature, inhomogeneous at every length scale from molecular to the system level, and highly variable from subject-to-subject. For these reasons, there is an enduring need for pedagogical understanding of the mechanical behavior of these tissues. The program plan relied heavily on a closely coupled experiment and modeling effort, harnessing the synergy between the two in improving our understanding of these complex materials.

Each type of tissue in the body is unique in function and form. This fact ran contrary to our desire to obtain fundamental and broadly applicable knowledge and our need to keep a finite scope. After some initial investigations that included other tissues and animal species, we chose bovine cornea as a model soft tissue. The cornea is skin-like tissue, since it is formed from a similar collagen fibril embedded in a hydrated proteoglycan matrix, with some unique properties, the most apparent being its transparency and its lack of vasculature. While the field of soft-tissue biomechanics had largely focused on ligament and vascular tissue due to their obvious biomechanical functionality, other important structural soft tissues, such as the cornea, have received much less attention. In the case of the cornea, the biomechanical response plays a key role in diseases such as keratoconus and corneal dystrophies and corrective surgeries such as LASIK and laser thermal keratoplasty. The specificity of the corneas structure to its function limited the type of experiments that were feasible and relevant to clinical practice. The program was designed around two types of experiments: (a) tension tests of excised strips and (b) bulge testing of intact corneas. The tension experiments (Chapter 2) were performed first and had the advantage of a simple, nearly homogeneous state throughout the test which eased the constitutive modeling and parameter fitting. Moreover, the simple tension state facilitated design

and interpretation of the experiments and allowed us to focus on the time/rate dependent behavior of the material. Preliminary permeability studies led us to discount a poroelastic approach to modeling the mechanical behavior of the cornea in favor of a viscoelastic paradigm. The complex behavior we observed was beyond the capacity of traditional quasi-linear viscoelasticity to predict and led to the development of a sophisticated constitutive viscoelastic anisotropic model (Chapter 3). We developed a novel optimization scheme to reduce the high dimensional parameter fitting problem to a sequence of low dimensional fits and generalized the model and applications to a range of soft composites (Chapter 4). From the first tests it was clear that the tension response was dominated by the collagen fibrils embedded in the hydrated proteoglycan matrix of the cornea. We also performed preliminary compression studies to try to extract directly the matrix response. The model we developed from the tension data incorporated the microstructure of the soft composite corneal tissue but the induced anisotropy was only tested in the second phase of the research program. The bulge experiments (Chapter 5) involved a relatively complex stress state, but had the advantage of testing the cornea in a stress state much closer to physiological. With full-field deformation maps from the experiments we were able to model the geometry of the undeformed corneas and correlate the expected anisotropic behavior with the actual.

The project developed and integrated a number of tools, including new experimental methods, optimization/correlation techniques, and constitutive models to characterize a complex material with significant medical and technological applications. These capabilities, which were extensions of Sandias core competencies in mechanics and materials science, have established Sandia as an unique contributor in the field of biomechanics. The unique capabilities developed in this program are currently being leveraged with optometry researchers at U.C. Berkeley to better understand the mechanical pathogenesis of myopia in scleral tissue, the white structural outer shell of the ocular globe. An NIH proposal based on pilot data collected as part of this program is expected on this topic. Future work, building off of the capabilities developed in this program, could span the range from modeling/design of soft mimetic composites to single cell manipulation for bio-defense to mechanically-based disease diagnosis and treatment.

Chapter 2

Stress-Controlled Viscoelastic Tensile Response of Bovine Cornea

The viscoelastic response of bovine corneas was characterized using *in vitro* load-controlled uniaxial tension experiments. Specifically, two types of tests were employed: cycled ramp tests over a range of loading rates and creep tests over a range of hold stresses. Multiple replicates of each were used to quantify the natural variability as well as mean trends. A preconditioning protocol was used to obtain a unique reference state before testing and to overcome the effects of non-physiological loading. A quasi-linear viscoelastic model incorporating a representation of the microstructure of the cornea was compared to the experimental results. For low stresses and moderate durations this model compares favorably, but overall the material displays non-linearities that can not be represented within the quasi-linear framework.

2.1 Introduction

The cornea's structural performance is dominated by the stroma which constitutes ~90% of the cornea thickness. The stroma consists of stacked lamellar sheets of collagen fibrils embedded in a hydrated matrix of proteoglycans, glycoproteins, and keratocytes [19, 56]. Each layer of (nearly) parallel fibrils lies obliquely to the neighboring layers, see, e.g., [69, Figure 1]. Within the central cornea, fibrils tend to run from limbus to limbus, and are preferentially aligned along inferior-superior (IS) and nasal-temporal (NT) axes [58, 11]. Near the edge of the cornea, fibrils tend to be aligned circumferentially. Since collagen fibers are the stiffest component of the cornea's structure, their alignment and density within lamellae largely control cornea mechanical response [43, 11].

Previous studies on cornea mechanics have typically employed a tensile strip method [64, 3, 35, 45, 89, 86], or a more physiologically relevant inflation method [88, 44, 34, 77]. These measurements have been used, for example, to study the efficacy of cross-linking agents as means to counteract keratoconus [86, 80]. However, very few previous investigations have explicitly characterized the viscoelastic response, the notable exception being the study [64]. Moreover, while fiber-matrix models have

been developed to describe corneal anisotropy [68, 69], there do not appear to be any viscoelastic cornea models.

Viscoelastic response has been studied more thoroughly in other soft tissues, including ligament, tendon, articular cartilage, muscle, and cardiovascular tissues, where the physiological manifestations of viscoelasticity are more apparent. For example, in ligament research, experimental results have guided development of a series of models [47, 70, 71, 85, 33]. The most commonly employed formulation is quasilinear viscoelastic (QLV) theory [28]. However, recent work has called into question the ability of QLV theory to represent observed behavior [70, 33].

The present study characterizes the viscoelastic response of the cornea and evaluates the fidelity of QLV theory. We hypothesize, based on aforementioned observations in ligament tissue, that QLV theory will not adequately describe cornea behavior. To explore this hypothesis, *in vitro* bovine cornea tensile stress-rate and creep tests were used to evaluate a newly developed microstructurally-based QLV formulation.

2.2 Materials and Methods

Experimental. Bovine cornea was selected for this study because its large size facilitates strip extraction, and it is not subjected to scalding which can damage porcine corneas during slaughter. Moreover, its response appears to be closer to human than porcine cornea (see Section 2.4 and Figure 2.7). Untreated bovine ocular globes from beef cattle 18-24 months in age were obtained from a medical supplier within 24 hours after slaughter. During this time, the intact ocular globes were stored in a sealed polypropylene bag at 5 °C, with no noticeable degradation or swelling. For each harvested cornea, one 7.0 mm wide tensile strip was sliced from the medial section along either the the NT or IS axis (Figure 2.1). The tensile strip comprised the full cornea thickness (1.15-1.30 mm) and the total length ran from limbus to limbus. After excision, tensile strips were stored in a sealed bag between cloth sheets saturated with Cytosol ophthalmic balanced saline solution (oBSS) at 5°C for up to 8 hours prior to testing. Tensile testing was performed using an MTS servohydraulic loadframe with pneumatically-clamping serrated soft tissue grips. The gage length was defined by the ~8.0 mm length of tissue that spanned between the two grips. The tensile specimen and grips were immersed in a recirculated oBSS bath held at 30°C. The oBSS bath, used in clinical practice, is iso-osmotic with the cornea to minimize tissue swelling. Tensile testing was performed under stress control at engineering stresses up to 500 kPa corresponding to engineering strains ($\Delta L/L$) as large as 5%. This value is beyond strains associated with normal changes in intraocular pressure which are ~1% [77], but relevant to injury and some surgical procedures. Because the cornea tissue was substantially more compliant than the load train, actuator displacement was sufficient to monitor axial strain. No correction was made for the strain inhomogeneities associated with flattening of the initially curved cornea.

Hoeltzel [35] suggests that this effect is negligible, noting that the cornea behaves like a membrane, with very little resistance to out-of-plane bending, presumably because the lamellae of the cornea only weakly transmit in-plane shear. In contrast, [25] computed corrections to the stress-strain response for the flattening effect and variations in the corneal thickness. However, the calculations assume linear elastic response inconsistent with the cornea data presented herein.

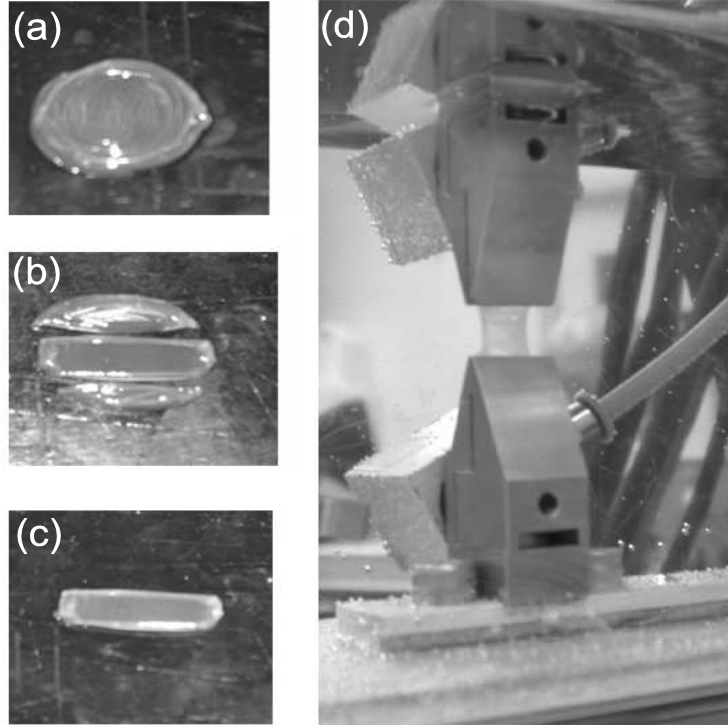


Figure 2.1. (a-c) Dicing of a cornea into a medial tensile strip along the nasal-temporal axis. (d) In-vitro tensile testing using pneumatic serrated grips in an oBSS bath.

For each cornea, either a “multi-stress-rate” regimen or a “creep” regimen was applied (Figure 2.2). Both regimens were initiated with a series of 5 cycles that preconditioned the tissue to a stress level of 500 kPa (Figure 2.2). Preconditioning is widely used in the mechanical testing of soft tissues [76, 82, 22, 18]. The need for preconditioning to attain a unique, recoverable reference state implies that the material is loaded in a non-physiological state and that microstructural reconfiguration is likely; therefore, the results of the subsequent experiments serve better to evaluate response characteristics of the excised strips rather than material properties of the intact cornea.

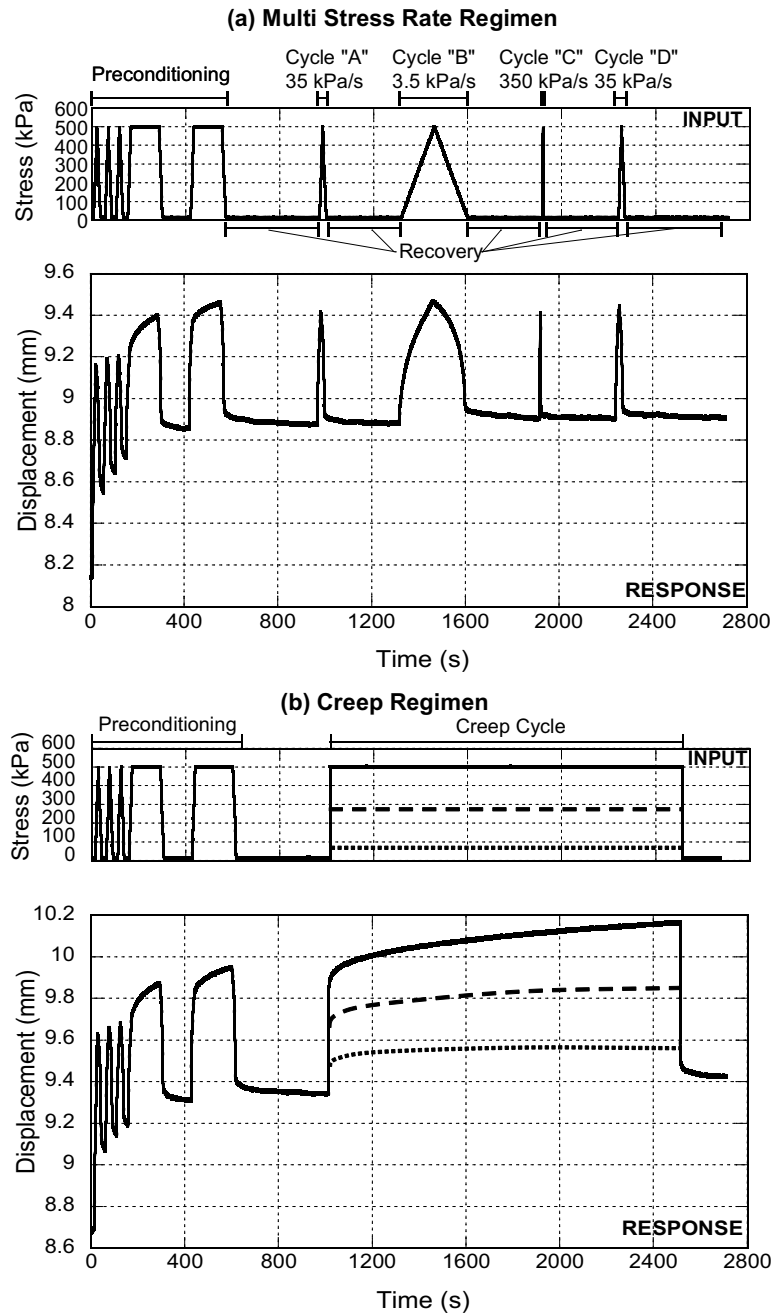


Figure 2.2. Stress-controlled loading regimen and typical deformation response for (a) multiple stress-rate loading cycles with alternating recovery segments, and (b) a constant-stress creep hold.

The multi-stress-rate regimen consisted of a series of 3 triangular loading cycles at rates of 35, 350, and 3.5 kPa/s (cycles A through C in Figure 2.2), to a maximum stress of 500 kPa . Between cycles, a recovery period at a near-zero stress level was applied. The final cycle D was a repetition of the first cycle A and was used to confirm that prior deformation was fully recoverable.

The creep regimen utilized the same preconditioning and recovery segments, but the test phase was replaced by a nearly instantaneous 4000 kPa/s ramp to a hold stress of 100, 350, or 500 kPa . This maximum stress was held for 1500 s .

Modeling. Quasilinear-viscoelasticity (QLV) has been commonly employed to model time-dependent behavior of soft tissues, see, e.g., [28, Section 7.6]. It assumes that the (second Piola-Kirchhoff) stress response to a history of deformation can be represented by a convolution of a deformation dependent function \mathbf{S}_e with a strictly time-dependent dimensionless kernel G :

$$\mathbf{S}(t) = \mathbf{S}_e(\mathbf{C}(t)) + \int_0^t \mathbf{S}_e(\mathbf{C}(s)) \dot{G}(t-s) ds . \quad (2.1)$$

Here $\mathbf{C} = \mathbf{F}^T \mathbf{F}$ is the right Cauchy-Green deformation tensor and \mathbf{F} is the deformation gradient. Neubert [61] developed a particular form of the kernel $G(t)$,

$$G(t) = G_\infty \left(1 + c(E_1(t/\tau_2) - E_1(t/\tau_1)) \right) \quad (2.2)$$

with a frequency spectrum that is inversely proportional to τ between τ_1 and τ_2 . Here, $E_1(t)$ is defined by $E_1(t) = \int_t^\infty \frac{1}{s} \exp(-s) ds$ and the constant $G_\infty = (1 + c \log(\tau_2/\tau_1))^{-1}$ normalizes $G(t)$ such that $G(0) = 1$. This form represents the nearly linear relaxation response over logarithmic time which is typical of soft tissues (see, e.g., [28, Section 7.6]).

Given the fibril-matrix structure of the cornea it is reasonable to assume that the function $\mathbf{S}_e = 2\partial_{\mathbf{C}}W$ can be written as the sum of contributions from the two constituents $W = W_{matrix} + W_{fibrils}$. Following [69], the fibril strain-energy function, $W_{fibrils}$, is determined by integrating contributions of individual fibrils w_{fibril}

$$W_{fibrils} = \frac{1}{2\pi} \int_{-\pi}^{\pi} w_{fibril}(\lambda_{\mathbf{M}}(\theta)) \phi(\theta) d\theta ,$$

where θ is the in-plane angle, and $\phi(\theta)$ is the in-plane fibril distribution. The invariant $\lambda_{\mathbf{M}} = \sqrt{\mathbf{M} \cdot \mathbf{C} \mathbf{M}}$ is the stretch along direction $\mathbf{M} = \mathbf{M}(\theta)$. The particular form of w_{fiber} , adapted from [83],

$$w_{fibril}(\lambda) = \alpha \left(\exp(\beta(\lambda^2 - 1)) - \beta\lambda^2 \right) , \quad (2.3)$$

is known to represent the J-shaped stress-strain curve of biological tissues well. Since the matrix is composed of mostly hydrated ground substance, it is assumed to be

Loading Rate (kPa/s)	Peak Strain (%)	
	Nasal-Temporal	Inferior-Superior
3.5	5.3	5.1
35	4.8	4.4
350	4.4	4.1

Table 2.1. The loading rate and orientation dependence of the maximum strain observed at the peak of the 500 *kPa* triangular stress profile. Each value represents an average of 12 observations.

isotropic, nearly incompressible and adequately represented by a neo-Hookean hyper-elastic model

$$W_{matrix} = \frac{\mu}{2}(\text{tr } \mathbf{C} - 3) + \frac{\mu}{2\gamma}((\det \mathbf{C})^{-\gamma} - 1) .$$

with $\gamma = 0.49$. The QLV formulation, modified by this fibril-matrix partitioning of the strain energy density, was evaluated in the context of the observed cornea tensile behavior.

2.3 Results

Experimental. Multi-stress-rate tests were performed on 12 corneas under nominally identical conditions. The axial component $\Delta L/L$ of engineering strain, $\sqrt{\mathbf{C}} - \mathbf{I}$, is plotted versus time in Figure 2.3 for three stress-rates and two tensile orientations. The trend lines represent the average response from 12 tests and the error bars represent one standard deviation. The average strains observed at peak loading are compiled in Table 2.1.

An important assumption was that deformation in the test phase loading cycles was completely recovered between cycles. As shown in Figure 2.3b, the first and last cycles at stress rate of 35 *kPa/s* appear to exhibit nearly identical behavior. For example, the average peak strain in cycles A and D (NT orientation) was 0.0492 ± 0.0072 *mm/mm* and 0.0476 ± 0.0070 *mm/mm*, respectively. While this small (3%) difference was statistically significant when the cycles were compared within a single specimen (a pairwise t-test [81] yielded $\hat{t} = 7.5 > t_{.90,11} = 1.363$), it was greatly overshadowed by specimen-to-specimen variability. This supports the notion of a (nearly) repeatable reference state.

Also of note, both in Table 2.1 and in Figure 2.3, is the apparent orientation dependence on the resulting strain response. On average, the IS aligned tensile bars exhibited less strain than the NT ones. A statistical paired *t*-test [81] on the peak

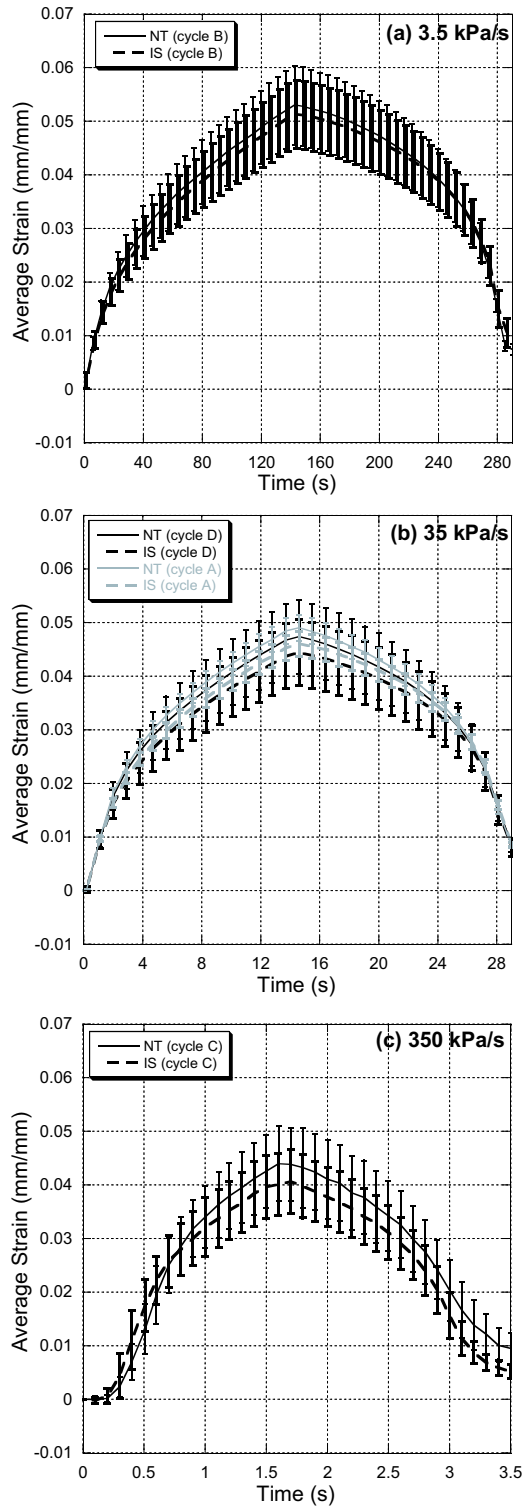


Figure 2.3. (a-c) Strain response during loading and unloading at three different loading rates. (d) Recovery at a dwell stress of 14 kPa after the 35 kPa/s loading cycles. All results correspond to the loading regimen shown in Figure 2.2a.

response of 12 pairs of NT and IS specimens loaded at 35 kPa/s , yields a t -statistic of $\hat{t} = 1.5$, indicating that the stiffer IS orientation was statistically distinguishable from the NT orientation with 90% confidence ($\hat{t} = 1.5 > t_{0.9,11} = 1.363$).

The average engineering (first Piola-Kirchhoff) stress-strain response for the NT orientation is plotted for the three stress-rates in Figure 2.4 (along with simulation results which will be discussed later in this section). The response demonstrated the J-shape typical of collagenous tissues. Also, as expected from a viscoelastic material, increased hysteresis was observed with decreasing stress-rate.

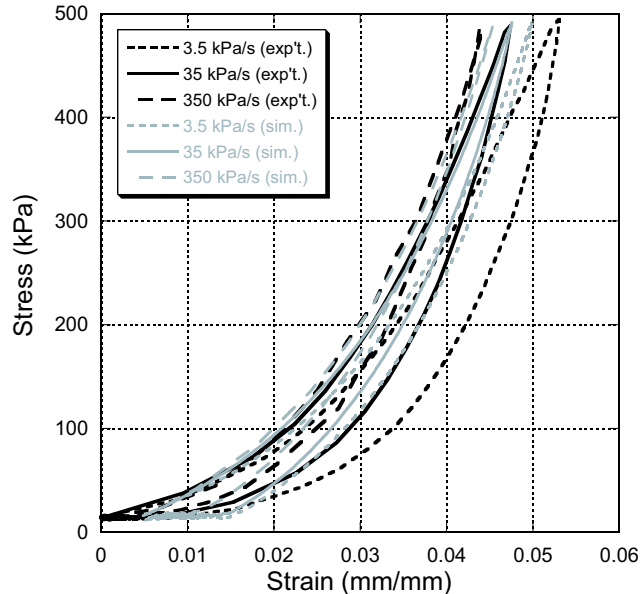


Figure 2.4. The average tensile stress-strain response of bovine cornea tissue in the nasal-temporal orientation at each of three different strain rates.

The creep regimen was applied to 27 NT-oriented tensile strips: 9 at each of 3 hold stresses, with results shown in Figure 2.5. The creep response at the lowest stress level of 100 kPa was linear when plotted on this logarithmic time scale, whereas the larger hold stresses resulted in an accentuated non-linear creep strain that accelerates over time. The distribution of creep responses at hold stresses of 350 and 500 kPa shows some overlap. However, a paired t -test determined that the creep response between these two datasets were indeed statistically distinguishable at a 90% confidence level ($\hat{t} = 1.5 > t_{0.9,8} = 1.397$).

Parameter Estimation and Model Results. Using the proposed QLV model, the tension experiments were simulated assuming a homogeneous state of stress, with principal stretches aligned with the axes of the specimen. The details of the boundary

conditions and as well as any Poisson or edge effects were ignored at this point. Also, given the lack of information about bovine fibril distribution and the uncertainty of which orientations in the excised specimens were engaged by the loading, the distribution function was set to unity, $\phi(\theta) = 1$. This corresponds to transverse isotropy (and a Poisson’s ratio of 0.25 for the fibril phase). If, for instance, it was certain that all the fibrils in a 45° sector about the NT axis were recruited then the stiffness parameter α could be corrected for the fact that about a third of the total distribution [11] were being loaded. With these assumptions, 6 free parameters $\{\alpha, \beta, \mu, \tau_1, \tau_2, c\}$ were left. A weighted sum of least square errors quantified the correlation between experimental data and simulations.

To determine the function \mathbf{S}_e the loading portion of the 350 kPa/s high-rate stress cycle C and the first point of each of the creep tests were used, since this data is assumed to be close to the instantaneous elastic response. An initial global study of the error as a function of $\{\alpha, \beta, \mu\}$ showed insensitivity to μ and consequently μ was set to 10.0 kPa (the same order of magnitude as cited in [69] for human corneas). (See [76] for a complete sensitivity analysis of the QLV framework). This plausible “weak matrix” assumption, where the matrix makes a relatively small contribution to the stiffness of the material, leaves just α and β controlling the elastic response. The same parameter study shows that there is considerable ambiguity in the existence of optimal $\{\alpha, \beta\}$. In an attempt to find a global minimum of the error norm, the best of a large random sample of a bounded parameter space were used to initialize a series of local Newton optimizations. Figure 2.6a shows the resulting fit where \mathbf{S}_e has been reparameterized as $\{\bar{\alpha} = \alpha\beta = 70.65 \text{ kPa}, \beta = 30.4\}$.

In order to determine the kernel function G in a manner as independent as possible from the determination of \mathbf{S}_e given the stress-controlled experiments, normalized strain histories were compared. Here, the strain history of each creep test and the corresponding simulations were shifted by their initial values to minimize polluting effects of an imperfect elastic fit. Only the low stress (100 kPa) creep response was used for fitting. Also, since it was apparent that the error sensitivity to the parameter τ_2 was very low once τ_2 had a value larger than the duration of the experiment, it was fixed at $\tau_2 = 10,000 \text{ s}$. Likewise, given the near linearity of the low stress response in Figure 2.5, τ_1 was set to 1 s . This choice is also justified by: (a) the control of the initial part of the test makes the accuracy of the short time response dubious [23], and (b) a lack of significant time dependence below the characteristic time of 1 s is consistent with the assumption that the response to the fast loading cycle C is essentially elastic. The last free parameter, c , was determined with the same method as used to fit $\{\alpha, \beta\}$. The response using the resulting optimal value $c = 0.20$ is compared to experimental data in Figure 2.6b.

The QLV model with parameters $\{\alpha\beta = 70.65 \text{ kPa}, \beta = 30.4, \mu = 10 \text{ kPa}, \tau_1 = 1 \text{ s}, \tau_2 = 10,000 \text{ s}, c = 0.20\}$ was used to predict the experimentally observed stress-strain and creep-time data. The model predictions are shown alongside experimental results in Figure 2.4 and Figure 2.5.

2.4 Discussion

The stress-strain response of bovine cornea exhibited significant non-linearity, resulting in the well-known J-shape shown in Figure 2.4. As shown in Figure 2.7, the present study measured a much stiffer response than other studies that did not employ preconditioning. A more direct comparison was made by extracting the stress-strain response from our first preconditioning cycle. This un-preconditioned data (triangles in Figure 2.7) exhibited similar behavior to the bovine experiments reported in [35]. Unlike the present preconditioning methodology, simple single-ramp experiments combine recoverable viscoelastic strain *with inelastic* strain.

Another literature comparison was made with regard to mechanical anisotropy. Kampmeier [45] found that porcine corneas were stiffer along the IS axis than the NT axis, which is consistent with the present observations where the effect was much less pronounced. Wide angle x-ray scattering experiments [13] on human corneas were unable to statistically distinguish fibril densities in the NT and IS direction, although they did show a dramatic reduction in fibril densities at 45° between the NT and IS directions.

As expected, the cornea exhibited significant viscoelasticity as evidenced by: (a) asymmetry in the ramp loading-unloading response in Figure 2.3a-c, (b) corresponding hysteresis in the stress-strain response in Figure 2.4, (c) exponential recovery at low stresses after ramp cycles in Figure 2.3d, and (d) time-dependent creep behavior at a variety of hold stresses in Figure 2.5. In light of these observations, it is surprising that nearly all existing literature on cornea mechanics failed to characterize viscoelastic behavior; most utilized a single load ramp at a single strain rate.

Following developments in other soft tissues, a QLV model was devised in an attempt to represent cornea behavior. The fitted elastic parameters compare well to corresponding published ones. Specifically, the initial stiffness of the fibers $\alpha\beta^2 = 65.3 \text{ MPa}$ is on the same order of magnitude and therefore comparable, given population variability, to the value 10.0 MPa for a one parameter model fitted to human data in [69]. Furthermore, the value determined for the exponent $\beta = 30.4$ is within the range (12.20–66.96) cited in [70] for a similar two parameter model applied to ligaments. As mentioned previously, there is very little experimental data for viscous properties of the cornea. In particular, the work [64] is not sufficiently quantitative to allow meaningful comparison of parameters τ_1 , τ_2 and c .

Figure 2.5 shows that the creep response of the model with the fitted parameters compares well to the low-stress creep, with only a small strain offset associated with error in the elastic fit (Figure 2.6a). On the other hand, it compares quite poorly to the two other experimental curves due to the increasingly non-linear response. This feature is likely indicative of the activation of additional creep modes which are not engaged in the low-stress (100 kPa) creep response. This concept is explored in detail in [62].

By dividing the strain history of each creep experiment by its initial value (Figure 2.8), it is apparent that this normalized creep strain in the first $\sim 10s$ is nearly identical across stress levels. In fact, the medium stress level (350 kPa) diverges from the low stress (100 kPa) response only after about 100 s . Examining Figure 2.5, it is noteworthy that these times (10 s , 100 s) correspond to $\sim 4.8\%$ strain, after which the similarity in the creep response breaks down. Clearly, the form of the kernel in Equation (2.2) is representative of the low stress creep response; but, Figure 2.5 also illustrates the failing of QLV to model the stress-dependent creep response (discussed at length in [71]). Although fitting the lowest stress creep well, a model of the form Equation (2.1) does not fit even the first $10s$ of the normalized strain perfectly. This is due to the fact that, in creep, the elastic component and time-dependent component of the response are not so neatly separable as Equation (2.1) predicts, and, consequently, the creep response is not exactly similar across load levels. Instead of the inverse of $\mathbf{S}(t)$ defined by (2.1), Figure 2.6b indicates that an analogous QLV model based on a stress-dependent $\mathbf{C}_e = \mathbf{C}_e(\mathbf{S})$ would be more representative of at least the first $10s$ of the creep data.

The strain-based model, (2.1), was also used to predict the experimental results from the cyclic tests. Figure 2.4 shows reasonable correlation with the experimental data's trends within the measured material variability. The high-rate loading response in Figure 2.4 compared to Figure 2.6a shows that there is a small but non-negligible viscous effect at this loading rate.

As a final comment, there are a number of limitations to the present effort which motivate subsequent work. From an experimental perspective, the undesirable non-physiological nature of the tensile test and the corresponding need for preconditioning cycles may be overcome by inflation tests (see, e.g. [16, 34, 25]). From a modeling perspective, the classical separable QLV does not appear to be sufficient to represent the observed stress-dependent non-linearities. Subsequent work will examine the ability of a fully non-linear viscoelastic model to predict the response of composite, hydrated soft tissues.

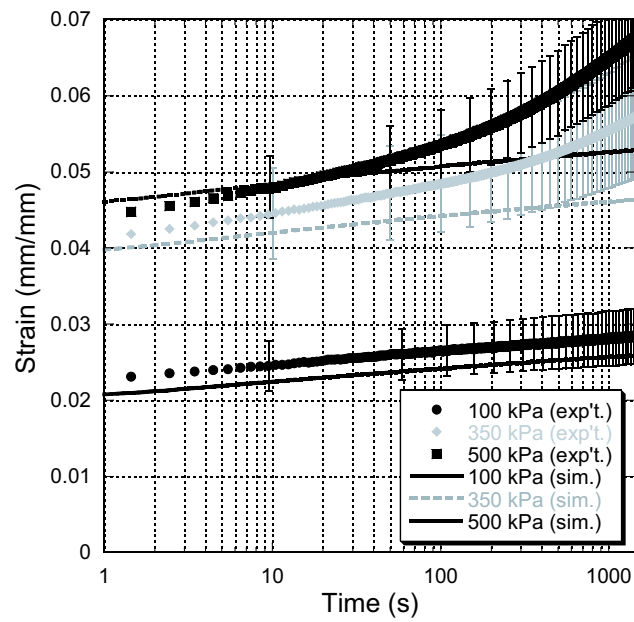


Figure 2.5. The creep response along the nasal-temporal direction at three different hold stresses where the error bars represent one standard deviation.

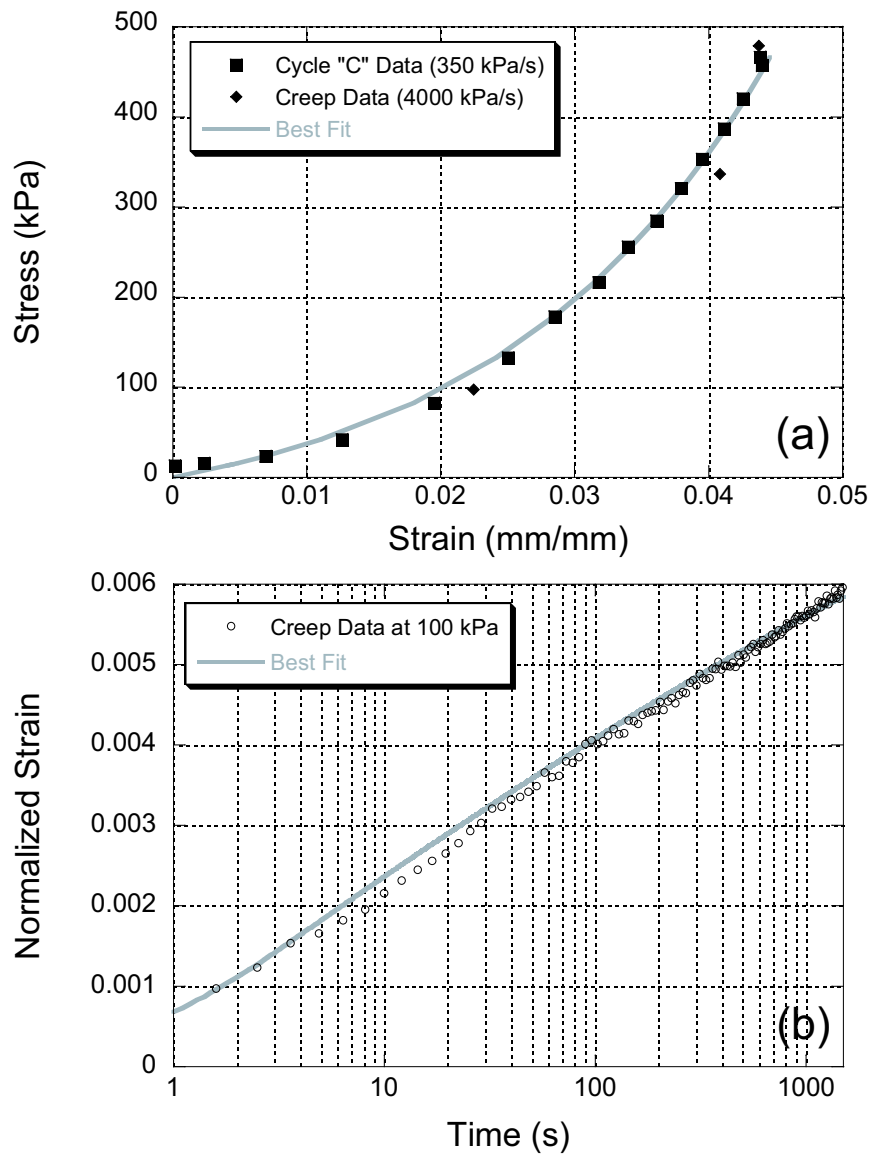


Figure 2.6. Fit to (a) the instantaneous response data and (b) the low stress creep data normalized by the initial strain.

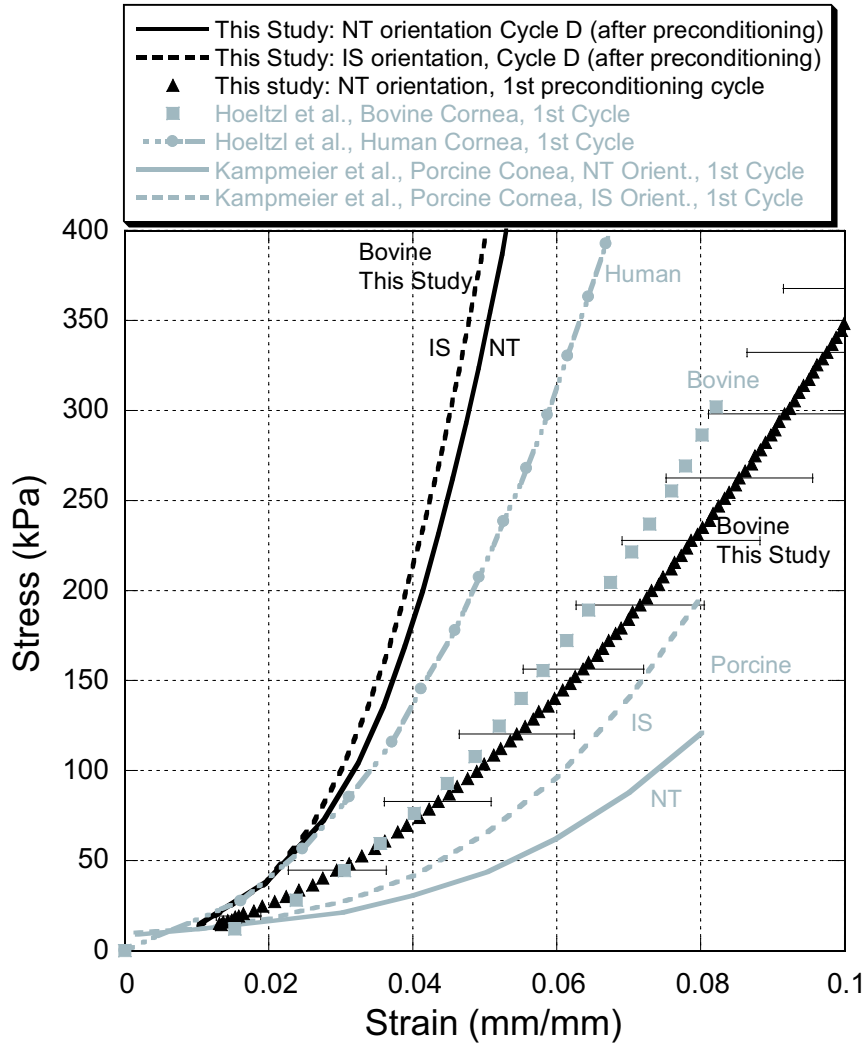


Figure 2.7. Comparison of average stress-strain responses of cornea tensile strips from this study and Refs. [35, 45] and in the vicinity of 10%/min.

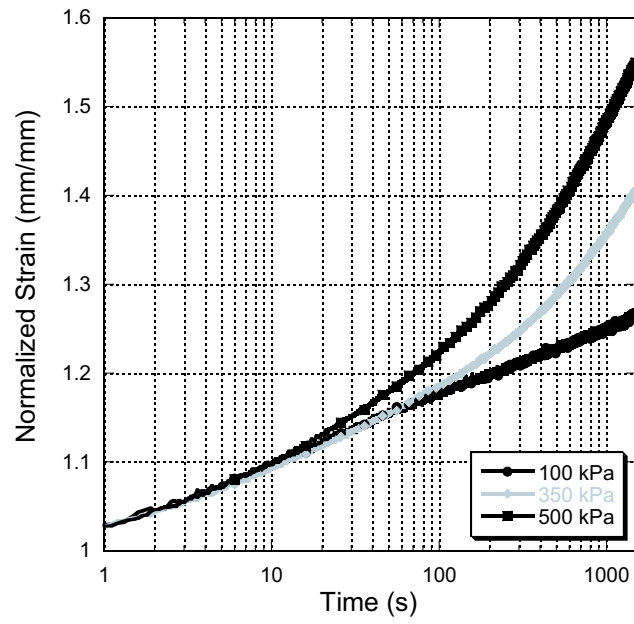


Figure 2.8. Comparison of creep response using strains normalized by their initial values

Chapter 3

A Nonlinear Viscoelastic Model for the Tensile Behavior of Bovine Cornea

Tensile strip experiments of bovine corneas have shown that the tissue exhibits a nonlinear rate-dependent stress-strain response and a highly nonlinear creep response that depends on the applied hold stress. In this chapter, we present a constitutive model for the finite deformation, anisotropic, nonlinear viscoelastic behavior of the corneal stroma. The model formulates the elastic and viscous response of the stroma as the integrated average of the elastic and viscous response of the individual lamellae weighted by a probability density function of the in-plane lamellar orientations. In contrast to previous viscoelastic models for soft tissues, the model does not formulate a viscous flow rule for the stroma as a whole but calculates it by homogenizing the viscous flow rule of the lamellae. This allows a description of the fibril arrangement to be included in both the effective stiffness and viscosity of the stroma. Simulations of recent tensile strip experiments show that the model is able to predict, well within the bounds of experimental error and natural variations, the cyclic stress-strain behavior and nonlinear creep behavior observed in uniaxial tensile experiments of excised strips of bovine cornea.

3.1 Introduction

A unique combination of mechanical strength, stiffness, and optical transparency enables the cornea to serve as both a protective barrier and the primary refractive component of the eye. These properties are derived from the fiber-reinforced microstructure of the corneal stroma, which in humans is formed by approximately 200 lamellae of type I collagen fibrils embedded in a matrix composed mainly of proteoglycans and water [56]. The collagen fibrils are uniform in diameter, run parallel and equidistant within each lamella, and subtend large angles between adjacent lamellae [49, 13]. Numerous experiments have shown that the mechanical behavior of the cornea is anisotropic, viscoelastic, and highly nonlinear [64, 88, 2, 44, 36, 34, 77, 46, 87, 14]. It is assumed that the mechanical anisotropy arises from the preferred orientations

of the collagen fibrils in the plane of the stroma which has been characterized for humans and certain species of primates by X-ray diffraction [58, 21, 1, 11].

Experiments have shown that the tensile nonlinear stress-strain response of bovine cornea is also rate-dependent, characterized by increasing stiffness and decreasing hysteresis with increasing loading rate [14, 64]. The creep response is also nonlinear with the creep rate increasing with the applied hold stress. The physical processes responsible for the nonlinear viscoelastic behavior of the cornea are poorly understood. The cornea is a bi-phasic material with water comprising 78% the weight of the corneal stroma [57]. As such, the flow of interstitial fluid in the proteoglycan matrix is a possible mechanism for the time-dependent behavior of the cornea. Additionally the proteoglycan matrix, collagen fibrils, and fibril-matrix interface can exhibit intrinsic time-dependent deformation mechanisms. The fluid flow mechanism is the basis of the multiphasic/poroelastic approach that has been applied successfully to model the time-dependent response of articular cartilage and other connective tissues in compression. However, the multiphasic approach has not been less successful in modeling the time-dependent behavior of cartilage under uniaxial tension [41]. This difficulty has been attributed to the fact that soft tissues tend to exhibit a significantly stiffer stress response in tension than in compression. [41] developed a biphasic model that incorporated the large difference between the tensile and compressive moduli of cartilage. The model showed good agreement with experiments in predicting the response of the tissue in unconfined compression, but it failed to produce a transient response in uniaxial tension. This led the authors to suggest that uniaxial tension is a discriminating testing configuration for the intrinsic viscoelasticity of the solid constituents of cartilage.

In this chapter, we propose a model for the finite deformation tensile behavior of the cornea that considers the viscoelastic behavior of the lamellae as the primary mechanism for the in-plane tensile viscoelastic behavior of the cornea observed in experiments. We base this assumption on the fact that the cornea operates mostly in tension where it has been suggested that poroelasticity has a less important effect. In addition, experiments have observed consistently faster creep rates at higher applied tensile stresses [14, 64] where the stresses are increasingly borne by the collagen fibril reinforcements. The model does not resolve the physical mechanisms of viscoelastic behavior of the stroma below the lamellar level because they are not well characterized for the cornea. Recent experiments on tendinous tissues indicate that the viscoelastic behavior at the fiber level, analogous to the lamellar level in the corneal stroma, can be attributed to “proteoglycan mediated fibrillar interactions” such as the viscous sliding of the fibrils in the proteoglycan matrix [51, 24, 72]. Faster stress relaxation have been observed in tendinous tissue with smaller concentrations of glycosaminoglycans that serve to crosslink the collagen fibrils to each other and to the proteoglycan matrix. These mechanisms can be active in excised corneal tissues where the severed collagen fibrils are free to reorient within the lamellae. However, the effects of proteoglycan mediated interfibrillar mechanisms are less important in the intact corneal where the fibrils remain anchored at the limbus and lack the freedom to travel or reorient

significantly. The time-dependent behavior of the intact cornea still can arise from the intrinsic viscoelasticity of the collagen fibrils and proteoglycan matrix.

The goal of this chapter is to develop a constitutive model to simulate the mechanical response of the intact cornea. Thus, it is important consider the effects of anisotropy based on the heterogeneous fibril arrangement. Some previous efforts to model the fiber architecture of the cornea and the resulting mechanical anisotropy include [68, 69, 31, 67]. The hyperelastic model of [69] applied a widely accepted homogenization scheme (e.g., [50]) to relate the strain energy density of the corneal stroma to the average of the strain energy density of the lamellae weighted by the probability of their in-plane orientation. Though not as computationally efficient as the structure tensor approach commonly applied to model the anisotropy of soft tissues (see for example the work of [67] applied to the cornea), this homogenization approach is attractive because a detailed map of the preferred fibril orientation in the plane of the cornea is already available from X-ray diffraction experiments of human corneas [58, 21, 1, 11].

Several approaches have been proposed for modeling the finite deformation, anisotropic, viscoelastic behavior of soft tissues (see for example [70], [52], [39], and [8]). Here, we develop a model for the tensile behavior of the cornea based on a newly developed general nonlinear constitutive framework for anisotropic viscoelasticity of soft fiber-reinforced composites [62]. The model represents the stroma as a continuum mixture consisting of collagen fibrils organized into lamellae characterized by an in-plane orientation angle and embedded in a soft isotropic matrix. Both constituents are required to deform according to the continuum deformation gradient. The model assumes that the time-dependent behavior of the cornea is dictated by the viscoelastic deformation of the lamellae. This is modeled using an internal variable approach by assuming a decomposition of the deformation gradient into elastic and viscous parts and an additive decomposition of the anisotropic component of the free energy density into equilibrium and nonequilibrium parts. We define the viscous stretch of the lamellae from the viscous deformation gradient and specify one-dimensional flow rules for the viscous stretch of the individual lamellae. These are combined to obtain an effective anisotropic flow rule for the viscous deformation of the corneal stroma. This is in contrast to previous approaches to modeling the anisotropic viscoelastic behavior of soft tissues, which usually specify an anisotropic evolution equation for the viscous deformation of either the fiber phase or the tissue as whole. Our approach naturally incorporates a description of the preferred fiber orientation into the effective viscosity as well as the effective moduli of the stroma.

The formulation of the model is presented in Sec. 3.2.1 as well as a description of the scheme used to estimate the model parameters from uniaxial cyclic and creep tensile tests. The following section demonstrates the successful ability of the model to reproduce the experimental data of [14] for the tensile behavior of the central region of bovine cornea. The time-dependent behavior of the model is also demonstrated for strongly anisotropic limbus.

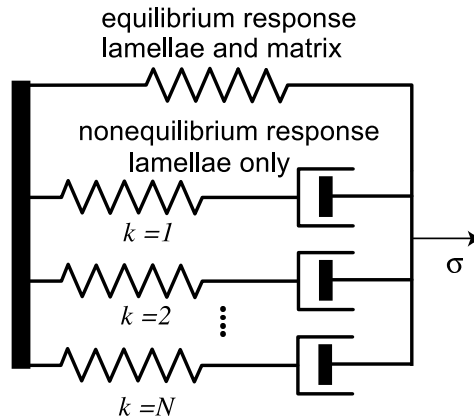


Figure 3.1. Generalized Maxwell rheological model for the viscoelastic behavior of the stroma.

3.2 Method

3.2.1 Model Formulation

In the following, we develop a model for the tensile behavior of the cornea based on a newly developed general nonlinear constitutive framework for anisotropic viscoelasticity of soft fiber-reinforced composites [62]. The corneal stroma is represented as a continuum mixture consisting of lamellae of unidirectional collagen fibrils characterized by an in-plane orientation angle θ , and bound by an isotropic matrix. It is assumed that the lamellae and matrix deform according to the continuum deformation gradient $\mathbf{F} = \frac{\partial \phi_t(\mathbf{X})}{\partial \mathbf{X}}$ that maps material lines from the reference (material) configuration Ω_0 to the deformed (spatial) configuration Ω . It is further assumed that the stress response of the stroma is described by the rheological model shown in Figure 3.1 where a single independent spring representing the time-independent equilibrium response acts in parallel with multiple Maxwell elements, numbered $k = 1 \dots N$, representing the different time-evolving nonequilibrium processes acting in the stroma. For simplicity, we assume that at large stresses and strains, where the most marked creep behavior of the cornea is observed in experiments, the time-dependent behavior of the cornea is dominated by the anisotropic viscoelastic deformation of the lamellae. The intrinsic isotropic viscoelastic behavior of the proteoglycan matrix that is independent from the viscoelastic deformation of the lamellae is considered negligible. Thus, the isotropic elastic behavior of the proteoglycan matrix is included in the equilibrium response of the stroma, represented in Fig. 3.1 by the equilibrium spring, but the isotropic viscous behavior of the proteoglycan matrix is excluded from the time-dependent nonequilibrium response of the stroma, represented by Maxwell elements in Figure 3.1. This assumption effectively neglects the out-of-plane time-dependent tensile behavior of the cornea that is difficult to characterize experimentally.

The kinematics of each nonequilibrium process of the lamellae is described by the multiplicative split of the deformation gradient into elastic and viscous parts,

$$\mathbf{F} = \mathbf{F}_k^e \mathbf{F}_k^v. \quad (3.1)$$

The viscous deformation gradient, \mathbf{F}_k^v , defines a mapping to an intermediate configuration $\tilde{\Omega}_k$ for the stroma. The elastic component \mathbf{F}_k^e is then the complementary mapping from $\tilde{\Omega}_k$ to the deformed configuration. From equation (3.1), we can define the Cauchy-Green deformation tensor as $\mathbf{C} = \mathbf{F}^T \mathbf{F}$, and the analogous viscous and elastic deformation tensors as, $\mathbf{C}_k^e = \mathbf{F}_k^{eT} \mathbf{F}_k^e$, and $\mathbf{C}_k^v = \mathbf{F}_k^{vT} \mathbf{F}_k^v$.

To describe the in-plane orientation of lamellae, we define a unit orientation vector in the reference configuration as $\mathbf{P}(\theta) = \{\cos \theta, \sin \theta\}$ and a structure tensor that is $\mathbf{M}(\theta) = \mathbf{P} \otimes \mathbf{P}$. Here θ is the in-plane angle. Because we've assumed that the lamellae deform with continuum body, the deformed orientation vector can be computed simply as $\lambda \mathbf{p} = \mathbf{F} \mathbf{P}$, where $\lambda(\theta)$ is the lamellar stretch and $\mathbf{p}(\theta)$ is the unit lamellar orientation vector in Ω . The lamellar stretch can be computed from this relation as,

$$\lambda = \sqrt{\mathbf{C} : \mathbf{M}}. \quad (3.2)$$

Substituting eq. (3.1) into the relation for the deformed lamellar vector, we can define the lamellar vector in the intermediate configuration as $\lambda_k^v \tilde{\mathbf{P}}_k = \mathbf{F}_k^v \mathbf{P}$, where $\lambda_k^v(\theta)$ and $\tilde{\mathbf{P}}_k(\theta)$ are defined as the viscous lamellar stretch describing the k th nonequilibrium process and the unit lamellar orientation vector in $\tilde{\Omega}_k$. From these quantities, we can define structure tensor in $\tilde{\Omega}_k$ as $\tilde{\mathbf{M}}_k = \tilde{\mathbf{P}}_k \otimes \tilde{\mathbf{P}}_k$ and compute the viscous and elastic components of the stretch of the lamellae as,

$$\lambda_k^v = \sqrt{\mathbf{C}_k^v : \mathbf{M}}, \quad \lambda_k^e = \sqrt{\mathbf{C}_k^e : \tilde{\mathbf{M}}_k} = \frac{\lambda}{\lambda_k^v}. \quad (3.3)$$

We will show that defining the lamellar stretch component λ_k^e using a mapping of the structure tensor to the intermediate configuration by \mathbf{F}_k^v provides several advantages in formulating the constitutive relations. An important one is that it allows the preferred material orientations to be defined only in the reference configuration where it can be experimentally characterized. This is in contrast to some previous internal variable approaches to modeling anisotropic viscoelasticity (see for example [8]) that specifies a description of the material anisotropy in both the reference and intermediate configurations.

To model the anisotropic behavior of the stroma, we assume that the free energy density can be split into an isotropic part that represents the contribution of the matrix and an anisotropic part that represents the collective contribution of the lamellae as follows,

$$W_s(\mathbf{C}, \mathbf{C}_k^e, \mathbf{M}, \tilde{\mathbf{M}}_k) = W_m(\mathbf{C}) + \bar{W}_f(\mathbf{C}, \mathbf{C}_k^e, \mathbf{M}, \tilde{\mathbf{M}}_k). \quad (3.4)$$

The isotropic component W_m depends only upon the stretch tensor \mathbf{C} because we've neglected the relatively soft isotropic viscoelastic response of the proteoglycan matrix. To further simplify matters, the following Neo-Hookean strain energy density

commonly used to model elastomers is assumed for the matrix:

$$W_m^{\text{eq}}(\mathbf{C}) = \frac{\mu}{2}(I_1 - 3) + \frac{\mu}{2\gamma}(I_3^{-\gamma} - 1), \quad \gamma = \frac{\nu}{1 - 2\nu}, \quad (3.5)$$

where ν is the Poisson's ratio in the small strain limit. The parameters $I_1 = \mathbf{C} : \mathbf{1}$ and $I_3 = \det(\mathbf{C})$ are the first and third invariants of the stretch tensor. The latter is directly related the volume change as $I_3 = (\det[\mathbf{F}])^2$. The parameter γ becomes increasingly large as $\nu \rightarrow 0.5$ for a nearly incompressible material. Following the approach of [69], the anisotropic component of the free energy density of the stroma is computed by integrating the free energy density W_f of the individual lamellae over all planar fibril orientation angles θ weighted by the probability density function $D(\theta, \mathbf{X})$:

$$\overline{W}_f(\mathbf{C}, \mathbf{C}_k^e, \mathbf{M}, \widetilde{\mathbf{M}}_k) = \frac{1}{2\pi} \int_{-\pi}^{\pi} W_f(\lambda(\theta), \lambda_k^e(\theta)) D(\theta, \mathbf{X}) d\theta. \quad (3.6)$$

[69] introduced the probability density function to model the preferred planar orientations of the lamellae in the stroma as characterized by wide angle X-ray diffraction experiments (see for example by [12] and [1]).

To model the time-dependent behavior of the collagen lamellae, it is assumed that the free energy density of the lamellae can be decomposed into equilibrium and nonequilibrium components as follows,

$$W_f(\lambda, \lambda_k^e) = W_f^{\text{eq}}(\lambda) + \sum_i^N W_{f_k}^{\text{neq}}(\lambda_k^e). \quad (3.7)$$

Substituting eq. (3.7) into eq. (3.4), we can write the free energy density of the stroma also as the sum of an equilibrium part dependent only on the external variable \mathbf{C} and a nonequilibrium part dependent on \mathbf{C} and the internal variables \mathbf{C}_k^v :

$$W_s = W_m(I_1, I_3) + \underbrace{\frac{1}{2\pi} \int_{-\pi}^{\pi} W_f^{\text{eq}}(\lambda(\theta)) D(\theta, \mathbf{X}) d\theta}_{\overline{W}_f^{\text{eq}}} + \sum_k^N \underbrace{\frac{1}{2\pi} \int_{-\pi}^{\pi} W_{f_k}^{\text{neq}}(\lambda_k^e(\theta)) D(\theta, \mathbf{X}) d\theta}_{\overline{W}_{f_k}^{\text{neq}}}. \quad (3.8)$$

The viscous deformation tensor \mathbf{C}_k^v can be considered the primitive internal state variables in eq. (3.8) because we have assumed that the nonequilibrium part of the free energy density $\sum_k^N \overline{W}_{f_k}^{\text{neq}}$ depends only on the elastic lamellar stretch. The additive decomposition of the stress response into time-independent equilibrium and time-evolving nonequilibrium parts was first proposed by [30] to model stress relaxation in elastomers. Since then, it has been used widely to describe the viscoelastic behavior of elastomers [55, 53, 74, 5] and more recently of soft tissues [6, 8]. In a relaxation experiment, $W_m + \overline{W}_f^{\text{eq}}$ determines the stress response of the stroma in the long-time limit.

The tensile stress-stretch response of the cornea exhibits a J -shaped curve that has been attributed to the straightening and stretching of the collagen fibrils and their associated substructures [60, 72]. We approximate the J -shape stress response of the fibrils by assuming a phenomenological exponential function commonly used for soft-tissues for both the equilibrium and non-equilibrium components of the free energy density of the lamellae:

$$\begin{aligned} W_f^{\text{eq}}(\lambda) &= \alpha^{\text{eq}} \left(\exp[\beta(\lambda^2 - 1)] + \frac{\beta}{\lambda^2} \right), \\ W_{f_k}^{\text{neq}}(\lambda_k^e) &= \alpha_k^{\text{neq}} \left(\exp[\beta(\lambda_k^{e^2} - 1)] + \frac{\beta}{\lambda_k^{e^2}} \right). \end{aligned} \quad (3.9)$$

The parameters $\alpha^{\text{eq}}\beta^2$ and $\alpha_k^{\text{neq}}\beta^2$ represent the equilibrium and nonequilibrium stiffness of the lamellae and β is a shape parameter governing the stiffening of the stress response of the lamellae. In general, different values of β can be used for W_f^{eq} and W_f^{neq} , and this may be desired if the shape of the equilibrium and instantaneous stress-stretch curves are significantly different. A single value is chosen to minimize the number of parameters to be determined from experiments. Preliminary analysis also showed that the best result in fitting the model to the uniaxial tensile experiments is obtained by assuming a single value for β .

Using the standard definition of the second Piola-Kirchhoff stress response $\mathbf{S}_s = 2\frac{\partial W_s}{\partial \mathbf{C}}$, the Cauchy stress of the stroma, $\boldsymbol{\sigma}_s = \frac{1}{\sqrt{I_3}}\mathbf{F}\mathbf{S}_s\mathbf{F}^T$, can be obtained for the free energy in eq. (3.8) as,

$$\begin{aligned} \boldsymbol{\sigma}_s &= \underbrace{\frac{\mu}{\sqrt{I_3}}(\mathbf{b} - I_3^{-\gamma}\mathbf{1})}_{\boldsymbol{\sigma}_m^{\text{neq}}} + \underbrace{\frac{1}{2\pi\sqrt{I_3}} \int_{-\pi}^{-\pi} \frac{\partial W_f^{\text{eq}}}{\partial \lambda} \lambda \mathbf{m} D(\theta, \mathbf{X}) d\theta}_{\boldsymbol{\sigma}_f^{\text{eq}}} \\ &\quad + \underbrace{\sum_k^N \frac{1}{2\pi\sqrt{I_3}} \int_{-\pi}^{-\pi} \frac{\partial W_{f_k}^{\text{neq}}}{\partial \lambda_k^e} \lambda_k^e \mathbf{m} D(\theta, \mathbf{X}) d\theta}_{\boldsymbol{\sigma}_f^{\text{neq}}}, \end{aligned} \quad (3.10)$$

where $\mathbf{b} = \mathbf{F}\mathbf{F}^T$ and $\mathbf{m} = \frac{\mathbf{F}\mathbf{M}\mathbf{F}^T}{\mathbf{C}:\mathbf{M}}$ is the structure tensor of the lamellae in Ω . Note that the same structure tensor \mathbf{m} appears in the expression for the equilibrium and nonequilibrium stress components, $\boldsymbol{\sigma}_f^{\text{eq}}$ and $\boldsymbol{\sigma}_f^{\text{neq}}$, which allows the preferred orientation of the lamellae to be defined in the reference configuration. From eq. (3.10), the lamellar stress can be identified as,

$$\tau_f = \underbrace{\frac{\partial W_f^{\text{eq}}}{\partial \lambda} \lambda}_{\tau_f^{\text{eq}}} + \sum_k^N \underbrace{\frac{\partial W_{f_k}^{\text{neq}}}{\partial \lambda_k^e} \lambda_k^e}_{\tau_{f_k}^{\text{neq}}}, \quad (3.11)$$

which is split also into an equilibrium and N nonequilibrium components.

To evaluate the stress relations, we must specify an evolution equation for the internal stretches λ_k^e . Following the general anisotropic viscoelasticity framework of [62], the following evolution equation is applied for the lamellar viscous stretches,

$$\frac{\dot{\lambda}_k^v}{\lambda_k^v} = \frac{1}{\eta_{f_k}} \tau_{f_k}^{\text{neq}}. \quad (3.12)$$

The elastic component λ_k^e is calculated from λ_k^v and λ using eq. (3.3). To model the stress-dependent creep response observed in experiments, the viscosity exhibited by the lamellae is assumed to depend on the flow stress $\tau_{f_k}^{\text{neq}}$. Specifically, the following phenomenological function is assumed for the viscosity,

$$\eta_{f_k}(\tau_{f_k}^{\text{neq}}) = \eta_{0_k} \left[\frac{\tau_{0_k}}{\tau_{f_k}^{\text{neq}}} \sinh \left(\frac{\tau_{f_k}^{\text{neq}}}{\tau_{0_k}} \right) \right]^{-1}, \quad (3.13)$$

where η_{0_k} is the value of the viscosity in the small strain limit and τ_{0_k} is the activation stress. The exponential form of the viscosity in (3.13) reflects the thermodynamic arguments of Eyring rate kinetics. As the magnitude of the flow stress approaches the activation stress, the viscous resistance decreases causing the rate of viscous deformation of the k th relaxation process to increase. In the limit that $\tau_{0_k} \rightarrow \infty$, the viscosity can be approximated by a constant value $\eta_{f_k} = \eta_{0_k}$.

The corresponding viscous flow rule of the stroma can be determined by noting that the nonequilibrium stress response in eq. (3.10) can be written using the lamellar flow rules in eq. (3.12) as,

$$\boldsymbol{\sigma}_s^{\text{neq}} = \sum_k^N \frac{1}{2\pi\sqrt{I_3}} \int_{-\pi}^{-\pi} \eta_{f_k} \frac{\dot{\lambda}_k^v}{\lambda_k^v} \mathbf{m} D(\theta, \mathbf{X}) d\theta, \quad (3.14)$$

With some algebraic manipulation (see Section 3.2.2), it can be shown that,

$$\frac{\dot{\lambda}_k^v}{\lambda_k^v} = \lambda_k^{e^2} \mathbf{b}_k^{e^{-1}} \mathbf{m} : \left(-\frac{1}{2} \mathcal{L}_v \mathbf{b}_k^{e^{-1}} \right) \mathbf{b}_k^{e^{-1}}, \quad (3.15)$$

where $\mathbf{b}_k^e = \mathbf{F}_k^e \mathbf{F}_k^{eT}$ and $\mathcal{L}_v \mathbf{b}_k^e = \overline{\mathbf{F} \mathbf{C}_k^{v^{-1}} \mathbf{F}^T}$ is an objective time derivative of \mathbf{b}_k^e . Substituting eq. (3.15) into eq. (3.14) gives,

$$\boldsymbol{\sigma}_s^{\text{neq}} = \sum_k^N \frac{1}{\sqrt{I_3}} \underbrace{\left[\frac{1}{2\pi} \int_{-\pi}^{-\pi} \eta_{f_k} \lambda_k^{e^2} \mathbf{m} \otimes \mathbf{m} D(\theta, \mathbf{X}) d\theta \right]}_{\mathcal{V}_{f_k}} : \mathbf{b}_k^{e^{-1}} \left(-\frac{1}{2} \mathcal{L}_v \mathbf{b}_k^{e^{-1}} \right) \mathbf{b}_k^{e^{-1}}. \quad (3.16)$$

The tensor \mathcal{V}_{f_k} is the effective viscosity for the k th nonequilibrium process that relates the nonequilibrium stress $\boldsymbol{\sigma}_s^{\text{neq}}$ to the viscous rate of deformation $\mathbf{b}_k^{e^{-1}} \left(-\frac{1}{2} \mathcal{L}_v \mathbf{b}_k^{e^{-1}} \right) \mathbf{b}_k^{e^{-1}}$ of the stroma. It can be considered to be associated loosely with the k th dashpot in Fig. 3.1. The viscosity of the stroma is calculated from a homogenization of the

characteristic viscosities of the lamellae and thus includes a description of the fibril distribution. Finally, the viscous dissipation of the stroma associated with the homogenized viscous flow rule in eq. (3.16) is,

$$\overline{D}_f^v = \frac{1}{2\pi} \int_{-\pi}^{\pi} \underbrace{\sum_k^N \tau_{f_k}^{\text{neq}} \left(\frac{\dot{\lambda}_k^v}{\lambda_k^v} \right)}_{D_f^v} D(\theta, \mathbf{X}) d\theta \geq 0. \quad (3.17)$$

As with the anisotropic component of the free energy density \overline{W}_f in eq. (3.8), \overline{D}_f^v is a homogenization of the viscous dissipation D_f^v exhibited by the lamellae.

3.2.2 Flow rate

This section demonstrates the relationship between the viscous lamellar stretch rate and the Lie time derivative of the stretch tensor $\mathbf{b}_k^e = \mathbf{F}_k^e \mathbf{F}_k^{eT}$ of the stroma. The viscous lamellar stretch rate can be computed from the definition of the viscous lamellar stretch in eq. (3.3) as,

$$2\dot{\lambda}_k^v \lambda_k^v = \dot{\mathbf{C}}_k^v : \mathbf{M}. \quad (3.18)$$

The rate of \mathbf{C}_k^v can be expressed in terms of the viscous rate of deformation tensor $\mathbf{D}_k^v = \dot{\mathbf{F}}_k^v \mathbf{F}_k^{v-1}$ as follows:

$$\mathbf{D}_k^v = \frac{1}{2} \left(\dot{\mathbf{F}}_k^v \mathbf{F}_k^{v-1} + \mathbf{F}_k^{v-T} \dot{\mathbf{F}}_k^{vT} \right) = \frac{1}{2} \mathbf{F}_k^{v-T} \dot{\mathbf{C}}_k^v \mathbf{F}_k^{v-1}. \quad (3.19)$$

Then combining eqs. (3.18) and eq. (3.19), the viscous stretch rate can be related to \mathbf{D}_k^v as,

$$2\lambda_k^v \dot{\lambda}_k^v = \mathbf{D}_k^v : \widetilde{\mathbf{M}}_k \quad (3.20)$$

Finally, the tensor \mathbf{D}_k^v can be expressed in the spatial configuration as,

$$\mathbf{D}_k^v = -\frac{1}{2} \mathbf{F}_k^{e-1} (\mathcal{L}_v \mathbf{b}_k^e) \mathbf{F}_k^{eT}, \quad (3.21)$$

where $(\mathcal{L}_v \mathbf{b}_k^e) = \mathbf{F}(\overline{\dot{\mathbf{C}}_k^v}) \mathbf{F}^T$. Then, the final relation in eq. (3.20) can be expressed equivalently as,

$$\frac{\dot{\lambda}_k^v}{\lambda_k^v} = -\frac{1}{2} \mathbf{b}_k^{e-1} (\mathcal{L}_v \mathbf{b}_k^e) \mathbf{b}_k^{e-1} : \lambda_k^{e2} \mathbf{m}. \quad (3.22)$$

3.2.3 Parameter Fitting

To evaluate the performance of the nonlinear anisotropic viscoelastic model, the stress relation in equation (3.10) and evolution equation (3.16) were implemented in a finite element program and applied to simulate the uniaxial tensile cyclic and creep experiments previously conducted by our group on excised corneal strips. The experimental setup, methodology and results were described in detail in [14]. To simulate the cyclic experiments, the stress was applied using a ramped (constant rate) load and unload function. For the creep simulations, the applied stress was ramped to the prescribed value and held for the loading time exhibited by experiments. To determine parameters representative of the tested tissue, we made a number of assumptions and we devised a rational, sequential fitting procedure for the remaining parameters based on standard Newton-Raphson searches with least squares error norms.

For the properties of the proteoglycan matrix, we chose an arbitrary small shear modulus $\mu = 10$ kPa and large $\gamma = 30.0$ to approximate the weak in-plane deviatoric response relative to the fibrils and incompressibility of the matrix. This value of γ corresponded to a small-strain Poisson's ratio of $\nu = 0.492$. These assumptions were warranted since the properties of the proteoglycan matrix by itself were very hard to measure using conventional mechanical tests.

All of the tensile strip tests sampled only the response of the central cornea region which we assumed had a particular fibril distribution. Because the fibril arrangement for bovine cornea has not been characterized, we applied the model of the fibril density function developed by [69] for the central cornea of humans from the wide angle scattering experiments of [1]:

$$D(\theta) = \cos^8(\theta) + \sin^8(\theta) + 0.454. \quad (3.23)$$

The fibril distribution function is plotted in Fig. 3.2(a). For the central cornea. The preferred fibril directions are aligned with the nasal-temporal (NT) and inferior-superior (IS) meridians, which is consistent with X-ray scattering experiments that show that both meridians exhibit the same fibril density. This preferential fibril alignment lies on top of a base-line isotropic value of 0.579 that represent the density of the population of fibrils equally distributed in all directions. Thus in the central region, we expect the cornea to behave approximately as a transversely isotropic material.

To obtain the remaining parameters associated with the lamellae, the constitutive model first was fitted to the loading part of the averaged stress-strain curve for the 350kPa/s uniaxial tensile tests. The stress-strain response of the highest rate cyclic test was chosen to estimate the instantaneous (short-time) elastic properties because it exhibited minimal hysteresis. Here, we assumed that viscous deformation would be negligible so that all the elastic elements (i.e, the springs in the rheological model in Fig. 3.1) act in parallel. The fit, shown in Fig. 3.3(a), gave a value for a collective $\bar{\alpha} = \alpha^{\text{eq}} + \sum_k^3 \alpha_k^{\text{neq}} = 0.835$ kPa and $\beta = 38.1$, which was assumed earlier to be

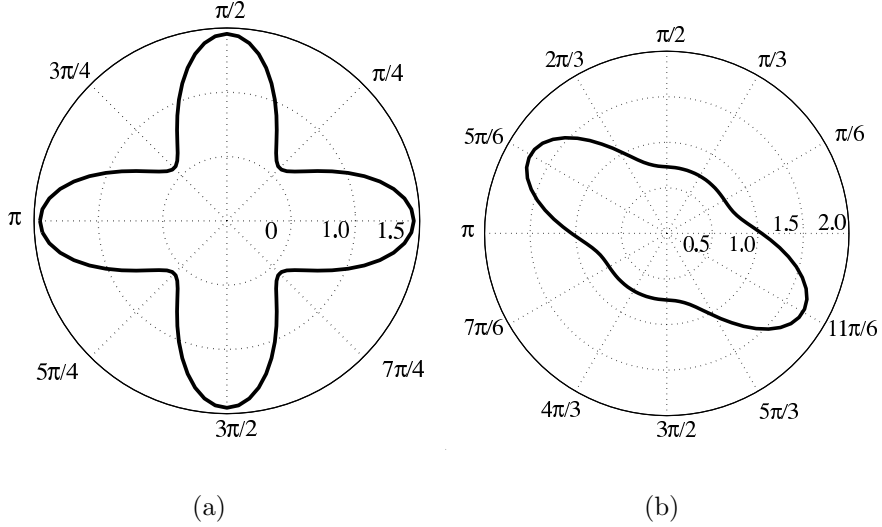
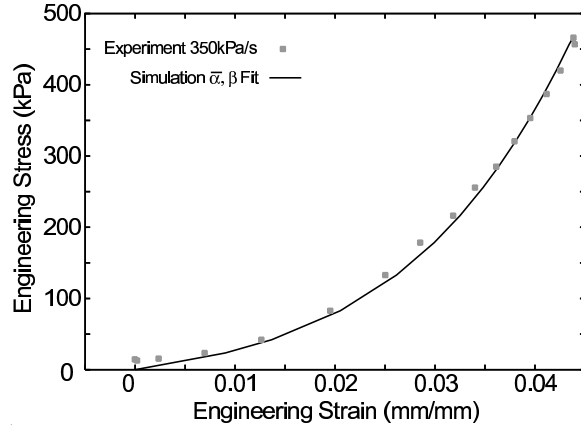


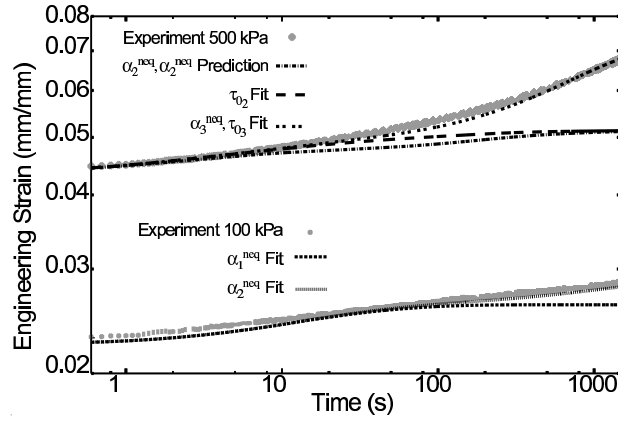
Figure 3.2. Probability density function for the preferred in-plane orientation of collagen fibrils developed by [69] for the human cornea for (a) the central cornea region, and (b) a region in the limbus. The 0° and 90° orientations corresponds to the nasal-temporal and inferior-superior meridians.

common across equilibrium and nonequilibrium components. In Fig. 3.3(a), the engineering strain plotted was computed from F_{22} , which was the normal component of the deformation gradient in the loading direction, while the engineering stress was the product of F_{22} and the normal component of the second Piola-Kirchhoff stress S_{22} in the loading direction.

Next, we used the averaged strain-time curves for the 100kPa and 500kPa uniaxial creep tests to determine the elastic and viscous properties of the individual components of the cornea model. For the creep strains observed in the experiments, the effect of each of the k exponential-based nonequilibrium processes, analogous to the Maxwell elements in Fig. 3.1, was most significant in time span of roughly a decade. Thus, at least three nonequilibrium processes with increasing characteristic retardation times were needed to model the time-dependent behavior of the corneal strips within the time span of the creep experiments. For simplicity, we used an equally spaced distribution of retardation times $t_k = (10^2, 10^4, 10^6)$ s. The characteristic retardation times were defined by linearizing the constitutive equations (3.10) and (3.16) about the reference state. The creep experiments showed that the response became significantly nonlinear only for larger times $t > 100$ s. Thus, the activation stress for the first element, $k = 1$, was assumed to be significantly larger than the applied stresses (i.e. $\tau_{0_1} \rightarrow \infty$), and a constant viscosity $\eta_1 = \eta_{0_1}$ was used. This simplification reduced the number of parameters and was consistent with the creep experiments which showed a nearly quasilinear response for small times $t < 100$ s.



(a)



(b)

Figure 3.3. A sequence of simulations showing (a) the initial fit of the elastic parameters ($\bar{\alpha} = \alpha^{\text{eq}} + \sum_k^3 \alpha_k^{\text{neq}}, \beta$) using the 350 kPa/s rate data, and (b) fits of α_1^{neq} and α_2^{neq} to the 100 kPa creep data; a prediction of the 500 kPa creep data using only the $\alpha_1^{\text{neq}}, \alpha_2^{\text{neq}}$ fit; and fits of τ_2 and $(\alpha_3^{\text{neq}}, \tau_3)$ to the 500 kPa creep data.

Since each of the $k = 1..3$ nonequilibrium processes produced significant creep strains in different time frames, we fitted each independently and in sequence using standard Newton-Raphson searches with least squares error norms. First, α_1^{neq} was determined using the initial $t < 100\text{s}$ portion of the low stress 100 kPa creep data. Here, as in the high rate case, elements $k = 2,3$ behaved essentially elastically and their responses were lumped with the equilibrium element. Using this fact, the definition of the characteristic retardation times t_k and the instantaneous uniaxial creep moduli E_k , the viscosities were parameterized as $\eta_{0k} = E_k t_k$. For $k = 1$, $E_k = (1/\bar{\alpha}_k + 1/\alpha_k^{\text{neq}})^{-1} \beta(\beta + 2)$ and $\bar{\alpha}_1 = \alpha^{\text{eq}} + \alpha_2^{\text{neq}} + \alpha_3^{\text{neq}} = \bar{\alpha} - \alpha_1^{\text{neq}}$. The parameter α_2^{neq} was fitted in a similar fashion to the $t > 100\text{s}$ portion of the 100kPa creep data with the constraint $\alpha_1^{\text{neq}} + \alpha_2^{\text{neq}} + \bar{\alpha}_2 = \bar{\alpha}$ to maintain the initial stiffness found in the elastic fit shown in Fig. 3.3(a). The resulting parameters $\alpha_1^{\text{neq}} = 0.221$ kPa, $\alpha_2^{\text{neq}} = 0.141$ kPa, $\eta_{01} = 6.38 \times 10^4$, and $\eta_{02} = 5.39 \times 10^6$ elicited a nearly linear response over log-time as shown in Fig. 3.3(b) that was characteristic of the low stress creep data.

To fit the remaining parameters, $\tau_{02}, \tau_{03}, \alpha_3^{\text{neq}}$, and α^{eq} the high stress 500 kPa creep data was employed. Lower bounds on the activation stresses τ_{02} and τ_{03} were chosen so as not to significantly affect the fit to the 100kPa creep data. Next, τ_{02} was fit to the $10\text{s} < t < 100\text{s}$ time range of the high stress creep data. Lastly, α_3^{neq} and τ_{03} were fit $t > 100\text{s}$ portion of the 500kPa creep data. The parameter α^{eq} was recovered using the constraint $\bar{\alpha} = \alpha^{\text{eq}} + \alpha_1^{\text{neq}} + \alpha_2^{\text{neq}} + \alpha_3^{\text{neq}}$. Figure 3.3(b) illustrates how the sequential fitting of each parameter brings the simulations closer to the experimental data, as well as the range of action of each parameter.

In summary, fits to loading portion of the 350kPa/s rate data and the 100 kPa and 500 kPa creep data resulted in the following material parameters: $\beta = 38.1$, $\alpha^{\text{eq}} = 0.0667$ kPa, $\alpha_k^{\text{neq}} = (0.221, 0.141, 0.405)$ kPa, $\eta_{0k} = (6.38 \times 10^4, 5.39 \times 10^6, 3.49 \times 10^8)$ kPa-s, $\tau_{02} = 20.9$ kPa., and $\tau_{03} = 102.$ kPa. With these parameters, the model was used to predict the strain-time response of the 350 kPa creep test and the 3.5 kPa/s and 35 kPa/s cyclic tensile tests.

3.3 Results of Uniaxial Tensile Simulations

The results from the uniaxial creep simulations and experiments at the three different stress levels, (100, 350, 500)kPa, obtained for the central portion of NT corneal strips, are plotted in Figure 3.4. The error bars indicate a plus/minus one standard deviation from the averaged experimental results. The model provided a good quantitative prediction of the creep measurements, and differences between data and simulation results were well within one standard deviation. Recall that the parameters of the viscosity were only fitted to the data for the highest and lowest stress levels, yet the model was able to predict the creep data for the intermediate 350kPa stress level to within experimental variation.

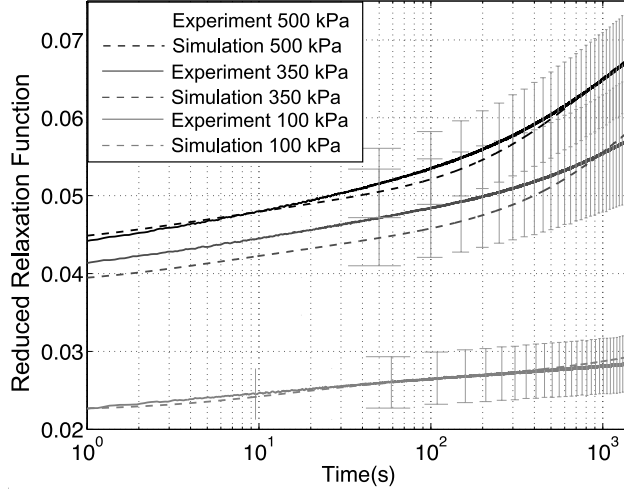


Figure 3.4. Uniaxial creep strain curves obtained from experiments and simulation at three different applied engineering stresses for the central portion of corneal strips cut along the nasal-temporal (NT) direction. The error bars indicate a ± 1 standard deviation from the bin-averaged experimental data. The nonlinear viscoelastic model is fitted to 100 kPa and 500 kPa creep data and used to predict 350 kPa data.

The strain-time curves obtained from cyclic uniaxial tensile experiments and simulations at three different stress rates (3.5, 35, 350)kPa/s for the central portion of NT corneal strips are shown in Figure 3.5(a)-3.5(c). Recall that only the loading curve for the 350 kPa/s case was used in fitting the parameters for the short-time elastic response. In general, the rate-dependent response predicted by the nonlinear viscoelastic model agreed well with the experimental data for both the loading and unloading portion of the strain-time curve. Figure 3.5(d) plots the experimental data and simulation results for the 35kPa/s uniaxial tension cyclic tests comparing the deformation response of the NT and IS orientations for the central cornea. The experimental results for the two orientations were similar in that the differences between the two were significantly smaller than the experimental error of either data set (see [14] for more details). As expected, the simulation results for the two orientations were identical because the probability function, plotted in Fig. 3.2(a), used to model the density of the collagen fibrils in the central cornea exhibited rotational symmetry about 90° . Consequently, the fibril distribution was the same when viewed from the NT and IS meridians.

To examine further the anisotropic time-dependent behavior of the model, the uniaxial tensile stress and time response was computed for the probability density function,

$$D(\theta) = \sin^8(\theta - 4\pi/3) + 0.727, \quad (3.24)$$

developed by [69] for a region in the limbus of the human cornea from the X-ray

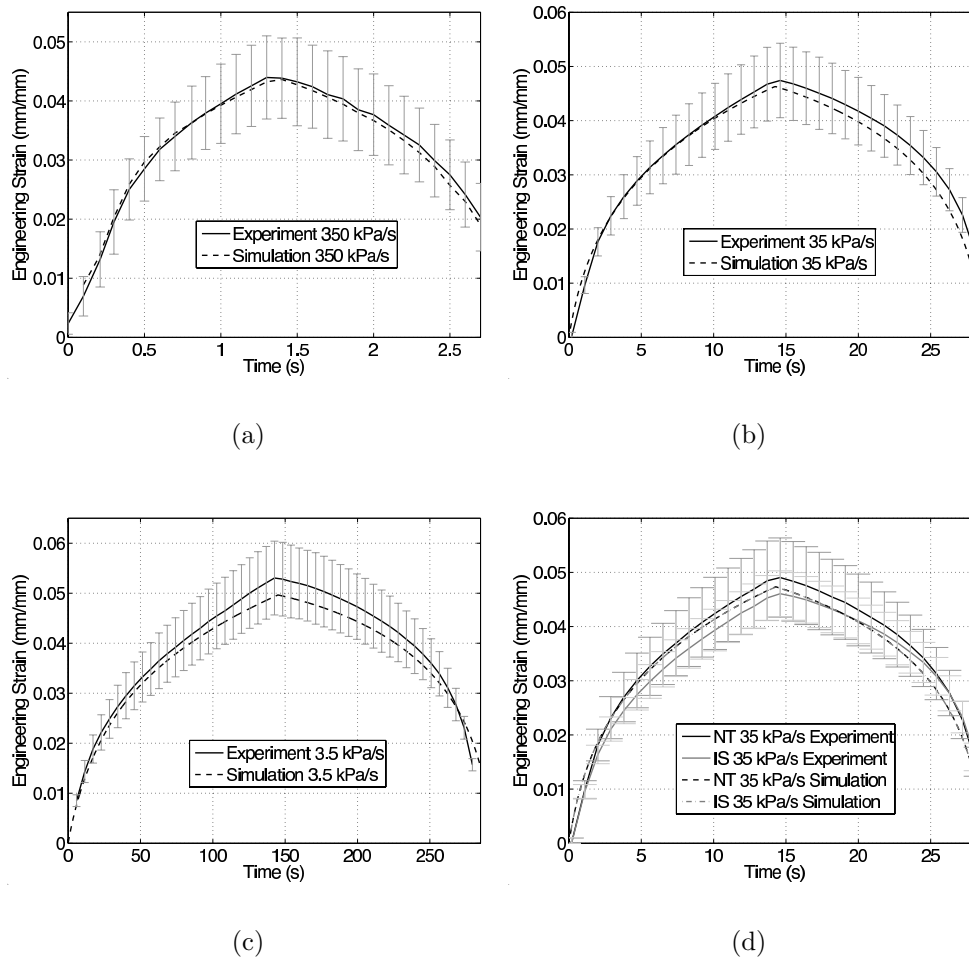
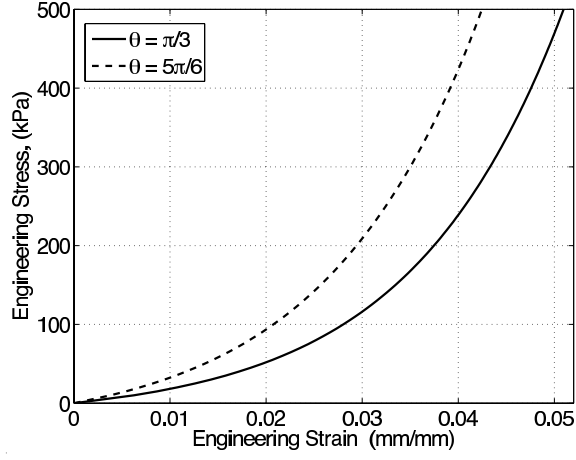
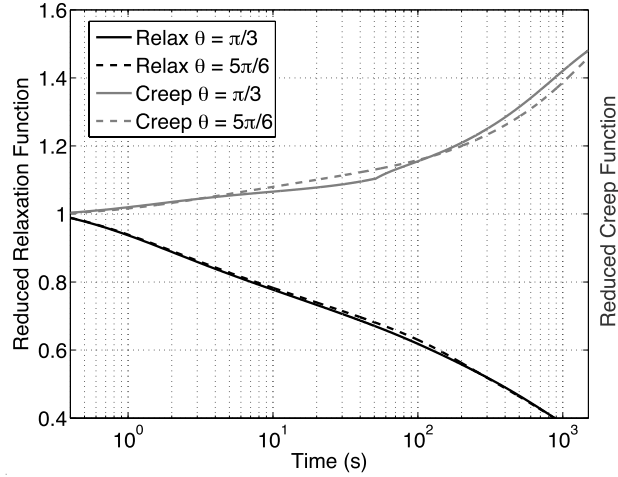


Figure 3.5. Cyclic strain-time plot obtained from uniaxial tension experiments and simulations at three different stress rates: (a) 350 kPa/s for the NT orientation, (b) 35 kPa/s for the NT orientation, (c) 3.5 kPa/s for the NT orientation, and (d) 35 kPa/s comparing the NT and IS orientations. Error bars indicate a ± 1 standard deviation from the bin-averaged experimental data. The nonlinear viscoelastic model is fitted to the loading curve of 350 kPa/s and creep data and used to predict response of lower stress rates.



(a)



(b)

Figure 3.6. Anisotropic behavior of nonlinear viscoelastic model calculated for the fibril density function in eq. (3.24): (a) stress-strain response at 500kPa/s and (b) reduced relaxation function for $\lambda = 1.04$ and reduced creep function for 500kPa. The angles $\theta = 5\pi/3$ and $\theta = \pi/3$ indicates orientations with highest and lowest fibril density.

scattering intensity data of [1]. The same viscoelastic model parameters obtained from tensile strip experiments of the central region were used. In the limbus, the preferred orientations of the fibrils were aligned in the circumferential direction. The density function, plotted in Fig. 3.2, was maximum at $\theta = 5\pi/6$ and minimum at $\theta = \pi/3$. Figure 3.6(a) plots the stress-strain response of the two orientations for a high applied stress rate 5000kPa/s. Figure 3.6(b) shows the uniaxial creep response for a 500kPa applied engineering stress and uniaxial relaxation response for an applied stretch $F_{22} = 1.05$ for the stiff $\theta = 5\pi/6$ and soft $\theta = \pi/3$ orientations. The results were normalized by the instantaneous values (at $t \rightarrow 0$) to obtain the reduced relaxation and creep functions. The instantaneous creep strains were 4.3% and 5.1% while the instantaneous relaxation stresses were 806kPa and 459kPa respectively for the $5\pi/6$ orientation and $\pi/3$ orientations. As expected, the $\theta = 5\pi/6$ orientation with the higher fibril density exhibited a significantly stiffer stress-strain response. However, both orientations exhibited similar time-dependent behavior in that the reduced creep relaxation functions were nearly identical for the entire time range.

The results indicate that though the model exhibits anisotropy in the stress-strain behavior, its time-dependent behavior is insensitive to the fibril anisotropy. This apparent isotropy in the time-dependent response is the direct consequence of the assumption in the model that the in-plane stress response of the matrix is significantly softer than the homogenized in-plane response of the lamellae, and that the viscous stretching of the lamellae is the primary mechanism for the time-dependent response of the stroma. As a first-order approximation, we can consider that the creep and stress relaxation response of the model is governed by the relaxation time given by the ratio of the viscosity of the material to its stiffness. This is exactly true in the limit of small strains. Because the model assumes that the viscoelastic behavior of the stroma originates from the viscoelastic stretching of the lamellae, the viscous stretch rate of the lamellae is homogenized in the same manner as the elastic stretch of the lamellae to calculate the nonequilibrium stress component. This is clearly observed by comparing the equivalent expressions for σ_s^{neq} in eqs. (3.10) and (3.14). Thus, the viscosity tensor relating the viscous stretch rate to σ_s^{neq} and the stiffness tensor relating the elastic stretch to σ_s^{neq} possess the same material anisotropy. The characteristic relaxation time in the small-strain limit is $\xi_k = \eta_{0_k} / (4\alpha_k^{\text{neq}}\beta(\beta + 2))$ for all orientations. The differences between the time-dependent response of the $5\pi/6$ and $\pi/3$ orientations in Fig. 3.6(b) are caused by kinematic nonlinearity and the stress-dependence of the softening lamellar viscosity model.

3.4 Discussion

A constitutive model was developed for the anisotropic and nonlinear viscoelastic tensile behavior of the cornea. The model attributes the time-dependent behavior of the cornea primarily to the viscoelastic stretching of the lamellae forming the stroma. It is hierarchical in that the stress and viscous flow response at the tissue level are calcu-

lated by homogenizing the stress and viscous flow response at the level of individual lamellae. This is the main feature distinguishing the model from previous models for the anisotropic viscoelasticity of soft fiber-reinforced tissues, most of which develop relations for the anisotropic viscous flow of the tissue as a whole. As a consequence of this approach, the model parameters are related directly to the properties, such as moduli and viscosities, of the constituent materials and the lamellar arrangement. The former can be determined from mechanical tests such as uniaxial strip tests, while the latter can be determined from microstructural characterization experiments such as X-ray scattering. In general, the constitutive framework can be applied to model the anisotropic viscoelastic response of other soft fiber-reinforced tissues such as the elastic arteries. The formulation of the model also provides for a simple and efficient numerical implementation for finite element analysis.

With some simplifying assumptions, we devised a sequential fitting procedure for the model parameters governing the nonlinear time-dependent behavior. The parameters associated with the material anisotropy were obtained by fitting to the X-ray scattering data for the distribution of collagen fibrils in the human cornea [69]. The short-time elastic parameters of the model were fitted to the loading portion of the stress-strain curve of a high rate cyclic uniaxial tensile test and the viscous parameters were fitted to the creep-time curves of a high and low applied stress uniaxial creep test of excised corneal strips. Given the large number of parameters that needed to be determined, we believe the gains in efficiency and robustness by using the devised sequential procedure, which employed at most two dimensional searches, more than offset the potential for bias. The fitted parameters then were applied to predict successfully the stress-strain curves of cyclic tensile tests at an intermediate and low stress rate and the creep-time curve of an intermediate applied stress. The agreement between the data and simulations were well within the experimental error. For the creep test, the model was able to reproduce the observed nonlinear stress-dependence of the strain-time curves in which the creep rate increased with the applied stress. It was shown in [14] that the same behavior could not be captured by the Fung quasilinear viscoelastic model. For the cyclic tests, the model consistently predicted a slightly faster unloading response, leading to smaller hysteresis in the cyclic stress-strain curves than observed in experiments. The difference in the measured and calculated unloading response increased with decreasing strain rate and may have reflected the effects of tissue swelling which was not included in the model. The model also predicted the same stress-strain response for the NT and IS orientations which was consistent with the results of the tensile strip tests.

The model was applied also to calculate the uniaxial stress-strain and time-dependent response of a region in the limbus, which exhibited more anisotropy than the central region. The same model parameters obtained from tensile strip experiments of the central region was used for the simulations of the limbus, only a different fibril density distribution was applied. As expected, the results showed that the cornea displayed a strongly anisotropic stress-strain response in the limbus. However, the time-dependent response as given by the reduced creep and relax functions, which

normalized out the elastic anisotropy, did not display a strong orientation dependence. The apparent isotropy in the time-dependent part of the creep and relaxation response was because (1) the collagen phase exhibited a base-line isotropic response that was significantly stiffer than the response of the matrix, and (2) the viscoelastic behavior of the stroma was dominated by the viscoelastic stretching of the lamellae. There are distinct advantages for the structural performance of the cornea to exhibit a strongly anisotropic stress-strain response but a time-dependent response that preserves the material symmetry. The anisotropic stress-strain response is needed for structural reinforcement of regions experiencing high stresses. For example, it is hypothesized that the additional fibril reinforcement in the circumferential direction of the limbus is needed to effect a change in corneal curvature from the dome-shaped central cornea to the flatter sclera [1]. If this anisotropy is manifested also in the time-dependent response, then the cornea as a membrane-like structure risks buckling in regions that exhibit faster stress relaxation or slower creep.

Because of the limitations of the experimental set-up of the tensile strip test, we were unable to measure the stress-strain response of the limbus and peripheral cornea. However, we are currently validating the anisotropic stress-strain and time-dependent behavior of the model by performing bulge experiments and corresponding finite element simulations of the intact cornea. The bulge experiments subject the intact cornea to constant rate cyclic loading, volume controlled relaxation, and pressure control creep while measuring the displacement field of the anterior surface using digital image correlation. The finite element calculations will compare the time-dependent displacement field predicted by the model and measured from the bulge experiments. This will allow us to validate the anisotropic stress/strain response and symmetry-preserving time-dependent behavior, as shown in Fig. 3.6, predicted by the model.

Chapter 4

Modeling the Anisotropic Finite-Deformation Viscoelastic Behavior of Soft Fiber-Reinforced Composites

This chapter presents constitutive models for the anisotropic, finite-deformation viscoelastic behavior of soft fiber-reinforced composites. An essential assumption of the models is that both the fiber reinforcements and matrix can exhibit distinct time-dependent behavior. As such, the constitutive formulation attributes a different viscous stretch measure and free energy density to the matrix and fiber phases. Separate flow rules are specified for the matrix and the individual fiber families. The flow rules for the fiber families then are combined to give an anisotropic flow rule for the fiber phase. This is in contrast to many current inelastic models for soft fiber-reinforced composites which specify evolution equations directly at the composite level. The approach presented here allows key model parameters of the composite to be related to the properties of the matrix and fiber constituents and to the fiber arrangement. An efficient algorithm is developed for the implementation of the constitutive models in a finite-element framework, and examples are presented examining the effects of the viscoelastic behavior of the matrix and fiber phases on the time-dependent response of the composite.

4.1 Introduction

Soft fiber-reinforced composites are a class of materials usually composed of polymeric fibers organized in a soft polymeric matrix. These materials have important applications in both engineering and biomechanics. Examples of soft engineering fiber-reinforced composites include woven fabrics for impact protection and containment, and laminate composites for automotive tires, hoses, and belts. In biomechanics, soft fiber-reinforced composites describe most soft tissues that serve a structural and/or protective function such as the cornea, skin, tendons, ligaments, and blood vessels. Because of their fiber-reinforced microstructure, these materials are extraordinarily

stiff and strong for their weight. Many soft fiber-reinforced composites also possess a unique combination of flexibility and toughness that is exploited for energy-absorbing and protective applications. The toughness of these materials arises from the ability of both the fiber and matrix constituents to dissipate energy through large inelastic deformation.

The area of phenomenological modeling of the anisotropic finite-inelastic behavior of soft fiber-reinforced composites has been focused mainly on the viscoelastic behavior of soft tissues, though there have been some recent attention given to the elastic-plastic behavior of soft engineering fabrics and laminates [73, 75, 48]. A number of these models are extensions of isotropic formulations that include a description of the preferred fiber orientation using the structure tensor method pioneered by [26, 84], and [79]. [52] extended the approach of [70] to incorporate an explicit dependence of the invariants of the Cauchy-Green deformation rate tensor and structure tensors in the stress response. The anisotropic viscoelastic model of [39] is an extension of the isotropic convolution integral formulation developed by [37] to include a dependence of the equilibrium stress and overstress response on the invariants of the Cauchy-Green deformation and structure tensors. A more physically-based model has been developed by [8] for highly extensible soft tissues such as skin that combines the isotropic viscoelastic model of [5] for elastomers and the orthotropic hyperelastic model of [7]. The model attributes the large-deformation time-dependent behavior of the composite to the entropic and reptation mechanisms of the constituent long-chain (bio)polymer molecules. The viscoelastic formulation applies a multiplicative decomposition of the deformation gradient into elastic and viscous parts. The latter is an internal variable for the viscous relaxation of the composite material.

The internal variable approach using the multiplicative decomposition of the deformation gradient has been applied widely and successfully to model the isotropic finite-inelastic behavior of polymers. However, applying the internal variable approach to anisotropic finite-inelasticity raises important questions of how to describe the material anisotropy in the intermediate configuration. The model of [7] effectively specifies the material anisotropy in both the intermediate and reference configurations by requiring that the preferred material orientations remain the same in the two configurations. The elasto-plastic model of [73] for fabric-reinforced composites specifies the structure tensors in the reference configuration and transforms them to the intermediate configuration using the plastic part of the deformation gradient. [75] applies a mixed transformation of the structure tensor using the viscous part of the deformation gradient and its inverse. The formulation of [73] leads to the constitutive relations being independent of the rotational components of the plastic deformation gradient, which serves a practical purpose of simplifying the numerical implementation. However, the advantages of the various approaches and their physical significance have not been fully explored.

This chapter presents constitutive models for the finite-deformation anisotropic, viscoelastic behavior of soft fiber-reinforced composites. First, a general formulation is

developed in which the composite material is represented as a continuum mixture consisting of various fiber families embedded in an isotropic matrix. The orientation of the fiber families are described in the reference configuration using structure tensors. The different material phases are required to deform affinely with the continuum deformation gradient. However, the model attributes to each phase a different viscous stretch measure by assuming parallel multiplicative decompositions of the deformation gradient into elastic and viscous parts. The structure tensors of the fiber families are mapped to the intermediate configuration using the viscous deformation gradient of the fiber phase.

From the general formulation, two specific models are developed. The first considers a composite material with an arbitrary number of fiber families and formulates the constitutive response of the fiber phase only in terms of the total and elastic fiber stretches. The model specifies an isotropic evolution equation for the viscous deformation of the matrix phase and separate evolution equations for the viscous stretch of the fiber families. The latter is the primary novelty of the approach developed here. Unlike other phenomenological anisotropic viscoelastic models, an anisotropic evolution equation is not specified directly for the viscous stretch of the fiber phase (or the composite material) as whole, but instead is developed by homogenizing the flow rules of the individual fiber families. This approach naturally incorporates a description of the fiber arrangement into the effective viscous resistance of the fiber phase and allows the model to consider a composite material with an arbitrary number of fiber families. The second model is developed specifically for a composite material with two fiber-families, but it considers the effects of additional fiber reinforcements under shear loadings through a dependence of the free energy density on higher order invariants of the stretch and structure tensors. As for the first model, flow rules are developed for the viscous stretch of the fiber families for the orthotropic case. These are combined to provide an evolution equation for the viscous deformation of the fiber phase. In essence, the main accomplishment of this chapter is the development of homogenization schemes to calculate the anisotropic viscous response of the fiber-reinforced composite from the viscous response of the fiber families that is consistent with the homogenization scheme widely used in finite-elasticity to evaluate the anisotropic stress response of the composite from that of the fiber families.

The general constitutive framework for modeling the anisotropic, finite-deformation, viscoelastic behavior of soft fiber-reinforced composites is presented in Sec. 4.2 along with the developments of specific models for the N fiber-families and two fiber-families composites. A scheme for the numerical implementation of the models in a finite element framework is presented in Section 4.3. The capabilities of the models are demonstrated in Sec 4.7 for simple examples of creep and relaxation of an orthotropic composite material and cyclic inflation of a laminated thick-wall tube. The results demonstrate that for a composite material with relatively stiff fiber phase in a soft matrix, the time-dependent behavior of the fibers dominates the in-plane time-dependent behavior of the composite while the time-dependent behavior of the matrix plays a more prominent role in determining the time-dependent out-of-plane response.

4.2 Model Developments

4.2.1 Kinematics

Consider a continuum body, denoted in the reference (undeformed) configuration as Ω_0 , consisting of a variety of fiber families, F_α for $\alpha = 1..N$, embedded in an isotropic matrix, M . A fiber family is defined as a collection of fibers sharing the same material composition and unit orientation vector $\mathbf{P}_\alpha(\mathbf{X})$ which can vary with the material position $\mathbf{X} \in \Omega_0$. Following [79], a structure tensor $\mathbf{M}_\alpha := \mathbf{P}_\alpha \otimes \mathbf{P}_\alpha$ is defined for each fiber family to facilitate calculation of the fiber stretch. The spatial (deformed) configuration of the body is denoted by Ω and the position of a spatial point $\mathbf{x} \in \Omega$ at time t is defined by the deformation map $\phi(\mathbf{X}, t)$. The tangent of ϕ defines the deformation gradient $\mathbf{F} := \frac{\partial \phi}{\partial \mathbf{X}}$ of the continuum body. It is assumed that both the matrix and fiber phases deform with the continuum deformation gradient \mathbf{F} . This assumption allows the deformed fiber vector of F_α to be calculated as,

$$\lambda_\alpha \mathbf{p}_\alpha = \mathbf{F} \mathbf{P}_\alpha, \quad (4.1)$$

where λ_α is the fiber stretch and \mathbf{p}_α is the unit fiber orientation vector in Ω . The fiber stretch is calculated from eq. (4.1) as,

$$\lambda_\alpha = \sqrt{\mathbf{C} : \mathbf{M}_\alpha}, \quad (4.2)$$

where $\mathbf{C} = \mathbf{F}^T \mathbf{F}$ is the right Cauchy-Green deformation tensor. The stretch rate of F_α can be calculated from eq. (4.2) as $2\dot{\lambda}_\alpha \lambda_\alpha = \dot{\mathbf{C}} : \mathbf{M}_\alpha$. Defining a unit structure tensor for the fiber family in Ω as,

$$\mathbf{m}_\alpha := \mathbf{p}_\alpha \otimes \mathbf{p}_\alpha = \frac{\mathbf{F} \mathbf{M}_\alpha \mathbf{F}^T}{\mathbf{C} : \mathbf{M}_\alpha}, \quad (4.3)$$

the fiber stretch rate can be evaluated alternatively using the spatial rate of deformation tensor $\mathbf{d} = \text{sym} \left[\dot{\mathbf{F}} \mathbf{F}^{-1} \right]$ from the relation,

$$\frac{\dot{\lambda}_\alpha}{\lambda_\alpha} = \mathbf{d} : \mathbf{m}_\alpha. \quad (4.4)$$

In modeling the viscoelastic behavior of hard composites with high-strength brittle fibers, such as graphite and glass, the fibers are usually considered elastic and the time-dependent response of the composite is attributed solely to the time-dependent behavior of the matrix material. However for soft composites, the fiber reinforcements can exhibit a significant time-dependent response. For example, experiments have shown that the mechanical behavior of collagen and elastin fibers, the primary structural elements in many fiber-reinforced soft tissues, is time-dependent [28]. To incorporate the time-dependent behavior of both the matrix and fiber phases in the viscoelastic model of the soft fiber-reinforced composite material, separate parallel

multiplicative decompositions of the deformation gradient into viscous and elastic parts are assumed for the matrix and fiber phases as,

$$\mathbf{F} = \mathbf{F}_M^e \mathbf{F}_M^v = \mathbf{F}_F^e \mathbf{F}_F^v. \quad (4.5)$$

Note that the parallel decompositions applies to the fiber phase and not to the fiber families, though this may be desired if the viscous properties of the fiber families are vastly different. Moreover, multiple relaxation processes can be incorporated for either phases by expanding eq. (4.5) to $\mathbf{F} = \mathbf{F}_{M_k}^e \mathbf{F}_{M_k}^v = \mathbf{F}_{F_l}^e \mathbf{F}_{F_l}^v$, where the k and l subscripts indicates the k th and l th relaxation process of the matrix phase (see [29] for isotropic viscoelasticity). In the following, only one relaxation process is considered for either phases for simplicity. The viscous deformation gradients \mathbf{F}_M^v and \mathbf{F}_F^v describe distinct mappings from the reference configuration Ω_0 to the intermediate configurations $\tilde{\Omega}_M$ and $\tilde{\Omega}_F$ corresponding to the matrix and fiber phases. From this, the elastic and viscous right Cauchy-Green deformation and corresponding rate of viscous deformation tensors can be defined for the matrix and fiber phases as,

$$\begin{aligned} \mathbf{C}_M^e &:= \mathbf{F}_M^{eT} \mathbf{F}_M^e, & \mathbf{C}_M^v &:= \mathbf{F}_M^{vT} \mathbf{F}_M^v, & \mathbf{C}_F^e &:= \mathbf{F}_F^{eT} \mathbf{F}_F^e, & \mathbf{C}_F^v &:= \mathbf{F}_F^{vT} \mathbf{F}_F^v, \\ \mathbf{D}_M^v &:= \text{sym} \left[\dot{\mathbf{F}}_M^v \mathbf{F}_M^{v-1} \right] = \frac{1}{2} \mathbf{F}_M^{v-T} \dot{\mathbf{C}}_M^v \mathbf{F}_M^{v-1}, & \mathbf{D}_F^v &:= \text{sym} \left[\dot{\mathbf{F}}_F^v \mathbf{F}_F^{v-1} \right] = \frac{1}{2} \mathbf{F}_F^{v-T} \dot{\mathbf{C}}_F^v \mathbf{F}_F^{v-1}. \end{aligned} \quad (4.6)$$

Substituting the multiplicative split of the deformation gradient for the fiber phase in eq. (4.5) into eq. (4.1) for F_α gives $\lambda_i \mathbf{p}_\alpha = \mathbf{F}_F^e (\mathbf{F}_F^v \mathbf{P}_\alpha)$. The term in the parentheses denotes a mapping of the fiber vector of F_α from the reference to the intermediate configuration by the viscous deformation gradient \mathbf{F}_F^v . The result of this mapping is defined as,

$$\lambda_\alpha^v \tilde{\mathbf{P}}_\alpha := \mathbf{F}_F^v \mathbf{P}_\alpha. \quad (4.7)$$

where the viscous fiber stretch λ_α^v and unit fiber vector $\tilde{\mathbf{P}}_\alpha$ denote the deformation and orientation of the fiber family in the intermediate configuration. From $\tilde{\mathbf{P}}_\alpha$, the following structure tensor is defined in the intermediate configuration [73],

$$\tilde{\mathbf{M}}_\alpha := \tilde{\mathbf{P}}_\alpha \otimes \tilde{\mathbf{P}}_\alpha = \frac{\mathbf{F}_F^v \mathbf{M}_\alpha \mathbf{F}_F^{vT}}{\mathbf{C}_F^v : \mathbf{M}_\alpha}. \quad (4.8)$$

Then, the viscous fiber stretch can be computed from eq. (4.7) as,

$$\lambda_\alpha^v = \sqrt{\mathbf{C}_F^v : \mathbf{M}_\alpha}, \quad (4.9)$$

and the viscous stretch rate of F_α can be determined from (4.6), (4.8), and eq. (4.9) as,

$$\frac{\dot{\lambda}_\alpha^v}{\lambda_\alpha^v} = \mathbf{D}_F^v : \tilde{\mathbf{M}}_\alpha. \quad (4.10)$$

This result is analogous to eq. (4.4) for the total stretch rate of F_α . To complete the kinematics developments, the mapping of $\tilde{\mathbf{P}}_\alpha$ from the intermediate to the spatial

configuration is defined as $\lambda_\alpha^e \mathbf{p}_\alpha := \mathbf{F}_F^e \widetilde{\mathbf{P}}_\alpha$. This allows the elastic component of the fiber stretch to be evaluated as,

$$\lambda_\alpha^e = \sqrt{\mathbf{C}_F^e : \widetilde{\mathbf{M}}_\alpha} = \frac{\lambda_\alpha}{\lambda_\alpha^v}. \quad (4.11)$$

4.2.2 Isotropic Invariants and the Free-Energy Density Function

The constitutive relations for the soft fiber-reinforced composites are developed following the internal state variable thermodynamic framework of [20]. A description of the material anisotropy is incorporated into the constitutive relations using the structure tensor method developed for finite-elasticity by [26, 84], and [79]. To begin, an isotropic function of the form $\mathcal{W}(\mathbf{C}, \mathbf{M}_\alpha, \mathbf{F}_M^v, \mathbf{F}_F^v)$ is postulated for the Helmholtz free energy density of the composite material (see the fundamental works of [9, 10] and [54] on the isotropic representation of anisotropic tensor functions). It is a function of the objective Cauchy-Green deformation tensor, the structure tensors denoting the fiber orientations in Ω_0 , and internal state variables for the viscous relaxation of the matrix and fiber phases. It is assumed that the free energy density can be split additively into an equilibrium component $\mathcal{W}^{\text{eq}}(\mathbf{C}, \mathbf{M}_\alpha)$ responsible for the time-independent stress response of the equilibrium state, and a nonequilibrium component $\mathcal{W}^{\text{neq}}(\mathbf{C}_M^e, \mathbf{C}_F^e, \widetilde{\mathbf{M}}_\alpha)$ responsible for the time-evolving part of the stress response. The decomposition of the stress response into time-independent and time-evolving parts was first proposed by [30] in their kinetic theory of rubber relaxation and since then has been adopted widely to describe the viscoelastic behavior of elastomers and other polymers [55, 53, 74, 5]. In a relaxation experiment $\mathcal{W}^{\text{eq}}(\mathbf{C}, \mathbf{M}_\alpha)$ determines the stress response in the long-time limit.

To model the viscoelastic behavior of both the matrix and fiber phases, the equilibrium and nonequilibrium components of the free-energy density are decomposed further into isotropic and anisotropic components. The equilibrium isotropic component of the free energy density $\mathcal{W}_M^{\text{eq}}(\mathbf{C})$ is formulated as an isotropic function of the three invariants of \mathbf{C} ,

$$I_1 = \mathbf{C} : \mathbf{1}, \quad I_2 = \frac{1}{2} (I_1^2 - \mathbf{C}^2 : \mathbf{1}), \quad I_3 = \det \mathbf{C}, \quad (4.12)$$

while the invariants of \mathbf{C} and \mathbf{M}_α , referred to here as structural invariants, are applied to formulate the equilibrium anisotropic component $\mathcal{W}_F^{\text{eq}}(\mathbf{C}, \mathbf{M}_\alpha)$. For a material with two fiber-families, $N = 2$, these invariants are given by,

$$\begin{aligned} I_4 &= \mathbf{C} : \mathbf{M}_1, \quad I_5 = \mathbf{C}^2 : \mathbf{M}_1, \quad I_6 = \mathbf{C} : \mathbf{M}_2, \quad I_7 = \mathbf{C}^2 : \mathbf{M}_2, \\ I_8 &= \text{tr}(\mathbf{C}\mathbf{M}_1\mathbf{M}_2), \quad I_9 = \mathbf{M}_1 : \mathbf{M}_2, \end{aligned} \quad (4.13)$$

where $\text{tr}(\cdot)$ denotes the trace of the tensor. The nonequilibrium isotropic component of the free-energy density $\mathcal{W}_M^{\text{neq}}(\mathbf{C}_M^e)$, modeling the time-dependent response of the

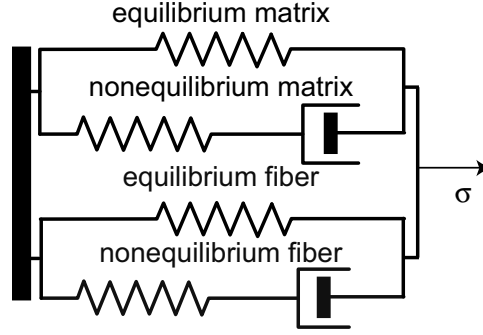


Figure 4.1. Rheological model of viscoelastic behavior of soft fiber-reinforced composite.

matrix, is expressed as an isotropic function of the three invariants of \mathbf{C}_M^e ,

$$I_{M_1}^e = \mathbf{C}_M^e : \mathbf{1}, \quad I_{M_2}^e = \frac{1}{2} \left(I_{M_1}^{e^2} - \mathbf{C}_M^e : \mathbf{1} \right), \quad I_{M_3}^e = \det \mathbf{C}_M^e. \quad (4.14)$$

Lastly, the nonequilibrium component of the free-energy density $\mathcal{W}_F^{\text{neq}} \left(\mathbf{C}_F^e, \widetilde{\mathbf{M}}_\alpha \right)$ is formulated as an isotropic function of the invariants of \mathbf{C}_F^e and $\widetilde{\mathbf{M}}_\alpha$. For a composite material with two fiber-families, these invariants are defined analogously to those in eqs. (4.12)-(4.13) as,

$$\begin{aligned} I_{F_1}^e &= \mathbf{C}_F^e : \mathbf{1}, \quad I_{F_2}^e = \frac{1}{2} \left(I_{F_1}^{e^2} - \mathbf{C}_F^e : \mathbf{1} \right), \quad I_{F_3}^e = \det \mathbf{C}_F^e, \\ I_{F_4}^e &= \mathbf{C}_F^e : \widetilde{\mathbf{M}}_1, \quad I_{F_5}^e = \mathbf{C}_F^e : \widetilde{\mathbf{M}}_1^2, \quad I_{F_6}^e = \mathbf{C}_F^e : \widetilde{\mathbf{M}}_2, \quad I_{F_7}^e = \mathbf{C}_F^e : \widetilde{\mathbf{M}}_2^2, \\ I_{F_8}^e &= \text{tr} \left(\mathbf{C}_F^e \widetilde{\mathbf{M}}_1 \widetilde{\mathbf{M}}_2 \right), \quad I_{F_9}^e = \widetilde{\mathbf{M}}_1 : \widetilde{\mathbf{M}}_2. \end{aligned} \quad (4.15)$$

This formulation for the nonlinear anisotropic viscoelastic behavior of the composite is analogous to the rheological model shown in Fig. 4.1 of two three-parameters standard models arranged in parallel. Separately, the two standard models describe the viscoelastic response of the matrix and fiber phases. The components $\mathcal{W}_M^{\text{eq}}$ and $\mathcal{W}_F^{\text{eq}}$ represent the strain energy of the “equilibrium” springs of the rheological model, while $\mathcal{W}_M^{\text{neq}}$ and $\mathcal{W}_F^{\text{neq}}$ represent the strain energy of the Maxwell elements. The deformation tensors \mathbf{C}_M^e and \mathbf{C}_F^e can be considered loosely as associated with the springs in the Maxwell elements.

The elastic deformation tensor of the matrix and fiber phases can be expressed as, $\mathbf{C}_M^e = \mathbf{F}_M^{\text{v-T}} \mathbf{C} \mathbf{F}_M^{\text{v-1}}$ and $\mathbf{C}_F^e = \mathbf{F}_F^{\text{v-T}} \mathbf{C} \mathbf{F}_F^{\text{v-1}}$. This allows the structural invariants of the elastic deformation tensors to be expressed equivalently in terms of the \mathbf{C} and \mathbf{C}_F^v and \mathbf{C}_M^v . For example, the invariants of \mathbf{C}_F^v in eqs. (4.14)-(4.15) can be written also

as,

$$\begin{aligned}
I_{F_1}^e &= \mathbf{C} : \mathbf{C}_F^{\mathbf{v}^{-1}}, \quad I_{F_2}^e = \frac{1}{2} \left(I_{F_1}^{e^2} - \mathbf{C} \mathbf{C}_F^{\mathbf{v}^{-1}} : \mathbf{C}_F^{\mathbf{v}^{-1}} \mathbf{C} \right), \quad I_{F_3}^e = \det \left[\mathbf{C} \mathbf{C}_F^{\mathbf{v}^{-1}} \right], \\
I_{F_4}^e &= \frac{\mathbf{C} : \mathbf{M}_1}{\mathbf{C}_F^{\mathbf{v}} : \mathbf{M}_1}, \quad I_{F_5}^e = \frac{\mathbf{C} \mathbf{C}_F^{\mathbf{v}^{-1}} \mathbf{C} : \mathbf{M}_1}{\mathbf{C}_F^{\mathbf{v}} : \mathbf{M}_1}, \quad I_{F_6}^e = \frac{\mathbf{C} : \mathbf{M}_2}{\mathbf{C}_F^{\mathbf{v}} : \mathbf{M}_2}, \quad I_{F_7}^e = \frac{\mathbf{C} \mathbf{C}_F^{\mathbf{v}^{-1}} \mathbf{C} : \mathbf{M}_2}{\mathbf{C}_F^{\mathbf{v}} : \mathbf{M}_2}, \\
I_{F_8}^e &= \frac{\mathbf{M}_1 \mathbf{C} : \mathbf{C}_F^{\mathbf{v}} \mathbf{M}_2}{(\mathbf{C}_F^{\mathbf{v}} : \mathbf{M}_1) (\mathbf{C}_F^{\mathbf{v}} : \mathbf{M}_2)}, \quad I_{F_9}^e = \frac{\mathbf{C}_F^{\mathbf{v}} \mathbf{M}_1 : \mathbf{M}_2 \mathbf{C}_F^{\mathbf{v}}}{(\mathbf{C}_F^{\mathbf{v}} : \mathbf{M}_1) (\mathbf{C}_F^{\mathbf{v}} : \mathbf{M}_2)}.
\end{aligned} \tag{4.16}$$

Then, $\mathbf{C}_F^{\mathbf{v}}$ and $\mathbf{C}_M^{\mathbf{v}}$ can be considered the primitive internal state variable of the formulation which allows the stress relations to be independent of the rotational components of $\mathbf{F}_F^{\mathbf{v}}$ and $\mathbf{F}_M^{\mathbf{v}}$ [73]. To complete the formulation, one only needs to specify evolution equations for $\mathbf{C}_F^{\mathbf{v}}$ and $\mathbf{C}_M^{\mathbf{v}}$ and not for the rotational components of the viscous deformation gradients. This leaves the description of the material anisotropy in the intermediate configuration (i.e, $\widetilde{\mathbf{M}}_\alpha$) undetermined.

The general formulation for the free energy density proposed thus far can be expressed for a composite with two fiber-families as,

$$\begin{aligned}
\mathcal{W}(\mathbf{C}, \mathbf{C}_M^{\mathbf{v}}, \mathbf{C}_F^{\mathbf{v}}) &= \mathcal{W}_M^{\text{eq}}(I_1, I_2, I_3) + \sum_{\alpha} \mathcal{W}_{F_\alpha}^{\text{eq}}(I_4, I_5, I_6, I_7, I_8, I_9) \\
&+ \mathcal{W}_M^{\text{neq}}(I_{M_1}^e, I_{M_2}^e, I_{M_3}^e) + \sum_{\alpha} \mathcal{W}_{F_\alpha}^{\text{neq}}(I_{F_4}^e, I_{F_5}^e, I_{F_6}^e, I_{F_7}^e, I_{F_8}^e, I_{F_9}^e). \quad (4.17)
\end{aligned}$$

Equation (4.17) is an irreducible representation of the isotropic invariants of the deformation, structural, and internal variables needed to specify the viscoelastic stress state of the composite. However, it involves 21 invariants and is impractical to apply for most problems of interests. The remainder of the constitutive developments will present two models that are simplifications of the general framework. The first model is developed for a composite material with arbitrary N fiber-families where the fiber reinforcing model is dependent only on the fiber stretches through $\mathbf{C} : \mathbf{M}_\alpha$ and $\mathbf{C}^e : \widetilde{\mathbf{M}}_\alpha$. The second model admits a generalization for the case of two fiber families to allow for additional dependence on I_5 and I_7 . These structural invariants are also related to the fiber stretch, but they introduce additional effects of fiber reinforcement in shear as demonstrated for finite-elasticity by [59].

4.2.3 Constitutive Model for N fiber-families

The following simplified form of the free energy density function is proposed for a composite material described by N fiber-families embedded in an isotropic matrix,

$$\mathcal{W} = \mathcal{W}_M^{\text{eq}}(I_1, I_2, I_3) + \mathcal{W}_M^{\text{neq}}(I_{M_1}^e, I_{M_2}^e, I_{M_3}^e) + \sum_{\alpha=1}^N \left(\mathcal{W}_{F_\alpha}^{\text{eq}}(I_{\alpha+3}) + \mathcal{W}_{F_\alpha}^{\text{neq}}(I_{F_{\alpha+3}}^e) \right), \quad (4.18)$$

where $I_{\alpha+3} := \mathbf{C} : \mathbf{M}_\alpha = \lambda_\alpha^2$ and $I_{F_{\alpha+3}}^e := \mathbf{C}_F^e : \widetilde{\mathbf{M}}_\alpha = \lambda_\alpha^{e2}$. Note that this numbering scheme for the structural invariants does not correspond to those of eq. (4.15) which applies for a two fiber-family system. The fiber families are represented in eq. (4.18) as rod-like elements that interact with each other and with the matrix only through the kinematic constraint imposed by the deformation gradient. The function $\mathcal{W}_{F_\alpha}(I_{\alpha+3}, I_{F_{\alpha+3}}^e) = \mathcal{W}_{F_\alpha}^{\text{eq}}(I_{\alpha+3}) + \mathcal{W}_{F_\alpha}^{\text{neq}}(I_{F_{\alpha+3}}^e)$ can be considered the free energy density for the stretch of a rod representing the fiber family F_α . It is split additively into equilibrium and nonequilibrium components to model the time-dependent behavior of the fiber reinforcements. The free energy density of the fiber phase of the continuum body is equated to the sum of the free energy density of the N fiber-families. This is a common homogenization scheme that has been applied successfully to model the constitutive behavior of many engineering materials, such as the finite-elasticity of single crystals [42], polymers [4], and fiber-reinforced tissues [50].

Applying the free energy density function in eq. (4.18) to the Clausius-Duhem form of the second law of thermodynamics gives the isothermal dissipation inequality,

$$\left(\mathbf{S} - 2 \frac{\partial \mathcal{W}}{\partial \mathbf{C}} \right) : \frac{1}{2} \dot{\mathbf{C}} - 2 \frac{\partial \mathcal{W}}{\partial \mathbf{C}_M^v} : \frac{1}{2} \dot{\mathbf{C}}_M^v - 2 \frac{\partial \mathcal{W}}{\partial \mathbf{C}_F^v} : \frac{1}{2} \dot{\mathbf{C}}_F^v \geq 0, \quad (4.19)$$

where \mathbf{S} is the second Piola-Kirchhoff stress. Requiring that the dissipation vanishes in the equilibrium state, defined by $\dot{\mathbf{C}}_M^v = \dot{\mathbf{C}}_F^v = \mathbf{0}$, gives the usual expression for the stress relation $\mathbf{S} = 2 \frac{\partial \mathcal{W}}{\partial \mathbf{C}}$ which for \mathcal{W} in eq. (4.18), can be evaluated as,

$$\begin{aligned} \mathbf{S} &= \underbrace{2 \frac{\partial \mathcal{W}_M^{\text{eq}}}{\partial I_1} \mathbf{1} + 2 \frac{\partial \mathcal{W}_M^{\text{eq}}}{\partial I_2} (I_1 \mathbf{1} - \mathbf{C}) + 2 \frac{\partial \mathcal{W}_M^{\text{eq}}}{\partial I_3} I_3 \mathbf{C}^{-1}}_{\mathbf{S}_M^{\text{eq}}} \\ &+ \underbrace{2 \frac{\partial \mathcal{W}_M^{\text{neq}}}{\partial I_{M_1}^e} \mathbf{C}_M^{v-1} + 2 \frac{\partial \mathcal{W}_M^{\text{neq}}}{\partial I_{M_2}} \left(I_{M_1}^e \mathbf{C}_M^{v-1} - \mathbf{C}_M^{v-1} \mathbf{C} \mathbf{C}_M^{v-1} \right) + 2 \frac{\partial \mathcal{W}_M^{\text{neq}}}{\partial I_{M_3}^e} I_{M_3}^e \mathbf{C}^{-1}}_{\mathbf{S}_M^{\text{neq}}} \\ &+ \underbrace{\sum_{\alpha=1}^N 2 \frac{\partial \mathcal{W}_F^{\text{eq}}}{\partial I_{\alpha+3}} \mathbf{M}_\alpha}_{\mathbf{S}_F^{\text{eq}}} + \underbrace{\sum_{\alpha=1}^N 2 \frac{\partial \mathcal{W}_F^{\text{neq}}}{\partial I_{F_{\alpha+3}}^e} \frac{\mathbf{M}_\alpha}{\mathbf{C}_F^v : \mathbf{M}_\alpha}}_{\mathbf{S}_F^{\text{neq}}}. \end{aligned} \quad (4.20)$$

A Piola transformation of eq. (4.20) with \mathbf{F} gives an expression for the Cauchy stress

in the spatial configuration as,

$$\begin{aligned}
\boldsymbol{\sigma} = & \underbrace{\frac{2}{\sqrt{I_3}} \frac{\partial \mathcal{W}_M^{\text{eq}}}{\partial I_1} \mathbf{b} + \frac{2}{\sqrt{I_3}} \frac{\partial \mathcal{W}_M^{\text{eq}}}{\partial I_2} (I_1 \mathbf{b} - \mathbf{b}^2) + \frac{2}{\sqrt{I_3}} \frac{\partial \mathcal{W}_M^{\text{eq}}}{\partial I_3} I_3 \mathbf{1}}_{\boldsymbol{\sigma}_M^{\text{eq}}} \\
& + \underbrace{\frac{2}{\sqrt{I_3}} \frac{\partial \mathcal{W}_M^{\text{neq}}}{\partial I_{M_1}^e} \mathbf{b}_M^e + \frac{2}{\sqrt{I_3}} \frac{\partial \mathcal{W}_M^{\text{neq}}}{\partial I_{M_2}^e} (I_{M_1}^e \mathbf{b}_M^e - \mathbf{b}_M^{e^2}) + \frac{2}{\sqrt{I_3}} \frac{\partial \mathcal{W}_M^{\text{neq}}}{\partial I_{M_3}^e} I_{M_3}^e \mathbf{1}}_{\boldsymbol{\sigma}_M^{\text{neq}}} \\
& + \underbrace{\sum_{\alpha=1}^N \frac{2}{\sqrt{I_3}} \frac{\partial \mathcal{W}_F^{\text{eq}}}{\partial I_{\alpha+3}} I_{\alpha+3} \mathbf{m}_\alpha}_{\boldsymbol{\sigma}_F^{\text{eq}}} + \underbrace{\sum_{\alpha=1}^N \frac{2}{\sqrt{I_3}} \frac{\partial \mathcal{W}_F^{\text{neq}}}{\partial I_{F_{\alpha+3}}^e} I_{F_{\alpha+3}}^e \mathbf{m}_\alpha}_{\boldsymbol{\sigma}_F^{\text{neq}}},
\end{aligned} \tag{4.21}$$

where $\mathbf{b} = \mathbf{F}\mathbf{F}^T$, $\mathbf{b}_M^e = \mathbf{F}_M^e \mathbf{F}_M^{eT}$, and $\mathbf{b}_F^e = \mathbf{F}_F^e \mathbf{F}_F^{eT}$. The anisotropic component of the stress response in (4.21) can be written as, $\boldsymbol{\sigma}_F = \frac{1}{\sqrt{I_3}} \sum_{\alpha=1}^N \tau_{F_\alpha} \mathbf{m}_\alpha$, where τ_{F_α} is the fiber stress of F_α . Like the fiber free energy density, it is also additively decomposed into equilibrium and nonequilibrium components.

Substituting eq. (4.20) into eq. (4.19) gives the following expression for the reduced dissipation inequality,

$$\underbrace{-2 \frac{\partial \mathcal{W}_M^{\text{neq}}}{\partial \mathbf{C}_M^v}}_{\mathbf{T}_M} : \frac{1}{2} \dot{\mathbf{C}}_M^v - \underbrace{2 \frac{\partial \mathcal{W}_F^{\text{neq}}}{\partial \mathbf{C}_F^v}}_{\mathbf{T}_F} : \frac{1}{2} \dot{\mathbf{C}}_F^v \geq 0, \tag{4.22}$$

where \mathbf{T}_M and \mathbf{T}_F are the stresses driving the viscous relaxation of the matrix and fiber phases. The two terms in eq. (4.22) represent the viscous dissipation exhibited by the matrix and fiber phases. Both are required to be positive, and eq. (4.22) is split into two separate criteria $\mathbf{T}_M : \frac{1}{2} \dot{\mathbf{C}}_M^v \geq 0$ and $\mathbf{T}_F : \frac{1}{2} \dot{\mathbf{C}}_F^v \geq 0$. It is assumed that the viscous relaxation of the two phases are governed by different physical processes and thus, occur independently of each other. This assumption allows for separate evolution equations to be developed for \mathbf{C}_M^v and \mathbf{C}_F^v .

The isotropic flow stress of the matrix can be evaluated for the free energy density in eq. (4.18) to give,

$$\mathbf{T}_M = \mathbf{C}_M^{v-1} \left(2 \frac{\partial \mathcal{W}_M^{\text{neq}}}{\partial I_{M_1}^e} \mathbf{C} + 2 \frac{\partial \mathcal{W}_M^{\text{neq}}}{\partial I_{M_2}^e} (I_{M_1}^e \mathbf{C} - \mathbf{C} \mathbf{C}_M^{v-1} \mathbf{C}) + 2 \frac{\partial \mathcal{W}_M^{\text{neq}}}{\partial I_{M_3}^e} I_{M_3}^e \mathbf{C}_M^v \right) \mathbf{C}_M^{v-1}, \tag{4.23}$$

To satisfy the positive dissipation criterion for the matrix phase, the following evolution equation is proposed for \mathbf{C}_M^v ,

$$\frac{1}{2} \dot{\mathbf{C}}_M^v = \mathbb{V}_M^{-1} : \mathbf{T}_M. \tag{4.24}$$

The parameter \mathbb{V}_M^{-1} is the inverse of a positive-definite, fourth-order, isotropic viscosity tensor given by,

$$\mathbb{V}_M^{-1} := \frac{1}{2\eta_{M_S}} \left(\mathbf{C}_M^v \odot \mathbf{C}_M^v - \frac{1}{3} \mathbf{C}_M^v \otimes \mathbf{C}_M^v \right) + \frac{1}{9\eta_{M_B}} \mathbf{C}_M^v \otimes \mathbf{C}_M^v, \quad (4.25)$$

where $(\mathbf{C}_M^v \odot \mathbf{C}_M^v)_{IJKL} = \frac{1}{2} (C_{M_{IK}}^v C_{M_{JL}}^v + C_{M_{IL}}^v C_{M_{JK}}^v)$, and η_{M_B} and η_{M_S} are respectively the bulk and shear viscosities of the matrix material. The formulation does not place any restriction on η_{M_B} and η_{M_S} except that they be positive. Thus, they can depend in general on the isotropic invariants of \mathbf{C}_M^v and/or \mathbf{T}_M (see for example [5] and [63]). It can be shown (see Section 4.5) that the spatial representation of eq. (4.24) is identical to the evolution equation proposed by [74] in their theory for isotropic nonlinear viscoelasticity. Thus, the isotropic part of the model presented here is identical to their isotropic viscoelasticity model.

To develop an evolution equation for \mathbf{C}_F^v , the anisotropic flow stress \mathbf{T}_F for the fiber phase is evaluated for the free energy density in eq. (4.18) as,

$$\mathbf{T}_F = \sum_{\alpha=1}^N 2 \frac{\partial \mathcal{W}_{F_\alpha}^{\text{neq}}}{\partial I_{F_{\alpha+3}}^e} I_{F_{\alpha+3}}^e \frac{\mathbf{M}_\alpha}{\mathbf{C}_F^v : \mathbf{M}_\alpha}. \quad (4.26)$$

Substituting eq. (4.26) into the reduced dissipation inequality for the fiber phase and applying the relation for the viscous stretch rate calculated from eq. (4.9) and fiber stress obtained from eq. (4.21) gives,

$$\sum_{\alpha=1}^N \tau_{F_\alpha}^{\text{neq}} \left(\frac{\dot{\lambda}_\alpha^v}{\lambda_\alpha^v} \right) \geq 0. \quad (4.27)$$

where $\tau_{F_\alpha}^{\text{neq}} = 2 \frac{\partial \mathcal{W}_{F_\alpha}^{\text{neq}}}{\partial I_{F_{\alpha+3}}^e} I_{F_{\alpha+3}}^e$ is the nonequilibrium component of the fiber stress. The expression on the left hand side of eq. (4.27) is the viscous dissipation of the fiber network and is required to remain non-negative. It is given by the sum of the viscous dissipation exhibited by the N fiber-families. From physical arguments, these must also be non-negative:

$$\tau_{F_\alpha}^{\text{neq}} \left(\frac{\dot{\lambda}_\alpha^v}{\lambda_\alpha^v} \right) \geq 0, \quad \text{for all } \alpha = 1 \dots N. \quad (4.28)$$

According to eq. (4.28), the nonequilibrium fiber stress $\tau_{F_\alpha}^{\text{neq}}$ is the thermodynamic stress driving the viscous relaxation of F_α . The following simple flow rule is proposed for the viscous stretch of F_α to satisfy the positive dissipation criterion,

$$\frac{\dot{\lambda}_\alpha^v}{\lambda_\alpha^v} = \frac{1}{\eta_{F_\alpha}} \tau_{F_\alpha}^{\text{neq}} (\lambda_{F_\alpha}^e), \quad (4.29)$$

where η_{F_α} is a positive scalar quantity representing the characteristic viscosity of F_α that in general can depend on $\tau_{F_\alpha}^{\text{neq}}$ and the fiber stretches λ_α and λ_α^v . Substituting

the flow rule in eq. (4.29) into eq. (4.26) for \mathbf{T}_F gives the following homogenized anisotropic flow rule for the fiber phase,

$$\mathbf{T}_F = \mathbb{V}_F : \frac{1}{2} \dot{\mathbf{C}}_F^v, \quad \mathbb{V}_F = \sum_{\alpha=1} \eta_{F\alpha} \frac{\mathbf{M}_\alpha}{\mathbf{C}_F^v : \mathbf{M}_\alpha} \otimes \frac{\mathbf{M}_\alpha}{\mathbf{C}_F^v : \mathbf{M}_\alpha}, \quad (4.30)$$

where \mathbb{V}_F is the effective anisotropic viscosity tensor of the fiber phase that is directly related to the viscosity of the individual fiber families and the fiber arrangement. For a planar fiber arrangement with more than three fiber families and for a three dimensional fiber arrangement with more than six fiber families, it is more efficient to solve eq. (4.30) than eq. (4.29) for the viscous deformation of the fiber phase. To summarize, the stress relation in eq. (4.21) and the evolution equations (4.24) and (4.29) (or alternatively eq. (4.30)) form a complete constitutive model for a fiber-reinforced composite material with N fiber-families. The numerical implementation of the model into a finite element framework is developed in Section 4.3.

4.2.4 Constitutive Model for Two Fiber-Families

This section presents a generalization of the nonlinear viscoelasticity framework developed in Sec. 4.2.3 for a composite with two fiber-families. The developments here allow the free energy density to depend on higher order structural invariants I_5 and I_7 defined in eqs. (4.13) and $I_{F_5}^e$ and $I_{F_7}^e$ defined in (4.15). As a short hand, the notation $I_{2\alpha+2}$ for $\alpha = 1, 2$ is used to denote the invariants I_4 and I_6 while $I_{2\alpha+3}$ is applied for the higher order invariants I_5 and I_7 . Similarly, $I_{F_{2\alpha+2}}^e$ and $I_{F_{2\alpha+3}}^e$ are used for $I_{F_4}^e$ and $I_{F_6}^e$, and $I_{F_5}^e$ and $I_{F_7}^e$. The following simplified form of the free energy is proposed for the composite material with two fiber-families,

$$\begin{aligned} \mathcal{W} = & \mathcal{W}_M^{\text{eq}}(I_1, I_2, I_3) + \mathcal{W}_M^{\text{neq}}(I_{M_1}^e, I_{M_2}^e, I_{M_3}^e) \\ & + \sum_{\alpha=1}^2 \mathcal{W}_{F_\alpha}^{\text{eq}}(I_{2\alpha+2}, I_{2\alpha+3}) + \sum_{\alpha=1}^2 \mathcal{W}_{F_\alpha}^{\text{neq}}(I_{F_{2\alpha+2}}^e, I_{F_{2\alpha+3}}^e). \end{aligned} \quad (4.31)$$

The same formulation of \mathcal{W}_M as used previously in Sec. 4.2.3 is applied to model the isotropic time-dependent behavior of the matrix. Thus, only developments pertaining the anisotropic part of the model are presented in this section. The stress response is computed using the relation $\mathbf{S} = 2 \frac{\partial \mathcal{W}}{\partial \mathbf{C}}$, which yields the following for the anisotropic component of the second Piola-Kirchhoff stress tensor,

$$\begin{aligned} \mathbf{S}_F = & \underbrace{\sum_{\alpha=1}^2 \left(2 \frac{\partial \mathcal{W}_{F_\alpha}^{\text{eq}}}{\partial I_{2\alpha+2}} \mathbf{M}_\alpha + \frac{\partial \mathcal{W}_{F_\alpha}^{\text{eq}}}{\partial I_{2\alpha+3}} (\mathbf{C} \mathbf{M}_\alpha + \mathbf{M}_\alpha \mathbf{C}) \right)}_{\mathbf{S}_F^{\text{eq}}} \\ & + \underbrace{\sum_{\alpha=1}^2 \left(2 \frac{\partial \mathcal{W}_{F_\alpha}^{\text{neq}}}{\partial I_{F_{2\alpha+2}}^e} \frac{\mathbf{M}_\alpha}{\mathbf{C}_F^v : \mathbf{M}_\alpha} + 2 \frac{\partial \mathcal{W}_{F_\alpha}^{\text{neq}}}{\partial I_{F_{2\alpha+3}}^e} \frac{\mathbf{C}_F^{v^{-1}} \mathbf{C} \mathbf{M}_\alpha + \mathbf{M}_\alpha \mathbf{C} \mathbf{C}_F^{v^{-1}}}{\mathbf{C}_F^v : \mathbf{M}_\alpha} \right)}_{\mathbf{S}_F^{\text{neq}}}. \end{aligned} \quad (4.32)$$

The isotropic component of the stress response \mathbf{S}_M is given in eq. (4.20). The anisotropic stress component can be expressed in the spatial configuration by applying the Piola transformation to give,

$$\begin{aligned} \boldsymbol{\sigma}_F = & \underbrace{\sum_{\alpha=1}^2 \left(\frac{2}{\sqrt{I_3}} \frac{\partial \mathcal{W}_{F_\alpha}^{\text{eq}}}{\partial I_{2\alpha+2}} I_{2\alpha+2} \mathbf{m}_\alpha + \frac{2}{\sqrt{I_3}} \frac{\partial \mathcal{W}_{F_\alpha}^{\text{eq}}}{\partial I_{2\alpha+3}} I_{2\alpha+3} (\mathbf{b} \mathbf{m}_\alpha + \mathbf{m}_\alpha \mathbf{b}) \right)}_{\boldsymbol{\sigma}_F^{\text{eq}}} \\ & + \underbrace{\sum_{\alpha=1}^2 \left(\frac{2}{\sqrt{I_3}} \frac{\partial \mathcal{W}_{F_\alpha}^{\text{neq}}}{\partial I_{F_{2\alpha+2}}^e} I_{F_{2\alpha+2}}^e \mathbf{m}_\alpha + \frac{2}{\sqrt{I_3}} \frac{\partial \mathcal{W}_{F_\alpha}^{\text{neq}}}{\partial I_{F_{2\alpha+3}}^e} I_{F_{2\alpha+3}}^e (\mathbf{b}_F^e \mathbf{m}_\alpha + \mathbf{m}_\alpha \mathbf{b}_F^e) \right)}_{\boldsymbol{\sigma}_F^{\text{neq}}}. \end{aligned} \quad (4.33)$$

The reduced dissipation inequality for the fiber phase is computed by applying the free energy density in eq. (4.31) to eq. (4.22) as,

$$\begin{aligned} \left[\left(\sum_{\alpha=1}^2 2 \frac{\partial \mathcal{W}_{F_\alpha}^{\text{neq}}}{\partial I_{F_{2\alpha+2}}^e} I_{F_{2\alpha+2}}^e + 2 \frac{\partial \mathcal{W}_{F_\alpha}^{\text{neq}}}{\partial I_{F_{2\alpha+3}}^e} I_{F_{2\alpha+3}}^e \right) \frac{\mathbf{M}_\alpha}{\mathbf{C}_F^v : \mathbf{M}_\alpha} \right. \\ \left. + \sum_{\alpha=1}^2 2 \frac{\partial \mathcal{W}_{F_\alpha}^{\text{neq}}}{\partial I_{F_{2\alpha+3}}^e} \frac{\mathbf{C}_F^{v-1} \mathbf{C} \mathbf{M}_\alpha \mathbf{C} \mathbf{C}_F^{v-1}}{\mathbf{C}_F^v : \mathbf{M}_\alpha} \right] : \frac{1}{2} \dot{\mathbf{C}}_F^v \geq 0, \end{aligned} \quad (4.34)$$

Where the term in the bracket is the flow stress \mathbf{T}_F of the fiber phase. It is desired to develop a flow rule for λ_α^v that is similar to eq. (4.29) for the simpler N fiber-families model. However, an expression for the thermodynamic stress driving the evolution of λ_α^v is not apparent from the reduced dissipation inequality in eq. (4.34) because of the coupling between the normal and shear response produced by the higher order structural invariants $I_{2\alpha+3}^e$. Here, inspiration is taken from the formulation in Sec. 4.2.3 to develop a relationship between the flow stress \mathbf{T}_F and nonequilibrium anisotropic stress component $\boldsymbol{\sigma}_F^{\text{neq}}$. With some algebraic manipulations, it can be shown (see Section 4.6) that for the orthotropic case, $\mathbf{P}_1 \cdot \mathbf{P}_2 = 0$,

$$\sqrt{I_3} \boldsymbol{\sigma}_F^{\text{neq}} : I_{2\alpha+2} \text{sym} [\mathbf{m}_\alpha \mathbf{b}^{-1}] = \mathbf{T} : \text{sym} [\mathbf{M}_\alpha \mathbf{C}_F^v], \quad (4.35)$$

where $\sqrt{I_3} \boldsymbol{\sigma}_F^{\text{neq}} : I_{2\alpha+2} \text{sym} [\mathbf{m}_\alpha \mathbf{b}^{-1}] = \tau_{F_\alpha}^{\text{neq}}$ is the fiber stress computed by projecting the nonequilibrium stress of fiber phase onto the fiber orientation vectors. The fiber stress can be evaluated for $\boldsymbol{\sigma}_F$ in eq. (4.33) as,

$$\begin{aligned} \tau_{F_\alpha}^{\text{neq}} = & 2 \frac{\partial \mathcal{W}_{F_\alpha}^{\text{neq}}}{\partial I_{F_{2\alpha+2}}^e} I_{F_{2\alpha+2}}^e + 2 \frac{\partial \mathcal{W}_{F_\alpha}^{\text{neq}}}{\partial I_{F_{2\alpha+3}}^e} I_{F_{2\alpha+3}}^e \\ & + \sum_{\beta}^2 \frac{\partial \mathcal{W}_{F_\beta}^{\text{neq}}}{\partial I_{F_{2\beta+3}}^e} \left(\frac{\mathbf{C}_F^{v-1} \mathbf{C} \mathbf{M}_\beta : \mathbf{M}_\alpha \mathbf{C}}{\mathbf{C}_F^v : \mathbf{M}_\beta} + \frac{\mathbf{M}_\beta \mathbf{C} \mathbf{C}_F^{v-1} : \mathbf{C} \mathbf{M}_\alpha}{\mathbf{C}_F^v : \mathbf{M}_\beta} \right). \end{aligned} \quad (4.36)$$

Then the same fiber-level flow rule in eq. (4.29) can be applied here for the orthotropic case:

$$\frac{\dot{\lambda}_\alpha^v}{\lambda_\alpha^v} = \frac{1}{\eta_{F_\alpha}} \tau_{F_\alpha}^{\text{neq}}. \quad (4.37)$$

where η_{F_α} is in general a scalar function denoting the characteristic viscosity of F_α . The anisotropic component of the stress response in eq. (4.32) requires a solution for \mathbf{C}_F^v . To complete the constitutive formulation, the following relation for \mathbf{C}_F^v and the viscous fiber stretch is proposed for the orthotropic case,

$$\frac{1}{2}\dot{\mathbf{C}}_F^v = \sum_{\alpha=1}^2 \frac{\dot{\lambda}_\alpha^v}{\lambda_\alpha^v} \text{sym} [\mathbf{M}_\alpha \mathbf{C}_F^v]. \quad (4.38)$$

This relation is consistent with the kinematic assumptions made in Sec. 4.2.1 regarding the deformation of the fiber families. Specifically, it can be shown from eq. (4.38) that $\dot{\mathbf{C}}_F^v : \mathbf{M}_\alpha = 2\lambda_\alpha^v \dot{\lambda}_\alpha^v$ for $\mathbf{P}_1 \cdot \mathbf{P}_2 = 0$ which is consistent with the definition of the viscous stretch in eq. (4.9).

An evolution equation for \mathbf{C}_F^v of the fiber phase can be obtained by combining eqs. (4.35), (4.37), and (4.38) to give,

$$\frac{1}{2}\dot{\mathbf{C}}_F^v = \mathbb{V}_F^{-1} : \mathbf{T}_F, \quad \mathbb{V}_F^{-1} = \sum_{\alpha=1}^2 \frac{1}{4\eta_{F_\alpha}} (\mathbf{M}_\alpha \mathbf{C}_F^v + \mathbf{C}_F^v \mathbf{M}_\alpha) \otimes (\mathbf{M}_\alpha \mathbf{C}_F^v + \mathbf{C}_F^v \mathbf{M}_\alpha), \quad (4.39)$$

where \mathbb{V}_F is the anisotropic viscosity tensor that is related directly to the fiber viscosities η_{F_α} and the fiber arrangement. The inverse viscosity tensor in eq. (4.39) possesses both major and minor symmetry. The latter is a consequence of the symmetric property of \mathbf{T}_F and \mathbf{C}_F^v , while the former is a direct consequence of choosing the relation in eq. (4.39) for $\mathbf{C}_{F_\alpha}^v$. Finally, eq. (4.39) is substituted into eq. (4.34) to test for the satisfaction of the positive dissipation criteria. The resulting expression for the viscous dissipation is a quadratic form,

$$\sum_{\alpha=1}^2 \frac{1}{\eta_{F_\alpha}} (\mathbf{T}_F : \text{sym} [\mathbf{M}_\alpha \mathbf{C}_F^v])^2 \geq 0, \quad \text{for } \eta_{F_\alpha} \geq 0, \quad (4.40)$$

that is always positive for $\eta_{F_\alpha} \geq 0$.

The model developed here reduces to the simpler model in Sec. 4.2.3 for two orthogonal fiber families. Absent the dependence of the free-energy density on I_5 , I_7 , $I_{F_5}^e$ and $I_{F_7}^e$, the anisotropic component of the stress response in eq. (4.32) reduces to that in eq. (4.20), and the relation $\dot{\mathbf{C}}_F^v : \mathbf{M}_\alpha$, evaluated from eq. (4.38), reduces to the evolution eq. (4.29) for λ_α^v . A numerical implementation of the model for a finite element framework is developed in Section 4.3.

The significance of the driving stress τ_{F_α} in eq. (4.35) as the fiber stress and the kinematic relation in eq. (4.38) are valid only for $\mathbf{P}_1 \cdot \mathbf{P}_2 = 0$. However, the same formulation can be applied for the case of two non-orthogonal fiber families by defining orthogonal direction vectors that are bisectors of the two non-orthogonal fiber vectors (e.g., $\hat{\mathbf{P}}_1 = \frac{\mathbf{P}_1 + \mathbf{P}_2}{\|\mathbf{P}_1 + \mathbf{P}_2\|}$ and $\hat{\mathbf{P}}_2 = \frac{\mathbf{P}_1 - \mathbf{P}_2}{\|\mathbf{P}_1 - \mathbf{P}_2\|}$). Then the same procedure can be applied to calculate the stresses and stretches of the fiber phase projected onto the two orthogonal directions $\hat{\mathbf{P}}_1$ and $\hat{\mathbf{P}}_2$.

Table 4.1. Integration algorithm for $\lambda_{\alpha_{n+1}}^v$ for N fiber-families model.

Residual for $k + 1$ iteration:	$r_\alpha^{k+1} = \lambda_\alpha^{v^{k+1}} - \frac{\Delta t}{\eta_{F_\alpha}^{k+1}} \tau_{F_\alpha}^{\text{neq}^k} \lambda_\alpha^{v^{k+1}} - \lambda_{\alpha_n}^v = 0,$ $\tau_{F_\alpha}^{\text{neq}} = 2 \frac{\partial \mathcal{W}_F^{\text{neq}}}{\partial I_{F_{\alpha+3}}^e} I_{F_{\alpha+3}}^e,$
Linearize about $\lambda_{F_{\alpha_{n+1}}}^{v^k}$:	$r_\alpha^{k+1} \approx r_\alpha^k \left(\lambda_{F_\alpha}^v \right) + \underbrace{\frac{\partial r_\alpha}{\partial \lambda_\alpha^v}}_{k_\alpha} \Big _{\lambda_\alpha^{v^k}} \Delta \lambda_i^v = 0,$
Consistent tangent:	$k_\alpha = 1 - \frac{\Delta t}{\eta_{F_\alpha}} \left(\left(1 - \frac{1}{\eta_{F_\alpha}} \frac{\partial \eta_{F_\alpha}}{\partial \lambda_\alpha^v} \lambda_\alpha^v \right) \tau_{F_\alpha}^{\text{neq}} - 2 \frac{\partial \tau_{F_\alpha}^{\text{neq}}}{\partial I_{F_{\alpha+3}}^e} I_{F_{\alpha+3}}^e \right),$
Solve for the increment:	$\Delta \lambda_\alpha^v = - \frac{r_\alpha}{k_\alpha} \Big _{\lambda_\alpha^{v^k}},$
Update solution:	$\lambda_\alpha^{v^{k+1}} = \lambda_\alpha^{v^k} + \Delta \lambda_\alpha^v$
Repeat until:	$r_\alpha^{k+1} < c_{\text{tol}}.$
Increment of \mathbf{C}_F^v :	$\Delta \mathbf{C}_F^v : \mathbf{M}_\alpha = \frac{g_\alpha}{k_\alpha \lambda_\alpha^e} \Delta \mathbf{C} : \mathbf{M}_\alpha$
Algorithmic moduli:	$g_\alpha = - \frac{\Delta t}{\eta_{F_\alpha}} \left(\frac{1}{\eta_{F_\alpha}} \frac{\partial \eta_{F_\alpha}}{\partial \lambda_\alpha^v} \lambda_\alpha^v \tau_{F_\alpha}^{\text{neq}} - 2 \frac{\partial \tau_{F_\alpha}^{\text{neq}}}{\partial I_{F_{\alpha+3}}^e} I_{F_{\alpha+3}}^e \right) \frac{\lambda_\alpha^v}{\lambda_\alpha}$ $\mathbf{C}_F^{\text{neq}} = \sum_{\alpha=1}^N \left(4 \frac{\partial^2 \mathcal{W}_{F_\alpha}^{\text{neq}}}{\partial I_{F_{\alpha+3}}^{e^2}} - 4 \left(\frac{\partial^2 \mathcal{W}_{F_\alpha}^{\text{neq}}}{\partial I_{F_{\alpha+3}}^{e^2}} I_{F_{\alpha+3}}^e + \frac{\partial \mathcal{W}_{F_\alpha}^{\text{neq}}}{\partial I_{F_{\alpha+3}}^e} \right) \frac{g_\alpha}{k_\alpha \sqrt{I_{F_{\alpha+3}}^e}} \right) \frac{\mathbf{M}_\alpha}{\mathbf{C}_F^v : \mathbf{M}_\alpha} \otimes \frac{\mathbf{M}_\alpha}{\mathbf{C}_F^v : \mathbf{M}_\alpha}.$

4.3 Numerical Implementation

The constitutive relations for the two models presented in Secs. 4.2.3 and 4.2.4 require the integration of the isotropic evolution equation for \mathbf{C}_M^v of the matrix and the anisotropic evolution equation for \mathbf{C}_F^v of the fiber phase. An efficient numerical integration algorithm has been developed by [74] for the spatial representation of the isotropic evolution equation (4.24). Their work also provides a method for calculating the consistent tangent for the isotropic component of the stress response. Therefore, this section will focus only on developing integration algorithms for the anisotropic evolution equations for \mathbf{C}_F^v and the material tangent for the anisotropic nonequilibrium component of the stress response.

4.3.1 Numerical Integration of the Evolution Equations

In a finite-element framework, the time integration of the evolution equations for the internal variables are performed at the integration point level. At time $t_{n+1} = t_n + \Delta t$, the updated internal variables are evaluated assuming that the updated values of the deformation gradient \mathbf{F}_{n+1} are given and that the previous values of the deformation

Table 4.2. Integration algorithm for $\mathbf{C}_{F_{n+1}}^v$ for N fiber-families model.

Residual $k + 1$ iteration:	$\mathbf{R}^{k+1} = \mathbf{C}_F^{v^{k+1}} - 2\Delta t (\mathbb{V}_F^{k+1})^{-1} : \mathbf{T}_F^{k+1} - \mathbf{C}_{F_n}^v = \mathbf{0},$ $\mathbf{T}_F = \sum_{\alpha=1}^N \tau_{F_\alpha}^{\text{neq}} \frac{\mathbf{M}_\alpha}{\mathbf{C}_F^v : \mathbf{M}_\alpha},$ $\mathbb{V}_F = \sum_{\alpha=1}^2 \frac{\eta_{F_\alpha}}{\lambda_{F_\alpha}^{v^4}} \mathbf{M}_\alpha \otimes \mathbf{M}_\alpha,$
Linearize about $\mathbf{C}_{F_{n+1}}^{v^k}$:	$\mathbf{R}^{k+1} \approx \mathbf{R}^k + \underbrace{\frac{\partial \mathbf{R}}{\partial \mathbf{C}_F^v}}_{\mathbb{K}} \Big _{\mathbf{C}_F^{v^k}} \Delta \mathbf{C}_F^v = \mathbf{0},$
Consistent tangent:	$\mathbb{K} = \mathbb{I} - \Delta t \mathbb{V}_F^{-1} : \left(2 \frac{\partial \mathbf{T}_F}{\partial \mathbf{C}_F^v} - \sum_{\alpha}^N \frac{1}{\lambda_\alpha} \frac{\partial \eta_{F_\alpha}}{\partial \lambda_\alpha} (\mathbf{M}_i : \mathbb{V}_F^{-1} : \mathbf{T}_F) \mathbf{M}_\alpha \otimes \mathbf{M}_\alpha \right),$ $2 \frac{\partial \mathbf{T}_F}{\partial \mathbf{C}_F^v} = \sum_{\alpha=1}^N -2 \frac{\partial \tau_{F_\alpha}^{\text{neq}}}{\partial I_{F_{2\alpha+2}}^e} I_{F_\alpha}^e \frac{\mathbf{M}_\alpha}{\mathbf{C}_F^v : \mathbf{M}_\alpha} \otimes \frac{\mathbf{M}_\alpha}{\mathbf{C}_F^v : \mathbf{M}_\alpha}$
Solve for the increment:	$\Delta \mathbf{C}_F^v = -\mathbb{K}^{-1} : \mathbf{R}^k \Big _{\mathbf{C}_F^{v^k}},$
Update solution:	$\mathbf{C}_F^{v^{k+1}} = \mathbf{C}_F^{v^k} + \Delta \mathbf{C}_F^v$
Repeat until:	$\ \mathbf{R}^{k+1}\ < c_{\text{tol}}.$
Increment of \mathbf{C}_F^v :	$\Delta \mathbf{C}_F^v = \mathbb{K}^{-1} : \mathbb{G} : \Delta \mathbf{C}$ $\mathbb{G} = \Delta t \mathbb{V}_F^{-1} : \left(2 \frac{\partial \mathbf{T}_F}{\partial \mathbf{C}} - \sum_i^N \frac{1}{\lambda_\alpha} \frac{\partial \eta_{F_\alpha}}{\partial \lambda_\alpha} (\mathbf{M}_\alpha : \mathbb{V}_F^{-1} : \mathbf{T}_F) \mathbf{M}_\alpha \otimes \mathbf{M}_\alpha \right).$ $2 \frac{\partial \mathbf{T}_F}{\partial \mathbf{C}} = \sum_{\alpha=1}^N 2 \frac{\partial \tau_{F_\alpha}^{\text{neq}}}{\partial I_{F_{2\alpha+2}}^e} \frac{\mathbf{M}_\alpha}{\mathbf{C}_F^v : \mathbf{M}_\alpha} \otimes \frac{\mathbf{M}_\alpha}{\mathbf{C}_F^v : \mathbf{M}_\alpha}.$
Algorithmic moduli:	$\mathbb{C}_F^{\text{neq}} = 2 \frac{\partial \mathbf{S}_F^{\text{neq}}}{\partial \mathbf{C}} + 2 \frac{\partial \mathbf{S}_F^{\text{neq}}}{\partial \mathbf{C}_F^v} : \mathbb{K}^{-1} : \mathbb{G},$ $2 \frac{\partial \mathbf{S}_F^{\text{neq}}}{\partial \mathbf{C}} = \sum_{\alpha=1}^N 4 \frac{\partial \mathcal{W}_{F_\alpha}^{\text{neq}}}{\partial I_{F_{2\alpha+2}}^e} \frac{\mathbf{M}_\alpha}{\mathbf{C}_F^v : \mathbf{M}_\alpha} \otimes \frac{\mathbf{M}_\alpha}{\mathbf{C}_F^v : \mathbf{M}_\alpha},$ $2 \frac{\partial \mathbf{S}_F^{\text{neq}}}{\partial \mathbf{C}_F^v} = \sum_{\alpha=1}^N -2 \frac{\partial \tau_{F_\alpha}^{\text{neq}}}{\partial I_{F_{2\alpha+2}}^e} \frac{\mathbf{M}_\alpha}{\mathbf{C}_F^v : \mathbf{M}_\alpha} \otimes \frac{\mathbf{M}_\alpha}{\mathbf{C}_F^v : \mathbf{M}_\alpha}$

gradient \mathbf{F}_n , previous values of the internal variables $\mathbf{C}_{M_n}^v$ and $\mathbf{C}_{F_n}^v$, and the structure tensors \mathbf{M}_α are known. For the constitutive model presented in Sec. 4.2.3 for N fiber-families, the flow rule in eq. (4.29) for λ_α^v can be integrated numerically using a backward Euler integration scheme. Applying the time discretization of the viscous stretch rate $\dot{\lambda}_\alpha^v = (\lambda_{\alpha_{n+1}}^v - \lambda_{\alpha_n}^v) / \Delta t$ to eq. (4.29) gives,

$$\lambda_{\alpha_{n+1}}^v - \left[\frac{\Delta t}{\eta_{F_\alpha}(\lambda_\alpha, \lambda_\alpha^v)} \tau_{F_\alpha}^{\text{neq}}(\lambda_\alpha^e) \right]_{n+1} \lambda_{\alpha_{n+1}}^v - \lambda_{\alpha_n}^v = 0, \quad (4.41)$$

where it has been assumed that the fiber viscosity, η_{F_α} , can depend generally on the total and viscous stretch, λ_α and λ_α^v . The N nonlinear equations are solved at each integration point for the updated values $\lambda_{\alpha_{n+1}}^v$ using the Newton solution algorithm presented in Table 4.1.

For the case where there are more than 3 fiber families arranged in a plane, and more than 6 fiber families in a fully three-dimensional arrangement, it is more efficient to solve for \mathbf{C}_F^v rather than for the viscous fiber stretches. The rate equation (4.30) is

inverted to give an evolution equation for \mathbf{C}_F^v ,

$$\dot{\mathbf{C}}_F^v = 2\mathbb{V}_F^{-1} : \mathbf{T}_F, \quad (4.42)$$

where the fourth order viscosity tensor \mathbb{V}_F given in eq. (4.30) is required to be invertible. A backward Euler discretization scheme is applied to eq. (4.42) to give,

$$\mathbf{C}_{F_{n+1}}^v - 2\Delta t \mathbb{V}_{F_{n+1}}^{-1} \mathbf{T}_{F_{n+1}} - \mathbf{C}_{F_n}^v = \mathbf{0}, \quad (4.43)$$

Equation (4.43) is a nonlinear equation for the updated values of \mathbf{C}_F^v that is solved at the integration point using the Newton scheme presented in Table 4.2.

Similarly for the generalized two fiber-families model presented in Sec. 4.2.4, a backward Euler integration scheme is applied to discretize the evolution equation (4.39) for the fiber viscous deformation. This results in the following nonlinear system of equations for $\mathbf{C}_{F_{n+1}}^v$,

$$\mathbf{C}_{F_{n+1}}^v - \sum_{\alpha=1}^2 \frac{2\Delta t}{\eta_{F\alpha}(\lambda_{\alpha_{n+1}}, \lambda_{\alpha_{n+1}}^v)} \left(\mathbf{T}_{F_{n+1}} : \text{sym} [\mathbf{M}_\alpha \mathbf{C}_{F_{n+1}}^v] \right) \text{sym} [\mathbf{M}_\alpha \mathbf{C}_{F_{n+1}}^v] - \mathbf{C}_{F_n}^v = \mathbf{0}. \quad (4.44)$$

This is solved at each integration point using the Newton solution algorithm described in Table 4.3.

4.3.2 Consistent Tangent Moduli

The implicit solution of an initial boundary value problem requires the time discretization of the deformation history and linearization of the constitutive relations about the deformation state at time t_n to solve for the updated deformation state at time $t_{n+1} = t_n + \Delta t$. The consistent material tangent moduli is defined by the linearization of the second Piola-Kirchhoff stress response for a time increment Δt as,

$$\Delta \mathbf{S}_{n+1} = \mathbb{C}_{n+1} : \frac{1}{2} \Delta \mathbf{C}_{n+1}. \quad (4.45)$$

The Second Piola-Kirchhoff stress tensor for the anisotropic viscoelastic models can be decomposed additively as,

$$\mathbf{S}_{n+1} = \mathbf{S}_{M_{n+1}}^{\text{eq}}(\mathbf{C}_{n+1}) + \mathbf{S}_{M_{n+1}}^{\text{neq}}(\mathbf{C}_{n+1}, \mathbf{C}_{M_{n+1}}^v) + \mathbf{S}_{F_{n+1}}^{\text{eq}}(\mathbf{C}_{n+1}) + \mathbf{S}_{F_{n+1}}^{\text{neq}}(\mathbf{C}_{n+1}, \mathbf{C}_{F_{n+1}}^v). \quad (4.46)$$

This allows \mathbb{C}_{n+1} also to be decomposed additively into equilibrium/nonequilibrium and isotropic/anisotropic components as,

$$\mathbb{C}_{n+1} = \mathbb{C}_{M_{n+1}}^{\text{eq}} + \mathbb{C}_{M_{n+1}}^{\text{neq}} + \mathbb{C}_{F_{n+1}}^{\text{eq}} + \mathbb{C}_{F_{n+1}}^{\text{neq}}. \quad (4.47)$$

Table 4.3. Integration algorithm for $\mathbf{C}_{F_{n+1}}^v$ for the two fiber-families model.

Residual $k + 1$ iteration:	$\mathbf{R}^{k+1} = \mathbf{C}_F^{v^{k+1}} - \sum_{\alpha=1}^2 \frac{\Delta t}{\eta_{F\alpha}} \left(\mathbf{T}_F^{k+1} : \text{sym} \left[\mathbf{M}_\alpha \mathbf{C}_F^{v^{k+1}} \right] \right) \text{sym} \left[\mathbf{M}_\alpha \mathbf{C}_F^{v^{k+1}} \right] - \mathbf{C}_{F_n}^v,$ $\mathbf{T}_F = \sum_{\alpha=1}^2 \left(2 \frac{\partial \mathcal{W}_{F\alpha}^{\text{neq}}}{\partial I_{F_{2\alpha+2}}^e} I_{F_{2\alpha+2}}^e + 2 \frac{\partial \mathcal{W}_{F\alpha}^{\text{neq}}}{\partial I_{F_{2\alpha+3}}^e} I_{F_{2\alpha+3}}^e \right) \frac{\mathbf{M}_\alpha}{\mathbf{C}_F^v : \mathbf{M}_\alpha} + 2 \frac{\partial \mathcal{W}_{F\alpha}^{\text{neq}}}{\partial I_{F_{2\alpha+3}}^e} \frac{\mathbf{C}_F^{v-1} \mathbf{C} \mathbf{M}_\alpha \mathbf{C} \mathbf{C}_F^{v-1}}{\mathbf{C}_F^v : \mathbf{M}_\alpha},$
Linearize about $\mathbf{C}_{F_{n+1}}^{v^k}$:	$\mathbf{R}^{k+1} \approx \mathbf{R}^k + \underbrace{\frac{\partial \mathbf{R}}{\partial \mathbf{C}_F^v}}_{\mathbb{K}} \Big _{\mathbf{C}_F^{v^k}} \Delta \mathbf{C}_F^v = 0,$
Consistent tangent:	$\mathbb{K} = \mathbb{I} - \sum_{\alpha=1}^2 \frac{\Delta t}{\eta_{F\alpha}} \left(\mathbf{T}_F : \text{sym} \left[\mathbf{M}_\alpha \mathbf{C}_F^v \right] (\mathbf{1} \odot \mathbf{M}_\alpha + \mathbf{M}_\alpha \odot \mathbf{1}) - 2 \text{sym} \left[\mathbf{M}_\alpha \mathbf{C}_F^v \right] \otimes \text{sym} \left[\mathbf{M}_\alpha \mathbf{T}_F \right] - \text{sym} \left[\mathbf{M}_\alpha \mathbf{C}_F^v \right] \otimes \text{sym} \left[\mathbf{M}_\alpha \mathbf{C}_F^v \right] : 2 \frac{\partial \mathbf{T}_F}{\partial \mathbf{C}_F^v} \right)$ $2 \frac{\partial \mathbf{T}_F}{\partial \mathbf{C}_F^v} = \sum_{\alpha=1}^2 \left(4 \frac{\partial^2 \mathcal{W}_F^{\text{neq}}}{\partial I_{F_{2\alpha+2}}^e{}^2} + 4 \frac{\partial^2 \mathcal{W}_F^{\text{neq}}}{\partial I_{F_{2\alpha+3}}^e{}^2} + 8 \frac{\partial \mathcal{W}_F^{\text{neq}}}{\partial I_{F_{2\alpha+2}}^e} + 8 \frac{\partial \mathcal{W}_F^{\text{neq}}}{\partial I_{F_{2\alpha+3}}^e} \right) \frac{\mathbf{M}_\alpha}{\mathbf{C}_F^v : \mathbf{M}_\alpha} \otimes \frac{\mathbf{M}_\alpha}{\mathbf{C}_F^v : \mathbf{M}_\alpha} + \left(4 \frac{\partial^2 \mathcal{W}_F^{\text{neq}}}{\partial I_{F_{2\alpha+2}}^e{}^2} I_{F_{2\alpha+3}}^e + 4 \frac{\partial \mathcal{W}_F^{\text{neq}}}{\partial I_{F_{2\alpha+3}}^e} \right) \left(\frac{\mathbf{M}_\alpha}{\mathbf{C}_F^v : \mathbf{M}_\alpha} \otimes \frac{\mathbf{C}_F^{v-1} \mathbf{C} \mathbf{M}_\alpha \mathbf{C} \mathbf{C}_F^{v-1}}{\mathbf{C}_F^v : \mathbf{M}_\alpha} + \frac{\mathbf{C}_F^{v-1} \mathbf{C} \mathbf{M}_\alpha \mathbf{C} \mathbf{C}_F^{v-1}}{\mathbf{C}_F^v : \mathbf{M}_\alpha} \otimes \frac{\mathbf{M}_\alpha}{\mathbf{C}_F^v : \mathbf{M}_\alpha} \right) + 4 \frac{\partial^2 \mathcal{W}_F^{\text{neq}}}{\partial I_{F_{2\alpha+3}}^e{}^2} \left(\frac{\mathbf{C}_F^{v-1} \mathbf{C} \mathbf{M}_\alpha \mathbf{C} \mathbf{C}_F^{v-1}}{\mathbf{C}_F^v : \mathbf{M}_\alpha} \otimes \frac{\mathbf{C}_F^{v-1} \mathbf{C} \mathbf{M}_\alpha \mathbf{C} \mathbf{C}_F^{v-1}}{\mathbf{C}_F^v : \mathbf{M}_\alpha} \right) + 4 \frac{\partial \mathcal{W}_F^{\text{neq}}}{\partial I_{F_{2\alpha+3}}^e} \left(\frac{\mathbf{C}_F^{v-1} \odot \mathbf{C}_F^{v-1} \mathbf{C} \mathbf{M}_\alpha \mathbf{C} \mathbf{C}_F^{v-1}}{\mathbf{C}_F^v : \mathbf{M}_\alpha} + \frac{\mathbf{C}_F^{v-1} \mathbf{C} \mathbf{M}_\alpha \mathbf{C} \mathbf{C}_F^{v-1} \odot \mathbf{C}_F^{v-1}}{\mathbf{C}_F^v : \mathbf{M}_\alpha} \right)$
Solve for increment:	$\Delta \mathbf{C}_F^v = -\mathbb{K}^{-1} : \mathbf{R}^k \Big _{\lambda_i^{v^k}},$
Update solution:	$\mathbf{C}_F^{v^{k+1}} = \mathbf{C}_F^{v^k} + \Delta \mathbf{C}_F^v$
Repeat until:	$\ \mathbf{R}^{k+1}\ < c_{\text{tol}}.$

Table 4.4. Algorithmic anisotropic moduli for the two fiber-families model.

<p>Increment of \mathbf{C}_F^v: $\Delta \mathbf{C}_F^v = \mathbb{K}^{-1} : \mathbb{G} : \Delta \mathbf{C}$</p> $\mathbb{G} = \sum_{\alpha=1}^2 \frac{\Delta t}{\eta_{F\alpha}} \left(\text{sym} [\mathbf{M}_\alpha \mathbf{C}_F^v] \otimes \text{sym} [\mathbf{M}_\alpha \mathbf{C}_F^v] : 2 \frac{\partial \mathbf{T}_F}{\partial \mathbf{C}} \right),$ $2 \frac{\partial \mathbf{T}_F}{\partial \mathbf{C}} = - \sum_{\alpha=1}^2 \left(4 \frac{\partial^2 \mathcal{W}_F^{\text{neq}}}{\partial I_{F2\alpha+2}^{e^2}} + 4 \frac{\partial \mathcal{W}_F^{\text{neq}}}{\partial I_{F2\alpha+2}^e} \right) \frac{\mathbf{M}_\alpha}{\mathbf{C}_F^v : \mathbf{M}_\alpha} \otimes \frac{\mathbf{M}_\alpha}{\mathbf{C}_F^v : \mathbf{M}_\alpha}$ $+ \left(4 \frac{\partial^2 \mathcal{W}_F^{\text{neq}}}{\partial I_{F2\alpha+2}^{e^2}} I_{F2\alpha+3}^e + 4 \frac{\partial \mathcal{W}_F^{\text{neq}}}{\partial I_{F2\alpha+3}^e} \right) \frac{\mathbf{M}_\alpha}{\mathbf{C}_F^v : \mathbf{M}_\alpha} \otimes \frac{\mathbf{M}_\alpha \mathbf{C}_F^{v-1} + \mathbf{C}_F^{v-1} \mathbf{M}_\alpha}{\mathbf{C}_F^v : \mathbf{M}_\alpha},$ $+ 4 \frac{\partial^2 \mathcal{W}_F^{\text{neq}}}{\partial I_{F2\alpha+3}^{e^2}} \left(\frac{\mathbf{C}_F^{v-1} \mathbf{M}_\alpha \mathbf{C}_F^{v-1}}{\mathbf{C}_F^v : \mathbf{M}_\alpha} \otimes \frac{\mathbf{C}_F^{v-1} \mathbf{M}_\alpha \mathbf{C}_F^{v-1}}{\mathbf{C}_F^v : \mathbf{M}_\alpha} \right)$ $+ 4 \frac{\partial \mathcal{W}_F^{\text{neq}}}{\partial I_{F2\alpha+3}^e} \left(\frac{\mathbf{C}_F^{v-1} \odot \mathbf{C}_F^{v-1} \mathbf{M}_\alpha \mathbf{C}_F^{v-1}}{\mathbf{C}_F^v : \mathbf{M}_\alpha} + \frac{\mathbf{C}_F^{v-1} \mathbf{M}_\alpha \mathbf{C}_F^{v-1} \odot \mathbf{C}_F^{v-1}}{\mathbf{C}_F^v : \mathbf{M}_\alpha} \right).$
<p>Algorithmic moduli: $\mathbb{C}_F^{\text{neq}} = 2 \frac{\partial \mathbf{S}_F^{\text{neq}}}{\partial \mathbf{C}} + 2 \frac{\partial \mathbf{S}_F^{\text{neq}}}{\partial \mathbf{C}_F^v} : \mathbb{K}^{-1} : \mathbb{G},$</p> $2 \frac{\partial \mathbf{S}_F^{\text{neq}}}{\partial \mathbf{C}} = - \sum_{\alpha=1}^2 4 \frac{\partial^2 \mathcal{W}_F^{\text{neq}}}{\partial I_{F2\alpha+2}^{e^2}} \frac{\mathbf{M}_\alpha}{\mathbf{C}_F^v : \mathbf{M}_\alpha} \otimes \frac{\mathbf{M}_\alpha}{\mathbf{C}_F^v : \mathbf{M}_\alpha}$ $+ 4 \frac{\partial^2 \mathcal{W}_F^{\text{neq}}}{\partial I_{F2\alpha+3}^{e^2}} \frac{\mathbf{M}_\alpha \mathbf{C}_F^{v-1} + \mathbf{C}_F^{v-1} \mathbf{M}_\alpha}{\mathbf{C}_F^v : \mathbf{M}_\alpha} \otimes \frac{\mathbf{M}_\alpha \mathbf{C}_F^{v-1} + \mathbf{C}_F^{v-1} \mathbf{M}_\alpha}{\mathbf{C}_F^v : \mathbf{M}_\alpha},$ $+ 4 \frac{\partial \mathcal{W}_F^{\text{neq}}}{\partial I_{F2\alpha+3}^e} \frac{\mathbf{C}_F^{v-1} \odot \mathbf{M}_\alpha \mathbf{C}_F^{v-1} + \mathbf{M}_\alpha \mathbf{C}_F^{v-1} \odot \mathbf{C}_F^{v-1}}{\mathbf{C}_F^v : \mathbf{M}_\alpha}.$ $2 \frac{\partial \mathbf{S}_F^{\text{neq}}}{\partial \mathbf{C}_F^v} = - \sum_{\alpha=1}^2 \left(4 \frac{\partial^2 \mathcal{W}_F^{\text{neq}}}{\partial I_{F2\alpha+2}^{e^2}} + 4 \frac{\partial \mathcal{W}_F^{\text{neq}}}{\partial I_{F2\alpha+2}^e} \right) \frac{\mathbf{M}_\alpha}{\mathbf{C}_F^v : \mathbf{M}_\alpha} \otimes \frac{\mathbf{M}_\alpha}{\mathbf{C}_F^v : \mathbf{M}_\alpha}$ $+ 4 \frac{\partial^2 \mathcal{W}_F^{\text{neq}}}{\partial I_{F2\alpha+3}^{e^2}} I_{F2\alpha+3}^e \frac{\mathbf{M}_\alpha \mathbf{C}_F^{v-1} + \mathbf{C}_F^{v-1} \mathbf{M}_\alpha}{\mathbf{C}_F^v : \mathbf{M}_\alpha} \otimes \left(I_{F2\alpha+3}^e \frac{\mathbf{M}_\alpha}{\mathbf{C}_F^v : \mathbf{M}_\alpha} + \frac{\mathbf{C}_F^{v-1} \mathbf{M}_\alpha \mathbf{C}_F^{v-1}}{\mathbf{C}_F^v : \mathbf{M}_\alpha} \right)$ $+ 4 \frac{\partial \mathcal{W}_F^{\text{neq}}}{\partial I_{F2\alpha+3}^e} \frac{\mathbf{C}_F^{v-1} \odot \mathbf{M}_\alpha \mathbf{C}_F^{v-1} + \mathbf{M}_\alpha \mathbf{C}_F^{v-1} \odot \mathbf{C}_F^{v-1}}{\mathbf{C}_F^v : \mathbf{M}_\alpha}$

Because the isotropic component of the stress response depends only on \mathbf{C} , the equilibrium components of the material tangent moduli can be evaluated simply as,

$$\mathbb{C}_M^{\text{eq}} = 2 \frac{\partial \mathbf{S}_M^{\text{eq}}}{\partial \mathbf{C}}, \quad \mathbb{C}_F^{\text{eq}} = 2 \frac{\partial \mathbf{S}_F^{\text{eq}}}{\partial \mathbf{C}}. \quad (4.48)$$

The isotropic equilibrium part of the viscoelastic models is essentially a standard isotropic hyperelastic model. Thus, \mathbb{C}_M^{eq} can be evaluated in the same manner as the material tangent moduli in isotropic hyperelasticity (see such nonlinear mechanics textbooks as [66, Ch. 6] and [38, Ch. 6]). From eq. (4.48), the anisotropic equilibrium part of the material moduli can be derived from \mathbf{S}_F^{eq} in eq. (4.20) for the N fiber-families model as,

$$\mathbb{C}_F^{\text{eq}} = \sum_{\alpha=1}^N 4 \frac{\partial^2 \mathcal{W}_{F\alpha}^{\text{eq}}}{\partial I_{\alpha+3}^2} \mathbf{M}_\alpha \otimes \mathbf{M}_\alpha. \quad (4.49)$$

Similarly it can be derived from \mathbf{S}_F^{eq} given in eq. (4.32) for the generalized two fiber-families model as,

$$\begin{aligned} \mathbb{C}_F^{\text{eq}} = \sum_{\alpha=1}^2 4 \frac{\partial^2 \mathcal{W}_{F\alpha}^{\text{eq}}}{\partial I_{2\alpha+2}^2} \mathbf{M}_\alpha \otimes \mathbf{M}_\alpha + \sum_{\alpha=1}^2 \left(4 \frac{\partial^2 \mathcal{W}_{F\alpha}^{\text{eq}}}{\partial I_{2\alpha+3}^2} (\mathbf{C} \mathbf{M}_\alpha + \mathbf{M}_\alpha \mathbf{C}) \otimes (\mathbf{C} \mathbf{M}_\alpha + \mathbf{M}_\alpha \mathbf{C}) \right. \\ \left. + 4 \frac{\partial \mathcal{W}_{F\alpha}^{\text{eq}}}{\partial I_{2\alpha+3}} (\mathbf{1} \odot \mathbf{M}_\alpha + \mathbf{M}_\alpha \odot \mathbf{1}) \right), \quad (4.50) \end{aligned}$$

where the tensor in the final expression is defined as $(\mathbf{1} \odot \mathbf{M})_{IJKL} = \frac{1}{2}(\delta_{IK} M_{JL} + \delta_{IL} M_{JK})$.

The isotropic nonequilibrium part of the model is identical to the isotropic viscoelastic model developed by [74] and it is recommended that their numerical method be applied to solve for the internal stretches of the spatial form of the evolution eq. (4.24) and to derive the material tangent moduli $\mathbb{C}_M^{\text{neq}}$. The anisotropic nonequilibrium part of the material moduli is evaluated by first linearizing the anisotropic nonequilibrium component of the stress response $\mathbf{S}_F^{\text{neq}}$ as,

$$\Delta \mathbf{S}_F^{\text{neq}} = 2 \frac{\partial \mathbf{S}_F^{\text{neq}}}{\partial \mathbf{C}} : \frac{1}{2} \Delta \mathbf{C} + 2 \frac{\partial \mathbf{S}_F^{\text{neq}}}{\partial \mathbf{C}_F^{\text{v}}} : \frac{1}{2} \Delta \mathbf{C}_F^{\text{v}}. \quad (4.51)$$

Determining $\mathbb{C}_F^{\text{neq}}$ in eq. (4.51) requires developing a relationship between the increment $\Delta \mathbf{C}_F^{\text{v}}$ of the fiber phase, which is solved locally at the integration point, and the increment $\Delta \mathbf{C}$ of the global solution algorithm. For the N fiber-families model, this relationship can be determined for the integration algorithm described in Table 4.1 by linearizing the residual equation $r_\alpha(\lambda_{\alpha_{n+1}}, \lambda_{\alpha_{n+1}}^{\text{v}}) = 0$. Considering that $\lambda_{\alpha_{n+1}}$ is not a constant in the global solution algorithm, this yields,

$$\begin{aligned} \underbrace{\frac{\partial r_\alpha}{\partial \lambda_\alpha^{\text{v}}}}_{k_\alpha} \Delta \lambda_\alpha^{\text{v}} + \underbrace{\frac{\partial r_\alpha}{\partial \lambda_\alpha}}_{-g_\alpha} \Delta \lambda_\alpha = 0, \\ \Delta \mathbf{C}_F^{\text{v}} : \mathbf{M}_\alpha = \frac{g_\alpha}{k_\alpha \lambda_\alpha^{\text{e}}} \Delta \mathbf{C} : \mathbf{M}_\alpha, \end{aligned} \quad (4.52)$$

where the expressions for k_α and g_α are given in Table 4.1. Substituting the final relation into eq. (4.51) and factoring out $\Delta \mathbf{C}$ gives,

$$\mathbf{C}_F^{\text{neq}} = \sum_{\alpha=1}^N \left(4 \frac{\partial^2 \mathcal{W}_{F_\alpha}^{\text{neq}}}{\partial I_{F_{\alpha+3}}^2} - 4 \left(\frac{\partial^2 \mathcal{W}_{F_\alpha}^{\text{neq}}}{\partial I_{F_{\alpha+3}}^2} I_{F_{\alpha+3}}^e + \frac{\partial \mathcal{W}_{F_\alpha}^{\text{neq}}}{\partial I_{F_{\alpha+3}}^e} \right) \frac{g_\alpha}{k_\alpha \sqrt{I_{F_{\alpha+3}}^e}} \right) \frac{\mathbf{M}_\alpha}{\mathbf{C}_F^{\text{v}} : \mathbf{M}_\alpha} \otimes \frac{\mathbf{M}_\alpha}{\mathbf{C}_F^{\text{v}} : \mathbf{M}_\alpha}. \quad (4.53)$$

Similarly for the integration algorithms presented in Tables 4.2 and 4.3, a relationship for the the increment $\Delta \mathbf{C}_{F_{n+1}}^{\text{v}}$ is obtained by linearizing the residual equation $\mathbf{R}(\mathbf{C}_{F_{n+1}}^{\text{v}}, \mathbf{C}_{n+1}) = \mathbf{0}$ for a non-constant \mathbf{C}_{n+1} . The result,

$$\Delta \mathbf{C}_F^{\text{v}} = \mathbb{K}^{-1} : \mathbb{G} : \Delta \mathbf{C}, \quad (4.54)$$

is substituted into eq. (4.52) to give the following general expression for the anisotropic nonequilibrium component of the material tangent moduli,

$$\mathbf{C}_F^{\text{neq}} = 2 \frac{\partial \mathbf{S}_F^{\text{neq}}}{\partial \mathbf{C}} + 2 \frac{\partial \mathbf{S}_F^{\text{neq}}}{\partial \mathbf{C}_F^{\text{v}}} : \mathbb{K}^{-1} : \mathbb{G}. \quad (4.55)$$

The tensors \mathbb{K} and \mathbb{G} are specific to the solution algorithm of $\mathbf{C}_{F_{n+1}}^{\text{v}}$ and are given in Table 4.2 for the N fiber-families model and in Table 4.4 for the generalized two fiber-families model.

4.4 Linearization for the Small-Strain Limit

This section presents the linearization of the examples Model I and II presented in Sec. 4.7 to obtain expressions for the long- and short-time moduli and characteristic relaxation times in the small-strain limit. For both models, the isotropic stress response of the matrix, $\boldsymbol{\sigma}_M$, is obtained by substituting eq. (4.72) into eq. (4.21) to give

$$\boldsymbol{\sigma}_M = \underbrace{\frac{1}{\sqrt{I_3}} \left[\mu^{\text{eq}} \left(\bar{\mathbf{b}} - \frac{1}{3} \bar{I}_1 \mathbf{1} \right) + \mu^{\text{neq}} \left(\bar{\mathbf{b}}_M^e - \frac{1}{3} \bar{I}_{M_1}^e \mathbf{1} \right) \right]}_{\mathbf{s}_M} + \underbrace{\frac{\kappa}{2} \left(\sqrt{I_3} - \frac{1}{\sqrt{I_3}} \right)}_{p_M} \mathbf{1}, \quad (4.56)$$

where $\bar{\mathbf{b}} = I_3^{-\frac{1}{3}} \mathbf{b}$ and $\bar{\mathbf{b}}_M^e = I_{M_3}^{e-\frac{1}{3}} \mathbf{b}_M^e$. Applying the stress response in eq.(4.56) to the spatial form of the evolution equation for the matrix (see Section 4.5) gives,

$$-\frac{1}{2} \mathcal{L}_v \mathbf{b}_M^e \mathbf{b}_M^{e-1} = \frac{\mu^{\text{neq}}}{2\eta_{M_S}} \left(\bar{\mathbf{b}}_M^e - \frac{1}{3} \bar{I}_{M_1}^e \mathbf{1} \right), \quad (4.57)$$

where $\mathcal{L}_v \mathbf{b}_M^e = \dot{\mathbf{F}} \mathbf{C}_M^{\text{v}-1} \mathbf{F}^T$ is the Lie time derivative of \mathbf{b}_M^e .

For Model I, the anisotropic component of the Cauchy stress tensor is obtained by applying eq. (4.73) to eq. (4.21),

$$\boldsymbol{\sigma}_F = \frac{1}{\sqrt{I_3}} \left[\sum_{\alpha=1}^2 2k^{\text{eq}} (I_{\alpha+3} - 1) I_{\alpha+3} \mathbf{m}_\alpha + \sum_{\alpha=1}^2 2k^{\text{neq}} (I_{F_{\alpha+3}}^e - 1) I_{F_{\alpha+3}}^e \mathbf{m}_\alpha \right]. \quad (4.58)$$

Applying eq. (4.58) to eq. (4.29), the fiber flow rule can be written as,

$$\frac{\dot{\lambda}_\alpha^v}{\lambda_\alpha^v} = \frac{2k^{\text{neq}}}{\eta_F} (I_{F_{\alpha+3}}^e - 1) I_{F_{\alpha+3}}^e. \quad (4.59)$$

Similarly, $\boldsymbol{\sigma}_F$ for Model II is calculated as,

$$\begin{aligned} \boldsymbol{\sigma}_F = & \frac{2}{\sqrt{I_3}} \sum_{\alpha=1}^2 k^{\text{eq}} (I_{2\alpha+3} - 1) I_{2\alpha+3} (\mathbf{b}\mathbf{m}_\alpha + \mathbf{m}_\alpha\mathbf{b}) \\ & + \frac{2}{\sqrt{I_3}} \sum_{\alpha=1}^2 k^{\text{neq}} (I_{F_{2\alpha+3}}^e - 1) I_{F_{2\alpha+3}}^e (\mathbf{b}_F^e \mathbf{m}_\alpha + \mathbf{m}_\alpha \mathbf{b}_F^e). \end{aligned} \quad (4.60)$$

Combining eqs. (4.60) and (4.36) gives the following flow rule for λ_α^v for Model II,

$$\frac{\dot{\lambda}_\alpha^v}{\lambda_\alpha^v} = \frac{2}{\eta_F} k^{\text{neq}} (I_{F_{2\alpha+3}}^e - 1) \left(I_{F_{2\alpha+3}}^e + \sum_{\beta}^2 \left(\frac{\mathbf{C}_F^{v-1} \mathbf{C} \mathbf{M}_\beta : \mathbf{M}_\alpha \mathbf{C}}{\mathbf{C}_F^v : \mathbf{M}_\beta} + \frac{\mathbf{M}_\beta \mathbf{C} \mathbf{C}_F^{v-1} : \mathbf{C} \mathbf{M}_\alpha}{\mathbf{C}_F^v : \mathbf{M}_\beta} \right) \right). \quad (4.61)$$

To examine the small strain behavior of the two models, the linearized Green-Lagrange strain is defined as $\boldsymbol{\varepsilon} = \frac{1}{2}(\mathbf{C} - \mathbf{1})$ and the associated linearized elastic and viscous strain tensors are defined as $\boldsymbol{\varepsilon}^v = \frac{1}{2}(\mathbf{C}^v - \mathbf{1})$ and $\boldsymbol{\varepsilon}^e = \boldsymbol{\varepsilon} - \boldsymbol{\varepsilon}^v$ for both the matrix and fiber phases. Moreover, the structure tensor in the various configuration reduces in the small-strain limit to $\mathbf{m}_\alpha \rightarrow \bar{\mathbf{M}}_\alpha \rightarrow \mathbf{M}_\alpha$. In the limit of small strains, the models reduces to a three-dimensional generalization of the rheological model shown in Fig. 4.1 of two standard three parameter models arranged in parallel. Separately, the two standard models describe the viscoelastic behavior of the matrix and fiber phases and their parallel combination describes the viscoelastic behavior of the composite. The strain $\boldsymbol{\varepsilon}$ is the total strain of the rheological model, while $\boldsymbol{\varepsilon}_M^e$ and $\boldsymbol{\varepsilon}_F^e$ are the strains of the springs in the Maxwell elements. The linearized evolution equations developed below for the viscous strains $\boldsymbol{\varepsilon}_M^v$ and $\boldsymbol{\varepsilon}_F^v$ govern the flow of the dashpots in the two Maxwell elements representing the relaxation of the matrix and fiber phases.

The small-strain short-time stress response ($t \rightarrow 0$) of Model I is computed by linearizing eqs. (4.56) and (4.58) in the limit $\boldsymbol{\varepsilon}_M^e \rightarrow \boldsymbol{\varepsilon}_F^e \rightarrow \boldsymbol{\varepsilon}$ to give,

$$\boldsymbol{\sigma}_o = \underbrace{\left(2(\mu^{\text{eq}} + \mu^{\text{neq}}) \left(\mathbb{I} - \frac{1}{3} \mathbf{1} \otimes \mathbf{1} \right) + \kappa \mathbf{1} \otimes \mathbf{1} + \sum_{\alpha=1}^2 4(k^{\text{eq}} + k^{\text{neq}}) \mathbf{M}_\alpha \otimes \mathbf{M}_\alpha \right)}_{\mathbf{c}_o} : \boldsymbol{\varepsilon}. \quad (4.62)$$

The tensor \mathbf{c}_o is defined as the small-strain short-time moduli. Similarly, the small-strain long-time ($t \rightarrow \infty$) stress response of Model I is computed by linearizing eqs. (4.56) and (4.58) in the limit $\boldsymbol{\varepsilon}_M^v \rightarrow \boldsymbol{\varepsilon}_F^v \rightarrow \boldsymbol{\varepsilon}$ to yield,

$$\boldsymbol{\sigma}_\infty = \underbrace{\left(2\mu^{\text{eq}} \left(\mathbb{I} - \frac{1}{3} \mathbf{1} \otimes \mathbf{1} \right) + \kappa \mathbf{1} \otimes \mathbf{1} + \sum_{\alpha=1}^2 4k^{\text{eq}} \mathbf{M}_\alpha \otimes \mathbf{M}_\alpha \right)}_{\mathbf{c}_\infty} : \boldsymbol{\varepsilon}. \quad (4.63)$$

The short- and long-time small-strain moduli can be computed for Model II in the same manner to give,

$$\begin{aligned} \mathbf{c}_o &= 2(\mu^{\text{eq}} + \mu^{\text{neq}}) \left(\mathbb{I} - \frac{1}{3} \mathbf{1} \otimes \mathbf{1} \right) + \kappa \mathbf{1} \otimes \mathbf{1} + \sum_{\alpha=1}^2 16(k^{\text{eq}} + k^{\text{neq}}) \mathbf{M}_\alpha \otimes \mathbf{M}_\alpha, \\ \mathbf{c}_\infty &= 2\mu^{\text{eq}} \left(\mathbb{I} - \frac{1}{3} \mathbf{1} \otimes \mathbf{1} \right) + \kappa \mathbf{1} \otimes \mathbf{1} + \sum_{\alpha=1}^2 16k^{\text{neq}} \mathbf{M}_\alpha \otimes \mathbf{M}_\alpha. \end{aligned} \quad (4.64)$$

To obtain the characteristic relaxation time of the matrix, eq. (4.57) is linearized as,

$$\dot{\mathbf{e}}_M^v = \frac{1}{\xi_M} \left(\mathbb{I} - \frac{1}{3} \mathbf{1} \otimes \mathbf{1} \right) : \mathbf{e}_M^e, \quad (4.65)$$

where $\mathbf{e}_M^v = \boldsymbol{\varepsilon}_M^v - \text{tr}(\boldsymbol{\varepsilon}_M^v) \mathbf{1}$, and $\mathbf{e}_M^e = \boldsymbol{\varepsilon}_M^e - \text{tr}(\boldsymbol{\varepsilon}_M^e) \mathbf{1}$ are the deviatoric strain components. The parameter $\xi_M = \eta_{M_S} / \mu^{\text{neq}}$ is the characteristic relaxation time of the matrix. The characteristic relaxation time of the fiber phase is obtained for Models I and II by linearizing eqs. (4.59) and (4.61). The result can be expressed as,

$$\dot{\mathbf{e}}_F^v : \mathbf{M}_\alpha = \frac{1}{\xi_F} \boldsymbol{\varepsilon}_F^e : \mathbf{M}_\alpha, \quad (4.66)$$

where $\xi_F = \eta_F / (4k^{\text{neq}})$ is the characteristic relaxation time of the fiber phase for Model I and $\xi_F = \eta_F / (16k^{\text{neq}})$ is for Model II.

4.5 Viscoelastic Evolution of the Matrix Phase

The following demonstrates that the spatial representation of eq. (4.24) is identical to the evolution equation developed for the isotropic viscoelasticity theory of [74]. First the evolution equation (4.24) is rewritten as follows,

$$\begin{aligned} \frac{1}{2} \dot{\mathbf{C}}_M^v &= \underbrace{\left(\frac{1}{2\eta_{M_S}} \left(\mathbf{C}_M^v \odot \mathbf{C}_M^v - \frac{1}{3} \mathbf{C}_M^v \otimes \mathbf{C}_M^v \right) + \frac{1}{9\eta_{M_B}} \mathbf{C}_M^v \otimes \mathbf{C}_M^v \right)}_{\mathbb{V}_M^{-1}} : \mathbf{T}_M \\ -\frac{1}{2} \dot{\mathbf{C}}_M^{v^{-1}} &= \frac{1}{2\eta_{M_S}} \left(\mathbf{T}_M - \frac{1}{3} (\mathbf{T}_M : \mathbf{C}_M^v) \mathbf{C}_M^{v^{-1}} \right) + \frac{1}{9\eta_{M_B}} (\mathbf{T}_M : \mathbf{C}_M^v) \mathbf{C}_M^{v^{-1}}, \end{aligned} \quad (4.67)$$

where the relation $-\frac{1}{2}\overline{\mathbf{C}_M^{v-1}} = \mathbf{C}_M^{v-1}\dot{\mathbf{C}}_M^v\mathbf{C}_M^{v-1}$ has been applied. The symmetric flow stress of the matrix phase in eq. (4.23) can be expressed as, $\mathbf{T}_M = \mathbf{C}_M^{v-1}\mathbf{C}\mathbf{S}_M^{\text{neq}} = \mathbf{S}_M^{\text{neq}}\mathbf{C}\mathbf{C}_M^{v-1}$, such that $\mathbf{T}_M : \mathbf{C}_M^v = \boldsymbol{\tau}_M^{\text{neq}} : \mathbf{1}$. Pushing eq. (4.67) forward with \mathbf{F} and applying $\mathbf{F}\mathbf{C}_M^{v-1}\mathbf{F}^T = \mathbf{b}_M^e$, $\mathbf{F}\overline{\mathbf{C}_M^{v-1}}\mathbf{F}^T = \mathcal{L}_v\mathbf{b}_M^e$, and $\mathbf{F}\mathbf{T}_M\mathbf{F}^T = \boldsymbol{\tau}_M^{\text{neq}}\mathbf{b}_M^e$ gives,

$$-\frac{1}{2}\mathcal{L}_v\mathbf{b}_M^e\mathbf{b}_M^{e-1} = \underbrace{\left(\frac{1}{2\eta_{M_S}}\left(\mathbb{I} - \frac{1}{3}\mathbf{1} \otimes \mathbf{1}\right) + \frac{1}{9\eta_{M_B}}\mathbf{1} \otimes \mathbf{1}\right)}_{\boldsymbol{\eta}_M^{-1}} : \boldsymbol{\tau}_F^{\text{neq}}, \quad (4.68)$$

which is the evolution equation developed by [74].

4.6 Fiber Flow Stress for an Orthotropic Fiber Arrangement

This section presents the development of the relationship in eq. (4.35) for the components of $\boldsymbol{\tau}_F^{\text{neq}}$ and \mathbf{T}_F . The term $\boldsymbol{\tau}_F^{\text{neq}} : \text{sym}[\mathbf{m}_\alpha\mathbf{b}^{-1}]$ can be evaluated as,

$$\begin{aligned} \boldsymbol{\tau}_F^{\text{neq}} : \text{sym}[\mathbf{m}_\alpha\mathbf{b}^{-1}] &= \sum_{\alpha=1}^2 \left(\frac{2}{I_{2\alpha+2}} \frac{\partial \mathcal{W}_{F_\alpha}^{\text{neq}}}{\partial I_{F_{2\alpha+2}}^e} I_{F_{2\alpha+2}}^e + \frac{2}{I_{2\alpha+2}} \frac{\partial \mathcal{W}_{F_\alpha}^{\text{neq}}}{\partial I_{F_{2\alpha+3}}^e} \mathbf{b}^e : \mathbf{m}_\alpha \right. \\ &\quad \left. + \sum_{\beta}^2 2 \frac{\partial \mathcal{W}_{F_\beta}^{\text{neq}}}{\partial I_{F_{2\beta+3}}^e} I_{F_{2\beta+2}}^e \frac{1}{2} (\mathbf{b}_F^e \mathbf{m}_\beta : \mathbf{m}_\alpha \mathbf{b}^{-1} + \mathbf{m}_\beta \mathbf{b}_F^e : \mathbf{m}_\alpha \mathbf{b}^{-1}) \right). \end{aligned} \quad (4.69)$$

It can be shown from eq. (4.15) that $\mathbf{b}^e : \mathbf{m}_\alpha = I_{F_{2\alpha+3}}^e$. Using this relation, the final term in eq. (4.69) can be rearranged to give,

$$\begin{aligned} &\frac{1}{2} (\mathbf{b}_F^e \mathbf{m}_\beta : \mathbf{m}_\alpha \mathbf{b}^{-1} + \mathbf{m}_\beta \mathbf{b}_F^e : \mathbf{m}_\alpha \mathbf{b}^{-1}) \\ &= \frac{1}{2I_{2\alpha+2}} \left(\frac{\mathbf{C}_F^{v-1} \mathbf{C} \mathbf{M}_\beta : \mathbf{M}_\alpha \mathbf{C}}{\mathbf{C}_F^v : \mathbf{M}_\beta} + \frac{\mathbf{M}_\beta \mathbf{C} \mathbf{C}_F^{v-1} : \mathbf{C} \mathbf{M}_\alpha}{\mathbf{C}_F^v : \mathbf{M}_\beta} \right) \end{aligned} \quad (4.70)$$

Substituting this result into eq. (4.69) yields $I_{2\alpha+2}\boldsymbol{\tau}_F^{\text{neq}} : \text{sym}[\mathbf{m}_\alpha\mathbf{b}^{-1}] = \boldsymbol{\tau}_{F_\alpha}^{\text{neq}}$. In the same manner, the term $\mathbf{T}_F : \text{sym}[\mathbf{M}_\alpha\mathbf{C}_F^v]$ can be evaluated to give,

$$\begin{aligned} \mathbf{T}_F : \text{sym}[\mathbf{M}_\alpha\mathbf{C}_F^v] &= \sum_{\alpha=1}^2 \left(2 \frac{\partial \mathcal{W}_{F_\alpha}^{\text{neq}}}{\partial I_{F_{2\alpha+2}}^e} I_{F_{2\alpha+2}}^e + 2 \frac{\partial \mathcal{W}_{F_\alpha}^{\text{neq}}}{\partial I_{F_{2\alpha+3}}^e} I_{F_{2\alpha+3}}^e \right. \\ &\quad \left. + \sum_{\beta}^2 \frac{\partial \mathcal{W}_{F_\beta}^{\text{neq}}}{\partial I_{F_{2\beta+3}}^e} \left(\frac{\mathbf{C}_F^{v-1} \mathbf{C} \mathbf{M}_\beta : \mathbf{M}_\alpha \mathbf{C}}{\mathbf{C}_F^v : \mathbf{M}_\beta} + \frac{\mathbf{M}_\beta \mathbf{C} \mathbf{C}_F^{v-1} : \mathbf{C} \mathbf{M}_\alpha}{\mathbf{C}_F^v : \mathbf{M}_\beta} \right) \right), \end{aligned} \quad (4.71)$$

which equals $\boldsymbol{\tau}_{F_\alpha}^{\text{neq}}$.

4.7 Numerical Examples

To demonstrate the capabilities of the anisotropic constitutive models, the N fiber-families model presented in Sec. 4.2.3 and the generalized two fiber-families model presented in Sec. 4.2.4 are applied to examine the viscoelastic behavior of composites with two reinforcing fiber families. For all of the examples, the stress response of the matrix is considered to be nearly incompressible. This is generally a good assumption for biological soft tissues where the matrix material is composed mainly of water and for soft engineering composites with an elastomeric matrix. To model the nearly incompressible behavior of the matrix, the following decoupled representation of the Neo-Hookean free energy density for the matrix is applied in all the simulations,

$$\mathcal{W}_M = \frac{\mu^{\text{eq}}}{2} (\bar{I}_1 - 3) + \frac{\mu^{\text{neq}}}{2} (\bar{I}_{M_1}^e - 3) + \frac{\kappa}{4} (I_3 - \ln I_3 - 1). \quad (4.72)$$

The variables $\bar{I}_1 = I_3^{-\frac{1}{3}} I_1$ and $\bar{I}_{M_1}^e = I_{M_3}^{e-\frac{1}{3}} I_{M_1}^e$ are the first invariant of the deviatoric components of the deformation tensors $\bar{\mathbf{C}} = I_3^{-\frac{1}{3}} \mathbf{C}$ and $\bar{\mathbf{C}}^e = I_{M_3}^{e-\frac{1}{3}} \mathbf{C}^e$ (see [27], [65], and [78] for more details on the volumetric/deviatoric split of \mathbf{F}). The deviatoric part of the matrix stress response is characterized by the short- and long-time shear moduli $\mu_o = \mu^{\text{eq}} + \mu^{\text{neq}}$ and $\mu_\infty = \mu^{\text{eq}}$ while the volumetric part is characterized by the bulk modulus κ . The incompressibility of the matrix material is approximated by specifying $\kappa \gg \mu_o$. The time-dependence of the bulk properties is neglected because of the incompressibility assumption. For simplicity, the shear viscosity η_{M_s} is set to a constant.

For the N fiber-families model presented in Sec. 4.2.3, where the anisotropic part of the free energy density depends only on the fiber stretches, the standard reinforcing model is applied for \mathcal{W}_F in eq. (4.18):

$$\mathcal{W}_F = \sum_{\alpha=1}^2 \frac{1}{2} k^{\text{eq}} (I_{\alpha+3} - 1)^2 + \sum_{\alpha=1}^2 \frac{1}{2} k^{\text{neq}} (I_{F_{\alpha+3}}^e - 1)^2. \quad (4.73)$$

Recall that for the N fiber-families model, $I_{\alpha+3} = \mathbf{C} : \mathbf{M}_\alpha$ and $I_{F_{\alpha+3}}^e = \mathbf{C}_F^e : \widetilde{\mathbf{M}}_\alpha$. The two fiber-families are chosen to have the same mechanical properties k^{eq} and k^{neq} in eq. (4.73). This model is referred to as Model I in the remainder of the section. For simplicity, the characteristic fiber viscosity is chosen to be a constant parameter.

For the two fiber-families model presented in Sec. 4.2.4, the following higher order reinforcing model examined by [59] is chosen for \mathcal{W}_F .

$$\mathcal{W}_F = \sum_{\alpha=1}^2 \frac{1}{2} k^{\text{eq}} (I_{2\alpha+3} - 1)^2 + \sum_{\alpha=1}^2 \frac{1}{2} k^{\text{neq}} (I_{F_{2\alpha+3}}^e - 1)^2. \quad (4.74)$$

As for Model I, it has been assumed that the two fiber-families exhibit the same material properties, and a constant η_F is chosen for the viscosity of both fiber families.

Table 4.5. Parameters for Models I and II for uniaxial creep of orthotropic fiber-reinforced composite.

cases	$k^{\text{neq}}/k^{\text{eq}}$	$\mu^{\text{eq}}/k^{\text{eq}}$	$\mu^{\text{neq}}/k^{\text{eq}}$	κ/k^{eq}	$\xi_{\text{F}} (s)$	$\xi_{\text{M}} (s)$
1	0.0	0.005	0.005	50	–	1
2	1.0	0.02	0.0	100	1	–
3	1.0	0.01	0.01	100	1	1

This model is referred to as Model II in the remainder of the section. The linearization of the two models in the limit of small-strains is presented in Section 4.4.

To avoid volumetric locking effects in modeling the nearly incompressible response of the matrix, the mixed element formulation developed by [78] is employed for the finite-element simulations. Specifically, eight-node hexahedron Q1P0 elements are used for all the simulations. In addition, an incremental Newton-Raphson solution algorithm is used to solve the quasistatic boundary value problem.

4.7.1 Uniaxial tensile creep response

Models I and II, were applied to study the uniaxial creep response of a composite with two orthogonal fiber families. Three cases were considered for each model to examine the effects of fiber and matrix viscoelasticity on the time-dependent response of the composite. Case 1 was characterized by a viscoelastic matrix and an elastic fiber phase while case 2 was characterized by an elastic matrix and viscoelastic fiber phase. Both phases exhibited viscoelastic behavior for case 3. The model parameters for the three cases, given in Table 4.5, were chosen to give the same ratio $\mu_o/k_o = 0.01$ and characteristic relaxation time $\xi^* = \xi_{\text{M}} = \xi_{\text{F}} = 1\text{s}$ for the matrix and fiber phases (see Section 4.4 for the derivation of ξ_{M} and ξ_{F}). As a result, Model I possessed a more compliant creep response than Model II, but the three cases of each model had same instantaneous behavior at $t = 0$. The two fiber-families were oriented in the $\mathbf{P}_1 = \mathbf{e}_1$ and $\mathbf{P}_2 = \mathbf{e}_2$ directions. The finite-element geometry employed for the uniaxial creep simulations was a cube discretized by eight Q1P0 hexahedron elements of size $h = 1\text{mm}$. The displacements of three faces of the cube were constrained as, $u_1(x_1 = 0) = 0, u_2(x_2 = 0)$ and $u_3(x_3 = 0)$, to remove rigid body deformation modes. Loading was provided by applying a constant normal traction $t_2 = \sigma_{22} = 0.5k_o$ to the top face of the cube $x_2 = 2h$ at time $t = 0$. The loading resulted in an instantaneous strain $\varepsilon_{22}(t = 0) = \frac{u_2}{2h} = 0.098$ for Model I and $\varepsilon_{22}(t = 0) = 0.027$ for Model II. As expected, Model I exhibited a more compliant creep response for the same fiber stiffness k_o . Throughout all the simulations, the change in the jacobian $J = \det[\mathbf{F}]$ remained below 0.01% which demonstrated that a sufficiently high value of the matrix bulk modulus can be used to model the nearly incompressible response of the composite.

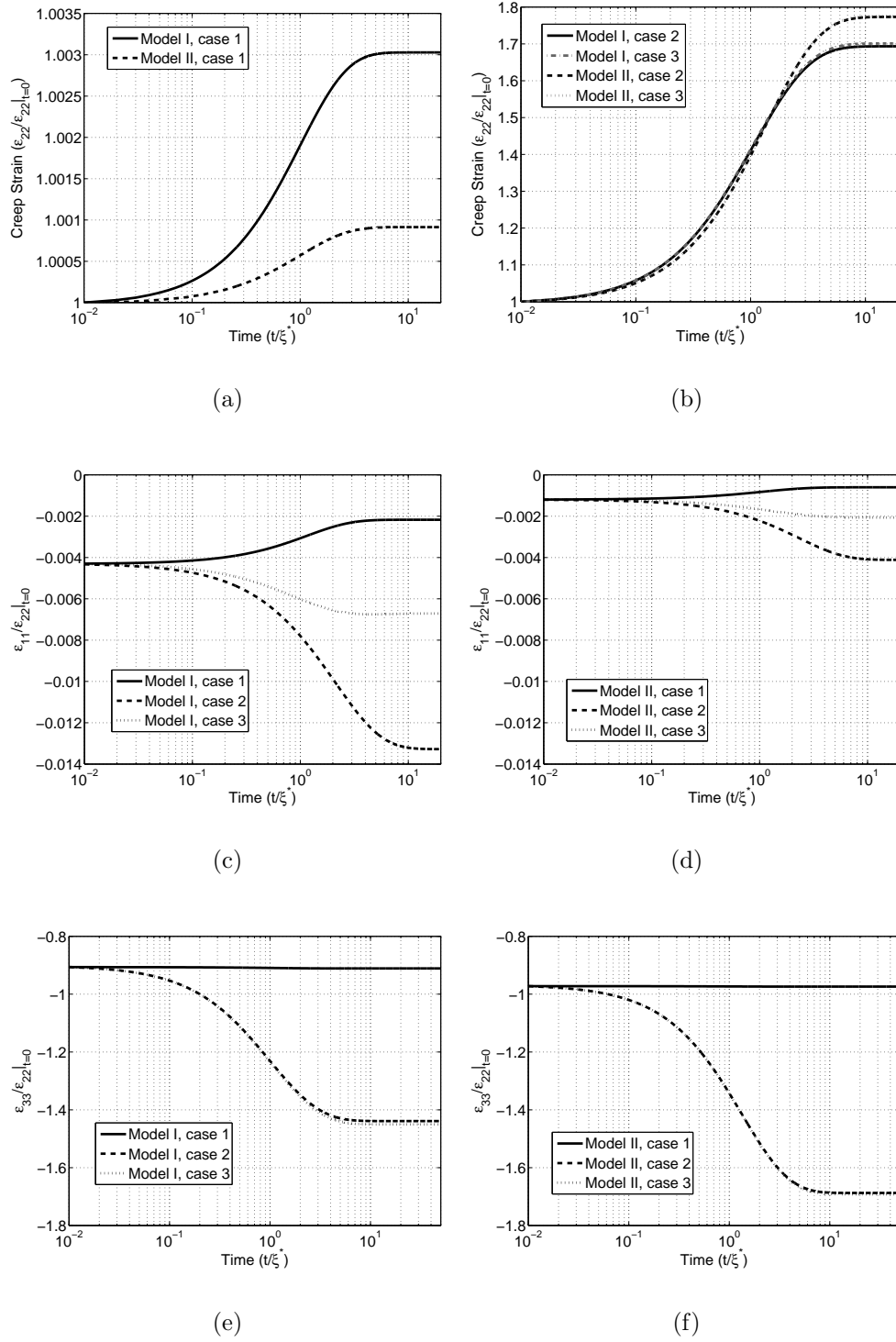


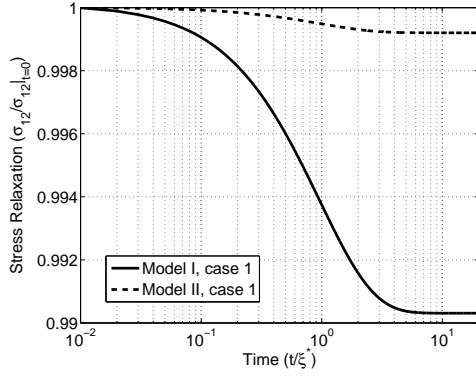
Figure 4.2. Uniaxial tensile creep: (a) creep strain in the loading direction ε_{22} for case 1 of both models, (b) ε_{22} for cases 2 and 3 of both models, (c) ε_{11} for all cases of Model I, (d) ε_{11} for all cases of Model II, (e) ε_{33} for all cases of Model I, and (f) ε_{33} for all cases of Model II.

The time evolution of the creep strain ε_{22} and the out-of-plane strains ε_{11} and ε_{33} for the three cases of Models I and II are plotted in Figures 4.2. The strains were normalized by the instantaneous creep strain $\varepsilon_{22}(t=0)$ while time was normalized by the characteristic relaxation time ξ^* . Because the fiber phase was significantly stiffer than the matrix phase, a more pronounced creep response was observed for cases 2 and 3 than case 1 where only the matrix was allowed to exhibit time-dependent behavior. The creep response of cases 2 and 3 plotted in Fig. 4.2(b) were nearly identical which confirmed that the time-dependent behavior of the matrix had little effect on the creep response of the composite.

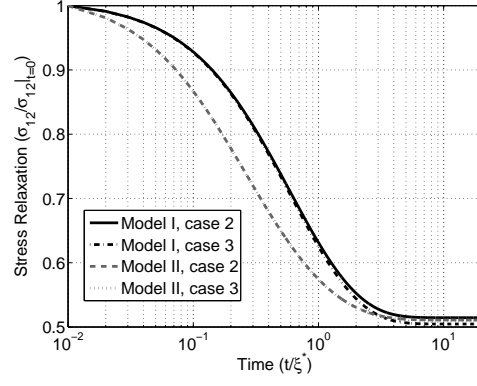
The Poisson's contraction in the plane of the fiber families, ε_{11} , plotted in Fig. 4.2(c)-4.2(d), were small relative to ε_{22} for all three cases. However, the time-dependence of ε_{11} differed dramatically between the cases. The magnitude of ε_{11} decreased with time for case 1 but increased with time for cases 2 and 3. The out of the plane strain, ε_{33} plotted in Fig. 4.2(e) and Fig. 4.2(f), became increasingly negative with time for all cases, but its magnitude was significantly larger for cases 2 and 3, where the fibers could creep, than case 1.

4.7.2 Simple shear relaxation response

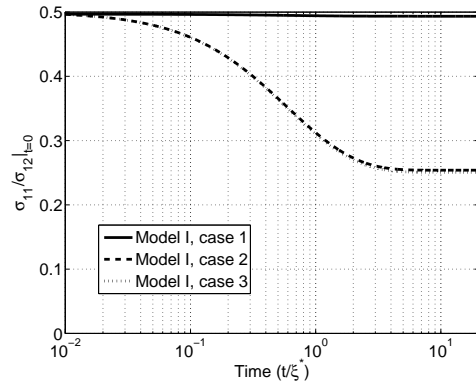
The three cases of Models I and II were applied to study the stress relaxation response under simple shear. Recall that the model parameters for the three cases were given in Table 4.5. The orientation of the two fiber-families was set to $\mathbf{P}_1 = \mathbf{e}_1$ and $\mathbf{P}_2 = \mathbf{e}_2$ and the same finite-element geometry employed for the creep problem was used for the simple shear simulations. The displacement components u_3 and u_2 of the cube were held fixed while $u_1(x_2) = 0.25x_2$ was applied to all the nodes of the finite-element geometry at time $t = 0$ to produce a uniform engineering shear strain $\gamma_{12} = 0.25$. Figure 4.3 plots the time history of the stress relaxation response. The stresses were normalized by the short-time shear stress, $\sigma_{12}(0) = 0.25k_o$ for Model I and $\sigma_{12}(0) = 3.1k_o$ for the significantly stiffer Model II, while the time was normalized by the characteristic relaxation time $\xi^* = 1$ s of each case. As observed in the creep simulations, the stress relaxation obtained for case 1, where only the fiber phase was elastic, was negligible compared to that computed for cases 2 and 3. The ratio of the long-time to short-time stress response of case 1 was $\sigma_{12}(\infty)/\sigma_{12}(0) = 0.99$ while $\sigma_{12}(\infty)/\sigma_{12}(0) = 0.5$ for cases 2 and 3. The same was observed for the normal stress response σ_{11} in the plane of the fiber families. However, the out-of-plane relaxation response was dominated by the time-dependent behavior of the matrix. As shown in Figs. 4.3(e) and 4.3(f), stress relaxation was observed for σ_{33} in cases 1 and 3 but not in case 2 where the matrix was elastic. The results of both the creep and relaxation studies indicated that the viscoelastic behavior of the matrix can be neglected in modeling the in-plane time-dependent behavior of fiber-reinforced composite when the fiber phase also exhibits viscoelastic behavior and is significantly stiffer than the matrix phase.



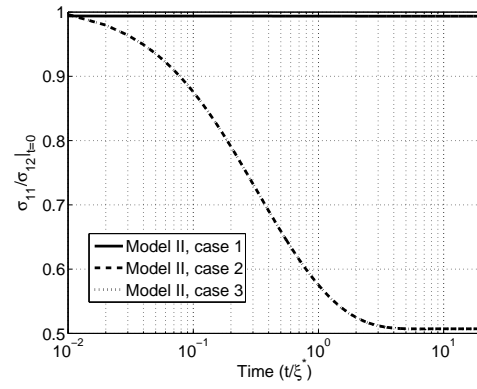
(a)



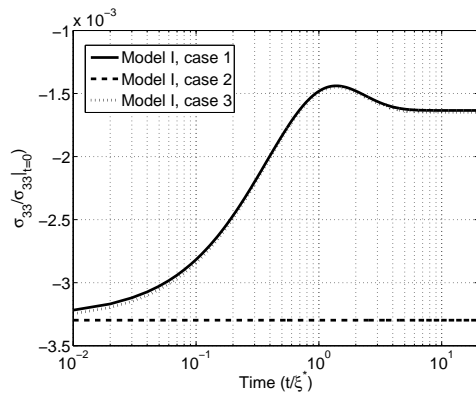
(b)



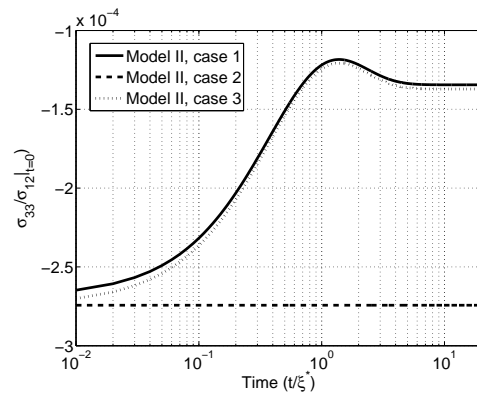
(c)



(d)



(e)



(f)

Figure 4.3. Simple shear relaxation: (a) shear stress in the loading direction σ_{12} for case 1 of both models, (b) σ_{12} for cases 2 and 3 of both models, (c) σ_{11} for all cases of Model I, (d) σ_{11} for all cases of Model II, (e) σ_{33} for all cases of Model I, (f) σ_{33} for all cases of Model II.

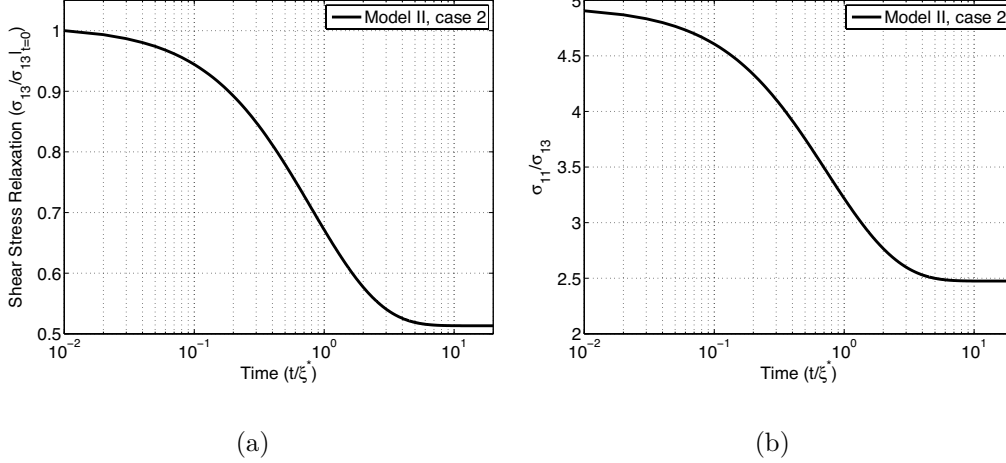


Figure 4.4. Stress relaxation for Model II subject to simple shear out of the plane of the fiber families: (a) shear stress σ_{13} along the loading direction (b) normal stress σ_{11} along the loading direction.

To further compare the reinforcing effects provided by the two models in shear, the relaxation response of case 2 was examined for an applied uniform shear strain $\gamma_{13} = 0.25$. Recall that case 2 was characterized by a viscoelastic fiber phase and an elastic matrix phase. The shear strain was applied by specifying $u_2 = u_3 = 0$ and $u_1(x_3) = 0.25x_3$ at all the nodes of the finite-element model. The stress response of Model I to γ_{13} was completely independent of time. The fiber families of Model I remained unstretched in this loading geometry, and the stress response of the composite was determined solely by the elastic matrix. In contrast, the fiber families provided a reinforcing effect in Model II because the applied deformation induced a stretch in the higher order invariant, $I_5 = 1 + \gamma_{13}$. This enabled the relaxation of the stress response σ_{13} and σ_{11} shown in Fig. 4.4.

4.7.3 Inflation of composite tube

Model I was applied to simulate the inflation of a laminated thick-wall tube. A schematic of the composite tube is illustrated in Fig. 4.5. The thick-wall tube consisted of two laminates, each composed of two helically wound fiber families embedded in an isotropic matrix. The orientation of fiber families were symmetric with respect to the tube axis. The geometry of the composite tube was chosen to represent the dimensions and fiber arrangement of the adventitia and media layers of a human elastic artery as provided by [40]. However, the material parameters listed in Table 4.5 for case 3 were applied to model both laminates. A quarter model of the tube was con-

structured for the finite-element simulation and discretized using Q1P0 mixed elements of length $L/12$ in the axial direction and $\pi/52$ rads in the circumferential direction. For each layer, the size of the elements in the radial direction was biased towards the center to capture the high stress gradients near the inner surface of each layers. In total, eight elements were used to discretize the radial thickness of the inner layer and four elements were used for the outer layer. The vertical displacement at the ends of the tube was constrained as $u_3(z = -L/2) = u_3(z = L/2) = 0$ to preclude axial stretching, and $u_3(x_2 = 0) = 0$ and $u_1(x_1 = 0) = 0$ were set to preserve the radial symmetry of the quarter tube model. An internal pressure, $p(t)$, was applied to the inner surface of the tube, while the outer surface of the tube was left traction free. The applied internal pressure p was ramped quickly from zero at $t = 0$ to $p = 0.1k_o$ at $t = 0.1\xi^*$, then cycled sinusoidally at a frequency of $\omega = 2\pi/\xi^* = 1\text{Hz}$ between $0 \leq p \leq 0.05k_o$.

The applied internal pressure is plotted in Figure 4.6 as a function of the internal volume change calculated as r_i^2/R_i^2 , where r_i and R_i were the deformed and undeformed inner radius of the tube. For the applied frequency $\omega = 1\text{Hz}$, steady-state was achieved in the pressure-volume response after one loading period. The steady-state pressure-volume curve formed an elliptical shape characteristic of the hysteresis curve of viscoelastic materials. The viscous dissipation can be computed by integrating the area underneath the steady-state pressure-volume curve for one cycle. The radial and hoop stress of the laminate cylinder are plotted in Fig. 4.6(b) as a function of the radial distance. The compressive radial stress decreased smoothly from the applied pressure $-p$ at the internal surface $R/R_i = 1$ to zero at the traction free external surface $R/R_i = 1.43$. Meanwhile, the tensile hoop stress decreased gradually from $-3.8 \leq \sigma_{\theta\theta}/p \leq -3.0$ for $1.0 \leq R/R_i \leq 1.21$, then more dramatically from $-3.0 \leq \sigma_{\theta\theta}/p \leq -0.93$ for $1.0 \leq R/R_i \leq 1.32$ before slowly decreasing to $-\sigma_{\theta\theta}/p = -0.85$ at the external surface of the cylinder, $R/R_i = 1.43$. The sharp decrease in the hoop stress occurred near the interface of the two laminates located at $r/R_i = 1.28$. The hoop stress was significantly higher in the inner laminate because the $\pm 10^\circ$ fiber winding angles of the inner laminate provided a stiffer hoop reinforcement than the $\pm 40^\circ$ fiber winding of the outer layer.

4.8 Discussion

A general constitutive framework has been presented for modeling the finite-deformation viscoelastic behavior of soft fiber-reinforced composites. The essential and distinguishing features of the model includes:

- The parallel decomposition of the deformation gradient and additive split of the free energy density into matrix and fiber components and then further into elastic/equilibrium and viscous/nonequilibrium components. This allows separate stress relations and viscous flow rules to be specified for either phases.

- The mapping of the structure tensor to the intermediate configuration with the viscous deformation gradient of the fiber phase which permits the fiber arrangement to be specified only in reference configuration.
- The definition of the viscous and elastic fiber stretch from the viscous and total deformation gradient tensors of the fiber phase and the structure tensors.
- The formulation of one-dimensional viscous flow rules for the individual fiber families and the homogenization of the individual flow rules for the three-dimensional .

The main result of this new approach is that it introduces a description of the fiber arrangement in the effective viscous properties of the fiber phase in the same manner that the analogous homogenization scheme for the free energy density incorporates a description of the fiber arrangement in the effective elastic properties.

An attractive feature of the approach to anisotropic viscoelasticity presented here is that key model parameters can be related to the material properties (i.e., moduli and viscosities) of the constituent phases and to the arrangement of the fiber families. Consequently, the model parameters can be determined, when possible, from independent characterizations of the viscoelastic properties of the matrix and fiber materials and of the composite morphology. The formulation of the model also provides for a simple and efficient numerical implementation in a finite-element framework. The constitutive relations depend only on the externally applied stretch and internal stretches, which are evaluated for the matrix and fiber phases in a finite-element framework at the integration point level using a first-order accurate, stable Newton solution algorithm.

Finally, the approach can be extended to model anisotropic elasto-viscoplasticity for fiber-reinforced composites. An analogous elasto-viscoplastic model would include the formulation for the individual fiber families of a yield condition using the fiber stress, a plastic flow rule for the plastic fiber stretch, and the Kuhn-Tucker conditions involving the plastic fiber stretch and the fiber yield condition. These features allow the constitutive models presented here to serve as an efficient and predictive simulation tool for the design and analysis of a class of materials that is important in both engineering applications and in biomechanics. In the area of biomechanics, the model is applied currently to study the viscoelastic behavior of the cornea [62]. In addition, its application to modeling the viscoelastic behavior of blood vessels is being explored.

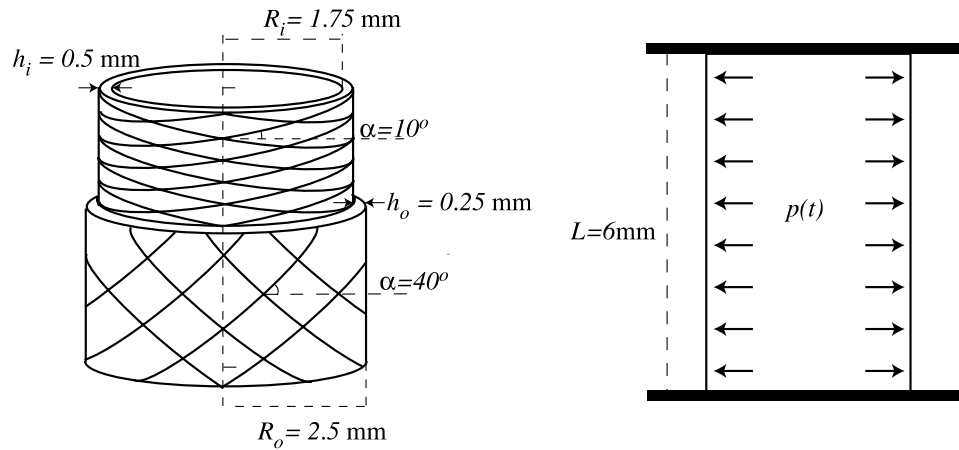


Figure 4.5. Schematic of thick-wall cylinder composed of two laminates of different fiber windings. The tube is inflated by applying a cyclic internal pressure while holding the ends fixed.

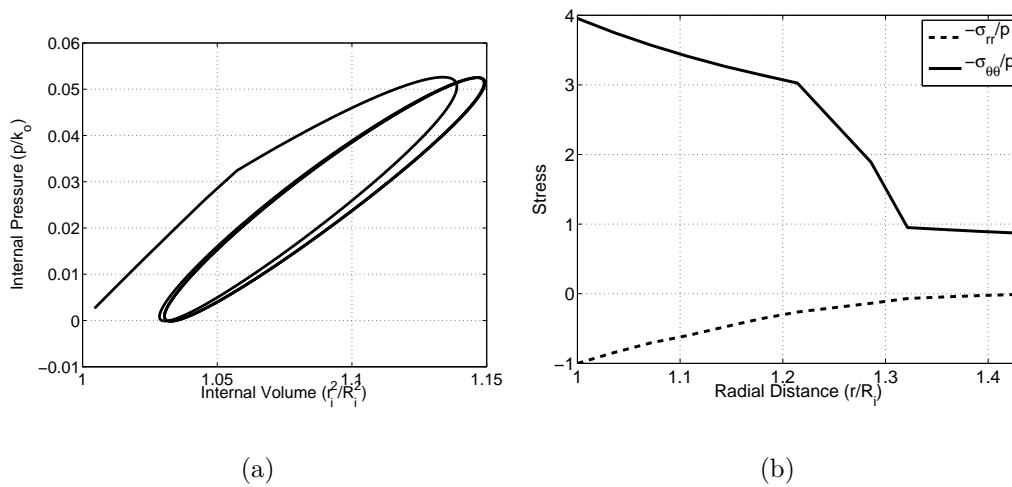


Figure 4.6. Cyclic inflation of laminate cylinder: (a) internal pressure vs. volume change, (b) the radial and hoop stresses, σ_{rr} and $\sigma_{\theta\theta}$, as a function of radial distance.

Chapter 5

Cornea Deformation Under Physiological Inflation Conditions

The time dependent response of bovine corneas was characterized using *in vitro* inflation experiments and compared to previously developed models. Using a fixture that conformed to the limbal-sclera junction and full field image correlation, three regimens were performed on intact corneas : (a) 0 to 8 *kPa*, (b) 0 to 32 *kPa* and (c) 3.6 to 8 *kPa*. The last test was intended to mimic nominal intraocular pressure (IOP) to the pressure observed in high glaucoma and was done on nine replicates to provide meaningful statistics and reduce noise in the displacements recovered via image correlation. From nominal IOP to high glaucoma, we observed minimal hysteresis, consistent with the conception that the cornea behaves essentially elastically at and near its normal range. We also observed that the structure of the cornea is such that it preserves the lens shape of the central cornea, leaving the periphery to accommodate most of the bulging under increased globe pressure.

5.1 Introduction

While previous work both at Sandia and in the literature [15, 64, 3, 35, 80, 45, 89, 86], has primarily involved tensile tests of excised corneal strips, both the excision process and the uniaxial loading mode may produce results that are not physiologically meaningful. Specifically, the excision process severs off-axis collagen fibrils, and the subsequent tensile loading mode will only directly load the on-axis fibrils. Moreover, the tensile loading mode, which is different from the natural biaxial mode associated with changes in intraocular pressure, may recruit fibers in a manner that is not physiological. The tensile testing mode pre-deforms the cornea from its naturally curved shape into a flat tensile bar. Moreover, the tensile test method requires aggressive clamping of the very compliant corneal strip to prevent slippage during testing, resulting in uncharacterized and presumably large corneal distortions/forces near the edge of the tensile strip. These issues with corneal tensile strip testing have been noted in the past (i.e. [17, 25]); specifically, our prior work [15] has suggested that the non-physiological loading conditions associated with the tensile test result in the need for pre-conditioning cycles to evolve the tissue into a repeatable reference state

for viscoelastic testing. Without pre-conditioning cycles, a monotonic tensile test is a combination of viscoelastic deformation and structural rearrangement, leading to results that are not fully recoverable.

The purpose of the present work is to evaluate the time-dependent properties of cornea tissue in a condition that is as physiologically-relevant as possible without resorting to costly and difficult *in vivo* characterization. To further enhance the value of this characterization, a non-contact 3-dimensional displacement mapping tool has been employed to image the entire deformation field across the entire cornea during pressurization. This tool permits examination of the isotropy and homogeneity of deformation in the cornea.

5.2 Method

Materials. Untreated bovine ocular globes from beef cattle 18-24 months in age were obtained from a medical supplier (Animal Technologies Inc., Tyler, Texas) within 24 hours after slaughter. The globes were shipped as left-right pairs in polymer sample bags on ice to minimize tissue evolution. Upon arrival, the corneas were each inspected for blemishes and the major and minor diameters, along the nasal-temporal and inferior-superior axes respectively, were measured. Typically, out of a shipment of 12 globes, only the best 2-4 were chosen for testing: without blemishes and nearest to average size.

Fixturing Scheme. Many prior works [44, 34] have inflated the entire intact globe to determine pressure-displacement response. However, in such a case, the deformation of the cornea is convoluted with the deformation of the supporting sclera. To separate cornea deformation from scleral deformation while minimizing perturbations to the cornea itself, a complex fixture was developed. The 3-dimensional profile of the anterior portion of a typical globe, including all of the cornea and several millimeters of the sclera was quantitatively captured using a two-camera single-frame digital image correlation routine (*VicSNAP* and *Vic3D*, Correlated Solutions, Inc.). The shape of this anterior globe was imported into solid modeling software (*SolidWorks*, SolidWorks Corp.) to capture the contour of the sclera and most importantly, the three dimensional shape of the corneo-scleral junction at the limbus. This corneo-scleral junction is not simply a two-dimensional ovoid, but rather a three-dimensional saddle-shape: the nasal and temporal edges of the junction being deeper, i.e. more distant from the apex along the optical axis, than the inferior and posterior edges. This complex saddle-shaped ovoid, directly imported into the solid modeling software was used to define the contour of a support ring where the ring, shown in Figure 5.1 only makes contact with the scleral side of the corneo-scleral junction. The support ring was manufactured in transparent lexan directly from the solid model using computer-numeric controlled machining. To mate the cornea to the scleral support ring, the near-cornea sclera of each intact globe was prepared by removing loose epi-

dermal layers and then lightly roughening the remaining tough core. A thin coating of cyanoacrylate adhesive was applied to the scleral contour of the ring, and the aligned globe was manually held against the ring until a structurally-stiff, liquid-impermeable seal was formed between the sclera and the lexan ring. Later testing revealed that this fixed-edge boundary condition was capable of holding pressures beyond 50 kPa , i.e. well beyond the maximum test pressures (typically 8 kPa). With the ring in place, all tissue posterior to the ring, including the posterior globe and the internal tissues (vitreous, lens, etc.), were removed leaving only the cornea mounted to the fixture.

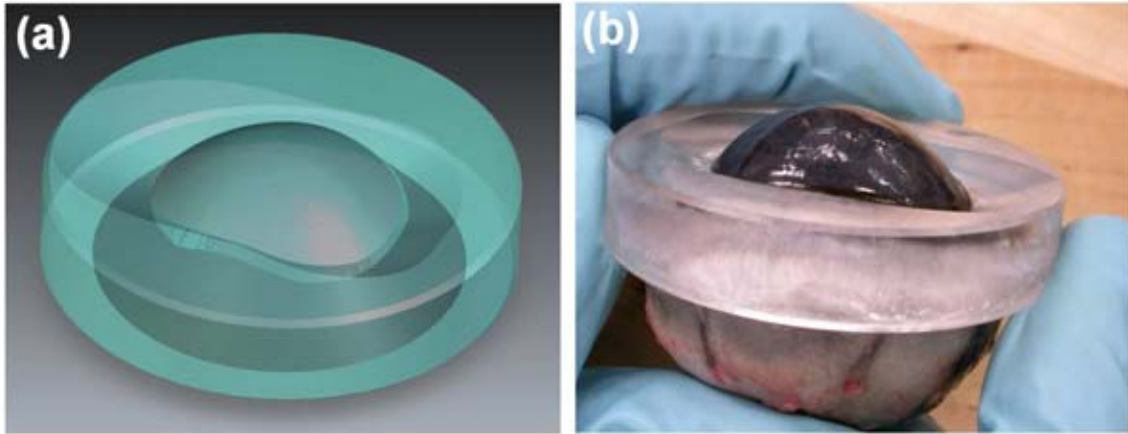


Figure 5.1. (a) Solid model of the cornea adapter ring interfacing with the saddle-shaped corneo-scleral junction. (b) The bovine globe being affixed to the adapter ring prior to removal of the posterior sclera and internal tissues

Controlled Pressurization Scheme and Loading Regimen. The cornea and support ring were bolted to the open end of a custom made stainless steel pressurization chamber, shown in Figure 5.2. A glass lid was loosely placed over the cornea to minimize evaporative tissue shrinkage ($<5\%$ over 1 hr) yet permit optically-based displacement mapping. The chamber provided an inlet at the side for fluid infusion and a $0\text{-}34.5\text{ kPa}$ pressure transducer (Precise Sensors, Inc.). A second inlet the bottom of the chamber provided fiber optic transmission illumination through the cornea for optical deformation mapping, described in more detail in the following section. Fluid infusion and withdrawal to the chamber was provided by a syringe via 3 mm diameter tubing 1 m in length. The syringe was actuated by a MTS Mini Bionix II desktop servohydraulic loadframe. The syringe actuation was controlled by a MTS 458.20 analog controller which permitted analog feedback control of plunger displacement, and hence infused volume, via a MTS $\pm 63.5\text{ mm}$ linear variable differential transformer (LVDT). Most importantly, the controller permits feedback control of pressure via a

MTS 458.11 signal conditioner. A MTS microprofiler was used automate a series of ramps at various rates and hold durations.

Similar to the loading regimen used previously for tensile testing (see previous chapters), cornea specimens were deformed using a series of triangular loading profiles (cycles) connected by relaxation segments at the minimum pressure. A series of preconditioning cycles were applied to the cornea prior to the actual test cycles. In the case of the tensile strip experiments, these preconditioning cycles were necessary to permit tissue rearrangement in response to the non-physiologic tensile loading condition thereby establishing a recoverable reference state. To maintain consistency, similar preconditioning cycles were used for inflation of the intact cornea, although as expected, they had much less impact on the resulting behavior. Following the triangular loading cycles, the cornea was also exposed to a long term hold at constant maximum pressure to observe creep and a long term hold at a constant syringe displacement/constant volume to observe relaxation. The loading regimen is shown schematically in Figure 5.3.

The loading regimen was applied to a set of 9 nominally identical tests on 9 bovine corneas, each with a minimum pressure of 3.6 kPa and a maximum pressure of 8 kPa . The minimum pressure was chosen to be similar to typical bovine intraocular pressures and the maximum pressure was chosen to represent a severe case of acute angle-closure glaucoma. The loading durations for cycles A-D, refer to Figure 5.3, were chosen to span nearly 3 orders of magnitude in pressure-rate and be comparable to the loading durations used for tension testing in the previous study. Corresponding linear ramp pressurization rates were 0.036 , 0.0045 , 0.29 , and 0.036 kPa/s for cycles A-D respectively. The two creep cycles, E and F, were loaded to maximum nearly instantaneously ($\ll 1\text{s}$), and held for an extended period of time to evaluate the characteristic timescales for pressure-controlled creep and volume-controlled relaxation respectively. The total duration of the entire loading regimen from preconditioning through cycle F was less than 1 hour. Preliminary experiments showed that significantly longer durations would have resulted in undesirable tissue evolution.

Beyond the baseline statistical sampling of 9 nominally identical tests, an additional two tests were performed at non-standard minimum and maximum pressures. The pressure range of the first test was from 0.07 kPa to 8 kPa , and the second test was from 0.07 kPa to 32 kPa . These two tests permitted examination of sub-physiologic and super-physiologic conditions, respectively. The linear ramp rates were increased so that the total duration of each cycle was identical to the corresponding standard cycles shown in Figure 5.3 (64 , 514 , 8 , 64 , 420 , and 420 s for cycles A-F respectively).

Deformation Mapping Scheme. Prior inflation studies of ocular globes have almost invariably measured scalar deformation quantities such as globe diameter or cornea apex displacement. Recently developed optical digital image correlation methods permit three-dimensional deformation mapping with high spatial resolution (on the order of microns) and temporal resolution (limited only by camera acquisition rate). The present study utilized a pair of low-noise Marlin F145B2 digital cameras with

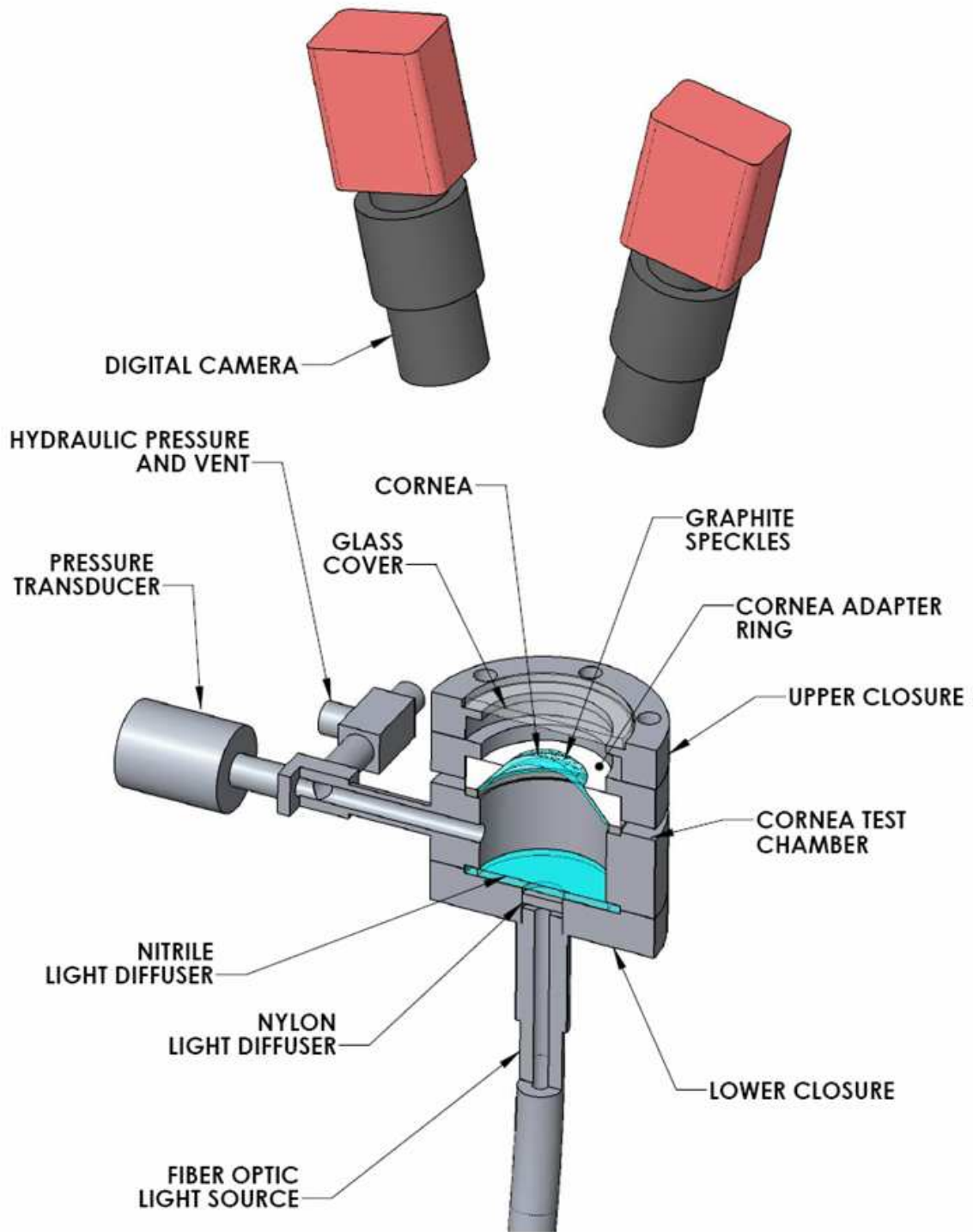


Figure 5.2. Solid model of the key elements in the cornea inflation apparatus.

a 1392 x 1040 pixel charge-coupled device (CCD) capable of continuous frame rates up to 15 fps. Both cameras were tilted ≈ 15 degrees from the optical axis to permit binocular viewing as shown in Figure 5.2. Prior to imaging the cornea specimens, a series of binocular images of a reference-grid pattern were captured using *VicSNAP* software over a wide range of reference-grid inclination angles to permit automated calibration of the camera-specimen orientations and distances using the *Vic3D* DIC software.

Digital image correlation (DIC) requires that the deforming surface has a pattern of dark and light contrasting features that track with the underlying material deformations. This requisite speckle-contrast is typically accomplished in artificial structural materials through the use of dispersed/partial-coverage black spray paint on a white background, surface roughness such as produced by bead blasting [14], or adherent black particles on a light surface. Highly reflective or glossy surfaces perform poorly in DIC because bright reflections from the light source do not track with the material deformations. This is especially problematic in the cornea where surface liquid renders a glossy surface. To circumvent this problem yet keep the tissue well hydrated, a transmission illumination scheme was developed. Diffused lighting from the bottom of the chamber transmitted through the cornea tissue to the cameras above. Graphite powder was sprinkled on the well-moistened surface to provide a benign speckle pattern, as shown in Figure 5.4a. An example of the resulting speckle-pattern contrast images is shown in Figure 5.4b.

In the DIC algorithm, the three-dimensional surface field within a subset of the image is represented by a non-uniform parametric B-spline surface function with unknown coefficients. The surface displacement field is recovered from reference and deformed point cloud image-pairs. The surface function coefficients are optimized iteratively using the Levenberg-Marquardt method to maximize the correlation between the actual and predicted deformed images over the analysis subset. The two camera system provides triangulation to locate the reference and deformed point clouds in three dimensional space. More details regarding the three-dimensional DIC algorithm is provided elsewhere [32]. The correlation function was minimized for a matrix of subsets of the overall region of interest. In the present experiments, the 24×21 mm dimensions of the major and minor cornea axes, corresponded to 810×710 pixels, whereas the individual subsets analyzed by the DIC algorithm were 35×35 pixels each. At this magnification, each pixel corresponded to a real area of 0.030×0.030 mm²; therefore, the subset size was 1×1 mm².

Finite element model of the cornea. The DIC algorithm extracts an initial shape of the original (reference) configuration, as well as deformation fields for each subsequent image-pair. An example of the initial reference shape of a cornea is shown in Figure 5.5. The noise-floor on the displacement profiles could be estimated by collecting a sequence of images of a non-deforming cornea. From this analysis, the empirical resolution was typically found to be better than $5 \mu m$. From the initial surface extracted with DIC and the solid model of fixture, refer to Figure 5.1, together with thickness

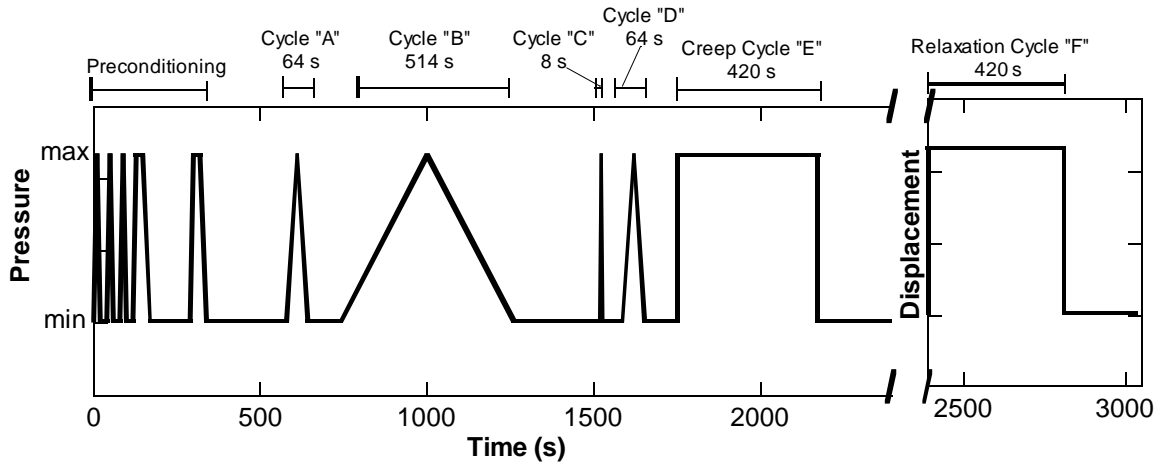


Figure 5.3. The inflation regimen. Note that the final cycle F was performed in displacement control rather than pressure control. This permitted characterization of both creep and relaxation.

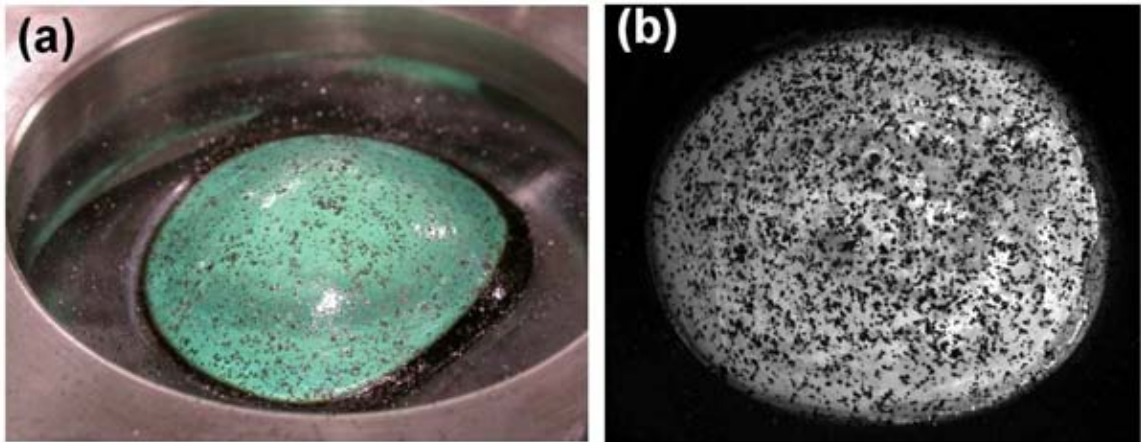


Figure 5.4. (a) Graphite flakes and transmission illumination of the cornea, (b) View of the illuminated speckled cornea from one of the DIC cameras

measurements of the cornea ($1.10 - 1.16 \text{ mm}$), a finite element model of the cornea was constructed. In order to interpolate between the fixture and the outer limit of the DIC data, as well as to reduce noise, the DIC data representing the outer surface of the cornea was fit to an analytical surface, an ellipsoid

$$\left(\frac{x - x_0}{R_{NT}}\right)^2 + \left(\frac{y - y_0}{R_{IS}}\right)^2 + \left(\frac{z - z_0}{R_Z}\right)^2 = 1 . \quad (5.1)$$

The resulting ellipsoid had comparable radii in the lateral directions, $R_{NT} = 17.9829 \text{ mm}$ in the nasal-temporal and $R_{IS} = 17.7144 \text{ mm}$ in the inferior-superior, and slightly larger in the vertical direction $R_Z = 24.193 \text{ mm}$. The fact that the cornea is approximately a prolate spheroid to a high degree of precision, with max error $\approx 0.02 \text{ mm}$, is consistent with its primary function as a lens. This ellipsoid, in turn was intersected with a vertical prism formed by the inner curve of the holder, approximately 28.0 mm in the NT direction and 22.0 mm in the IS direction. Subsequently, this surface was extruded to the approximate (uniform) thickness of the tested corneas, 1.15 mm . The resulting mesh is shown in Figure 5.6.

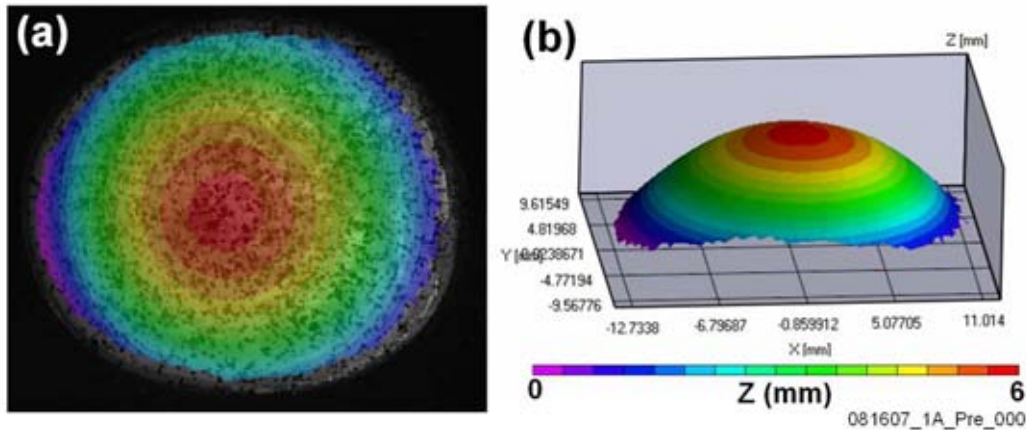


Figure 5.5. (a) DIC determination of the initial shape of a cornea along with (b) corresponding oblique view

5.3 Results

The Displacement Profile. The correlation algorithm provides the shape profile of the initial (reference) image-pair as initial (vertical) Z -heights for a matrix of (lateral) X, Y coordinates within the correlation region of interest. Also, for each of these X, Y coordinates, the DIC algorithm provides $U, V,$ and W displacement components for resolved deformation along the $x, y,$ and z -axes of the camera coordinate system. For

the initial (reference) image, U, V, and W are zero by definition. A typical set of U,V,W deformation values are shown in Figure 5.7. These values are taken for a single cornea at one time-step during the multi-cycle loading regimen. Specifically, these particular DIC maps correspond to the point of maximum pressure, i.e. 8 kPa , during the first test cycle, i.e. cycle A of the 0-8 kPa regimen. The point of maximum pressure occurred 32 s after the start of cycle A, and this DIC map corresponds to the 32nd image-pair captured during cycle A at a frame rate rate of 1 fps. The map for U-displacement shows zero-displacement along the central vertical meridian, i.e. along the inferior-superior axis. The most positive displacements, approaching $+0.3\text{ mm}$, are near the right edge (temporal) and the most negative displacements, approaching -0.3 mm are near the left edge (nasal). The map for V-displacement shows similar gradients, but aligned with the IS axis. These U,V deformation gradients are consistent with an expanding hemispherical shell. The most significant deformations, approaching 1 mm , are shown in the vertical W-displacement map corresponding to deformation along the z axis. As expected, the maximum displacements are at the apex of the cornea and the minimum displacements occur at the periphery. Also, the steepest gradients in W occur in the limbal region: there is more stretch along the z-axis in the peripheral cornea and the central cornea contributes less to the total displacement of the apex. The displacements are not zero at the edge of the DIC map because the transmission DIC method requires a finite analysis window. In the present study, this analysis window prevents characterization of displacements within $\approx 1\text{ mm}$ of the boundary edge.

The Pressure-Dependent Vertical Displacement Field. The present section describes features found at maximum pressure when the total displacements are at or near their maximum. More detail can be found regarding the pressure-dependent evolution of the displacement field as shown in Figure 5.8. At the minimum reference pressure of 0.1 kPa , the cornea is in its reference configuration and there is no U,V or W displacement. At a pressure of 0.7 kPa , which is $<10\%$ of the maximum pressure and $<30\%$ of typical bovine IOP, the cornea appears to have a smoothly-graded nearly symmetric displacement field. At this sub-IOP pressure, the cornea has already deformed quite substantially: the maximum W-displacement in the central cornea of $\approx 0.55\text{ mm}$ is more than half of the final deformation that will be achieved at a maximum pressure of 8 kPa . By a pressure of 2.4 kPa , nearing typical bovine IOP, the shape of the deformation contours has transformed significantly with the deformation contours now more rectangular and stretched along the inferior-superior axis rather than the nasal-temporal axis found at 0.7 kPa . The characteristic contour shapes that emerge at pressures near IOP persist to higher pressures and are still evident at 7.4 kPa . At the pressure of 2.4 kPa , the cornea has already experienced $>80\%$ of its total W-displacement. The displacement profile at a pressure of 6.1 kPa is nearly identical to that at 7.4 kPa . These observations highlight the well-known nonlinear elastic response of the cornea: it is much stiffer at pressures near IOP and above than it is in the fully relaxed state.

Statistically Averaged Displacement Response. The displacement fields for individual

cornea samples do not exhibit regular, symmetric contours indicative of a possible lack of isotropy and/or property homogeneity. Since there was some variability from sample-to-sample, a composite average displacement field for all 9 tests under nominally identical conditions was constructed. The resulting initial configuration and displacement field is shown in Figure 5.9 and Figure 5.10, respectively.

As another way to condense the rich dataset, a scalar W-displacement value was extracted at each timestep of the 9 identical tests. The W-displacement values were taken from the central cornea at the highest point of the original reference configuration. This provides an apex displacement value that can be readily examined as a function of time or pressure. The averaged apex displacement for the 9 identical tests is shown in Figure 5.11. In this figure the three different pressurization rates, i.e. cycles A, B, and C, are compared directly corresponding to pressurization rates of 0.036, 0.0045, and 0.29 kPa/s , respectively. It is interesting to note that there is significantly less sample-to-sample scatter in this inflation data than in preceding tensile experiments (Chapter 2). At all pressure-rates the cornea displays viscoelastic hysteresis, but only a small degree of non-linearity compared to the tensile results. This important feature will be analyzed in more detail in the Discussion section.

Since cycles A and D are nominally identical, both at a ramp rate of 0.036 kPa/s , one can assess the repeatability of the tests. Average apex displacement is plotted as a function of pressure for both of these cycles in Figure 5.12. As intended, the two cycles result in nearly identical behavior, well beyond statistical distinguishability. This suggests that the cornea loading condition returns to a well-defined reference state for each of the cycles, and that any possible time-dependent or cycle-dependent evolution of the material does not affect the resulting mechanical response.

Apex displacement can also be examined as a function of time. This is especially interesting for the constant-pressure creep and constant-volume relaxation cycles, E and F. The average response for these two loading cycles are shown in Figure 5.13. The creep behavior at a constant pressure of 8 kPa quickly reaches a steady-state creep rate on the linear timescale. The creep-rate does not diminish with increasing time. On a logarithmic timescale, the cornea creep rate is growing exponentially, similar to the tensile creep curves for the higher tensile stresses of 350 and 500 kPa shown in Figure 2.5, which suggests activation of multiple creep elements at different timescales [62]. The pressure and apex displacement evolution at constant volume shows expected relaxation of the pressure. Also, as expected, the apex displacement continues to creep since the pressure continues to be well above the rest-state, i.e. 3.6 kPa .

Local Deformation: Central Cornea and Limbus. The ability to extract local displacement vectors allows the evaluation of spatially disparate response. To compare the deformation of the central cornea to deformation around the limbal periphery, displacement values were extracted from positions midway between the corneo-scleral junction and the apex of the cornea, along each of the four directions: nasal, temporal, inferior, and superior. These mid-peripheral displacements were compared directly

to the apex displacement for one specific loading cycle in Figure 5.14. While the pressure-displacement profile for a single specimen is not as smooth as the averaged response, nevertheless a specific trend is obvious: The displacement values at the mid-periphery points account for $\approx 90\%$ of the displacement that occurs at the apex. In other words, the central cornea largely retains its shape during deformation. As a corollary, the pressure-driven deformation is largely accommodated in the limbus of the cornea.

The Response of the Cornea over a Wider Pressure Range. While the preceding results correspond to pressures in the range of 3.6-8 *kPa*, i.e. within the range of physiologically plausible pressures experienced by the bovine species, inflation experiments were also performed over a much wider pressure range from 0.7-32 *kPa*. From these results, a few key cycles were plotted in Figure 5.15. Cycles A and B exhibit a dramatically nonlinear or J-shaped pressure-displacement response. It is interesting to note that the knee in the response is located in the vicinity of ≈ 2 *kPa*, at the onset of typical intraocular pressures. Also note, that this wide-range data supports the notion that the material response is approximately linear over the smaller physiologic range of 3.6-8 *kPa*, as was observed in the previously described experiments. While this wider range is outside the realm of physiologically relevant pressures, it provides a connection to commonly observed J-shaped stress-strain curves found in the literature. The creep response at a constant pressure of 32 *kPa* showed a constant creep rate on a linear timescale, similar to that observed at a creep pressure of 8 *kPa*, here again suggesting the activation of multiple creep mechanisms and different timescales.

5.4 Discussion

Predictability of Inflation Experiments. Using the finite element mesh constructed from DIC data and the constitutive model described in Chapter 3 (and in [62]), the response of the cornea to the programmed pressure excursions was simulated. Figure 5.16 shows how the response of the cornea changes with increasing pressure. Specifically, it clearly demonstrates large deformation and subsequent rapid change in stiffness as the collagen fibrils go from slack to taut. It is also important to note that the higher stress behavior is similar, i.e. after the weak low stress response is removed, in all three types of tests. Since the model described in Chapter 3 was conditioned on tensile data starting from the perceived knee in the response, the parameters obtained from the tension fits should correlated well with the data in the 3.6-8.0 *kPa* regimen. However, referring to Figure 5.17, it is clear that the apex displacement is overpredicted by roughly a factor of 6. There are a number of plausible sources for this error, including: (a) the matrix bulk and shear moduli assumed in the tension work are not representative of the cornea (and the inflation response is relatively more sensitive to these parameters than the tension fit). (b) the intact fibril density was underestimated in the tension experiments due to loading only the

unsevered fibrils, (c) the thickness of the cornea was underestimated by the direct measurements, which would effectively be an underestimation of both the matrix and fibril response. Sensitivity studies show that the inflation response is much more sensitive to the matrix parameters than the tension response. However, the sensitivity to the fibril response in inflation is much greater than the matrix response at the fitted values, as expected. Figure 5.17 shows the response of the same model but fortified with 4x the density of fibrils. The response is quite comparable to the data, but it is hard to attribute all of the error to this cause since it implies loading only 1/4 of the fibrils in the tension experiment.

The full field DIC displacement data also provided a means of comparing the effects of fibril density on deformation. Figure 5.18 shows the assumed fibril density across the cornea, and is adapted from the work [69] on human corneas

$$\begin{aligned} \phi(r, \theta) = & d_{\text{central}} R(r, R_{\text{NT-IS}}, R_{\text{periphery}})(\cos^8 \theta + \sin^8 \theta + 0.451) \\ & + d_{\text{periphery}} R(-r, R_{\text{limbus}}, R_{\text{periphery}})(\sin^8 \theta + 0.720) \end{aligned} \quad (5.2)$$

where (r, θ) are polar coordinates in the NT-IS plane, d_{central} , $d_{\text{periphery}}$ are densities in the central cornea and periphery, and $R(x, x_1, x_2)$ is ramp function that is zero for $x < x_1$, one for $x > x_2$ and linear in between. It is clear from Figure 5.19 that the high density of fibrils in the center cornea provides the stiffness necessary to maintain its shape, while the largest deformations occur at the periphery, much like in Figure 5.10c. However, there is no apparent effects of the anisotropy in fibril density in the central cornea, where most fibrils run in the NT and IS directions. An explanation of this observation is predicated on the fact that the cornea under inflation is nominally in an equibiaxial mode of deformation and, at least at small stretches, the corresponding tangent modulus of the fibril component of the model

$$\mathbb{C} \approx \frac{1}{2\pi} \int_{-\pi}^{\pi} \left. \frac{\partial^2 w_{\text{fibril}}}{\partial(\lambda_{\mathbf{M}}^2)^2} \right|_{\lambda=1} \mathbf{M} \otimes \mathbf{M} \phi d\theta \quad (5.3)$$

is approximately isotropic in plane since the fibril stiffness $\frac{\partial^2 w_{\text{fibril}}}{\partial(\lambda_{\mathbf{M}}^2)^2}$ is independent of θ in the reference configuration (refer to Chapter 3). Figure 5.20 illustrates this point for the deformation of the central cornea only. The deviations from isotropy are on the order of 1/100th the mean displacements.

Application of the Model to Applanation of Cornea during Tonometry. As an application of the geometric and constitutive model to a problem of clinical relevance, a simulation of glaucoma screening via tonometry was constructed. In this common diagnostic test, a flat punch makes contact with the anterior surface of the cornea measuring the internal pressure of the eye indirectly through the cornea. Given the apparent viscous effects that are intrinsic to the cornea, not to mention those associated with other tissues of the globe and the aqueous humor, the conjecture was that the rate of loading would affect the reaction force measured by the instrument. Although the full globe is not modelled nor are the fluid effects, they are mimicked in part in the simulation by a constant volume constraint under the cornea. A cylindrical flat-ended punch was made to approach the cornea at two different loading rates

: 1.0 mm/s and 10.0 mm/s . A typical displacement of anterior surface is shown in Figure 5.21 and Figure 5.22 shows that the reaction force after 10s is different by $< 2\%$. This finding gives confidence to the accuracy of this common test.

5.5 Summary and Conclusions

The present study employed a newly developed cornea inflation and deformation mapping scheme to examine the viscoelastic deformation of the cornea under conditions that closely match *in vivo* conditions. This physiologically-inspired study revealed aspects of cornea deformation that can not be readily gleaned from most *ex situ* experiments. It is clear from these experiments that the structure of the cornea is tailored to operate under positive pressures in the realm of intraocular pressures. At pressures lower than the typical intraocular range, the response of the cornea is much less stiff, almost certainly due to slack collagen fibrils which are perhaps readily buckled in the relatively weak matrix. Another important observation from this study is that the central cornea deforms very little over a physiologic pressure range. This feature is attributed to the circumferential alignment of limbal fibrils which are more compliant along the radial axis than the radially-aligned central cornea fibrils. The result of this radially stiff central cornea is that the central cornea retains its shape and optical power during pressure excursions. Another finding of clinical importance is the cornea's response, over the physiological pressure range and the timescales considered, may be reasonably approximately as linear and relatively free of hysteresis. While an original emphasis of this program was to examine the non-linear viscoelastic response of the cornea, which had been largely ignored in the literature, the inflation results suggest that linearity is a reasonable first-order approximation *under physiologic conditions*. In addition, the under physiologic conditions, the cornea appears to have multiple creep modes active, a phenomenon that was only evident in tensile results at high mean stress or long timescales.

While the present study has emphasized physiologic conditions, the timescale of these experiments was necessarily short, less than 1 hour. The extrapolation of these results to longer term events such as glaucoma and other disease processes is questionable. However, the findings of this work have significant relevance to shorter timescale processes such as corrective surgery and screening tests. Future work to examine longer term physiologically-relevant mechanical evolution in cornea properties will almost certainly require *in vivo* experiments, such as by tonometry.



Figure 5.6. Finite element mesh of the cornea, the red regions are held fixed, to approximate the permeation of the glue into the stiffer scleral tissue, and the inner surface is pressurized

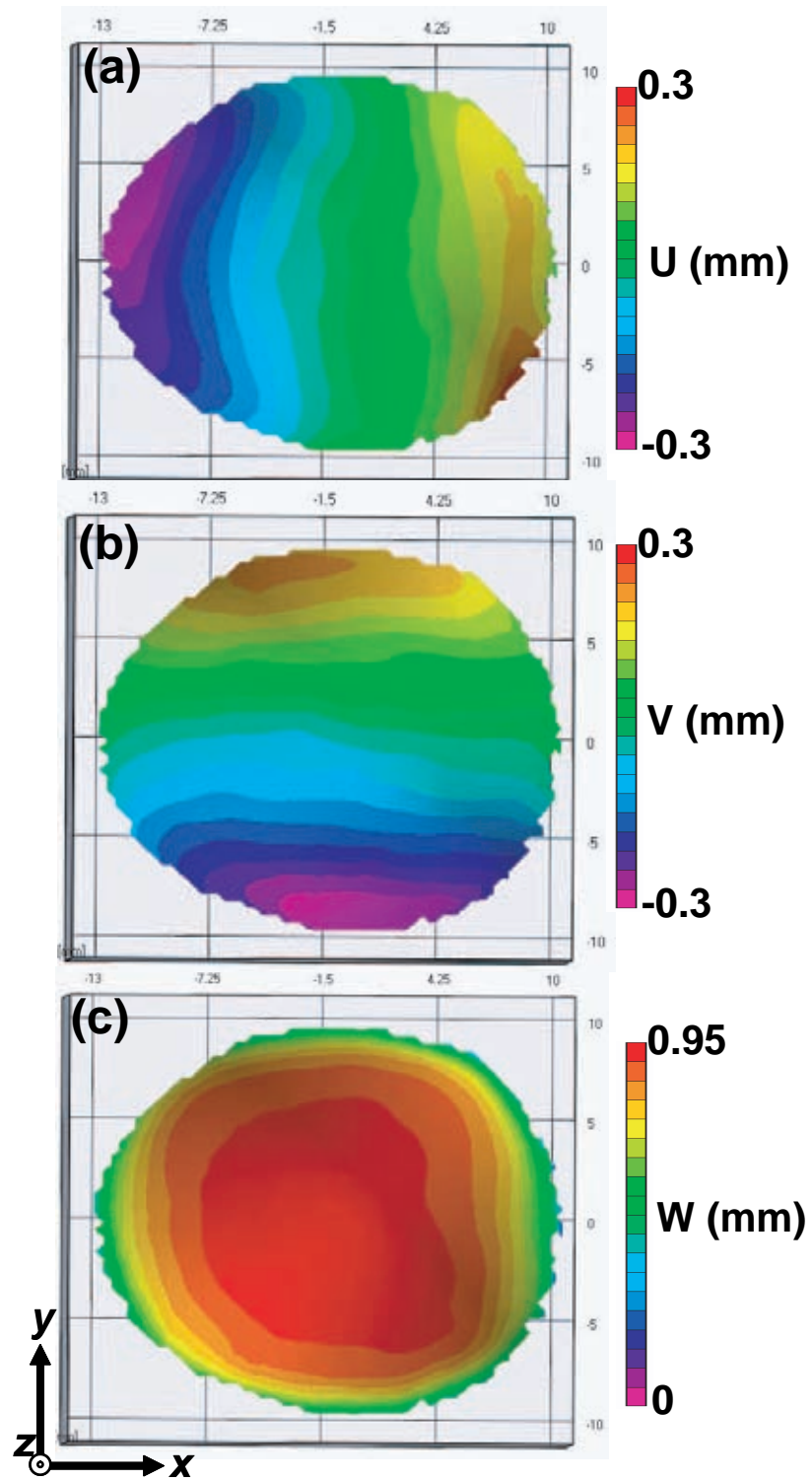


Figure 5.7. Typical displacement components U , V , and W , at a pressure of 8 kPa .

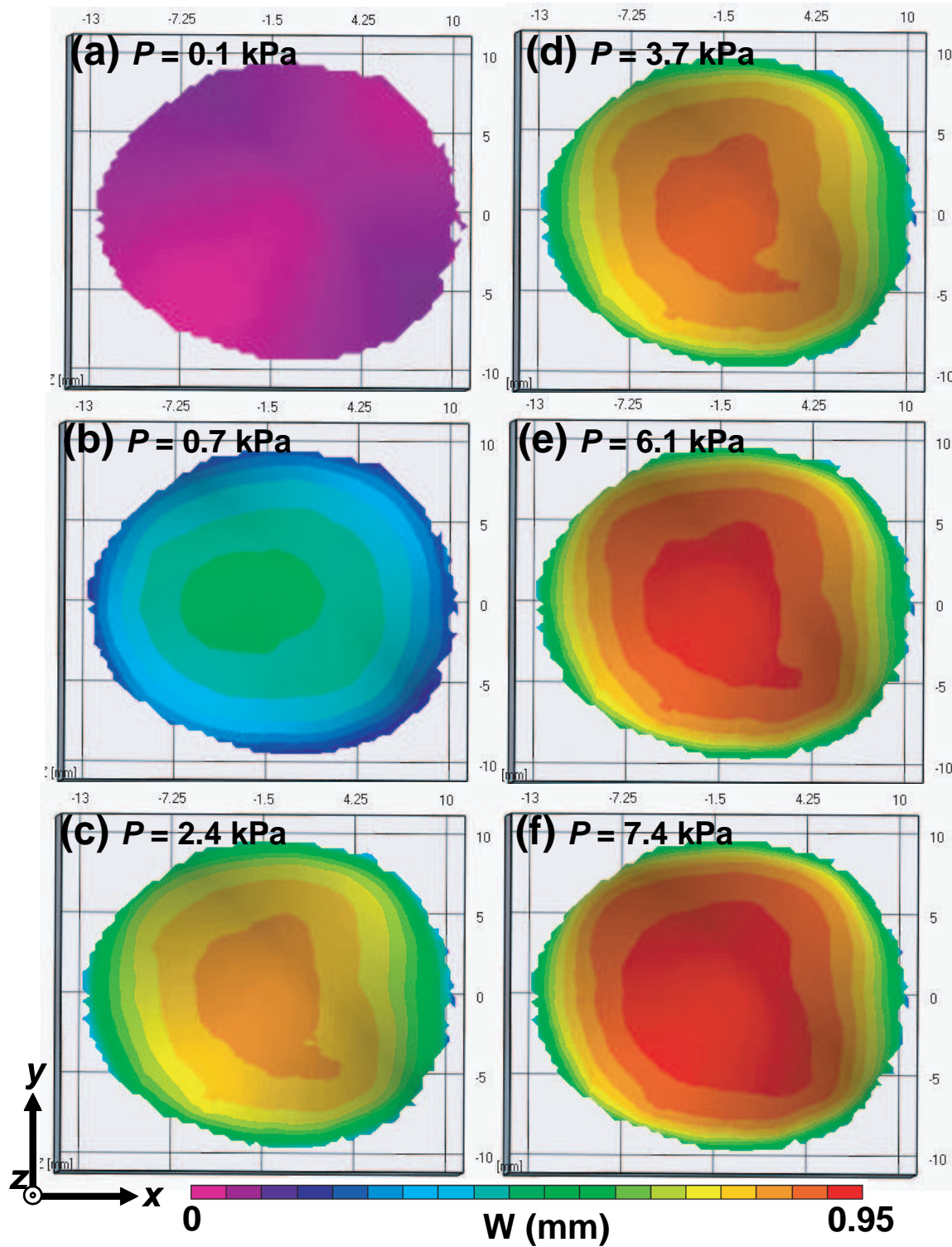


Figure 5.8. Typical out-of-plane displacement, W , at 6 different pressures.

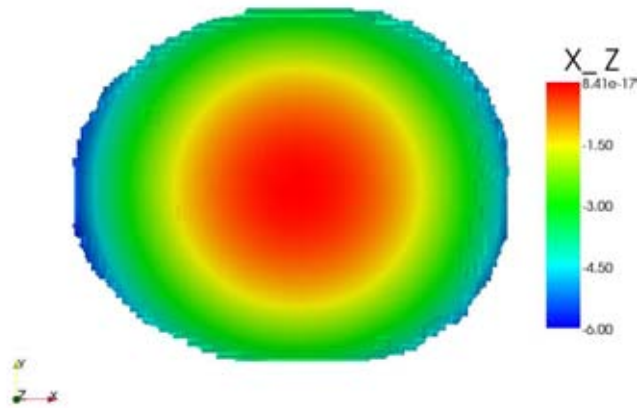


Figure 5.9. Averaged configuration at 3.6 kPa and after preconditioning

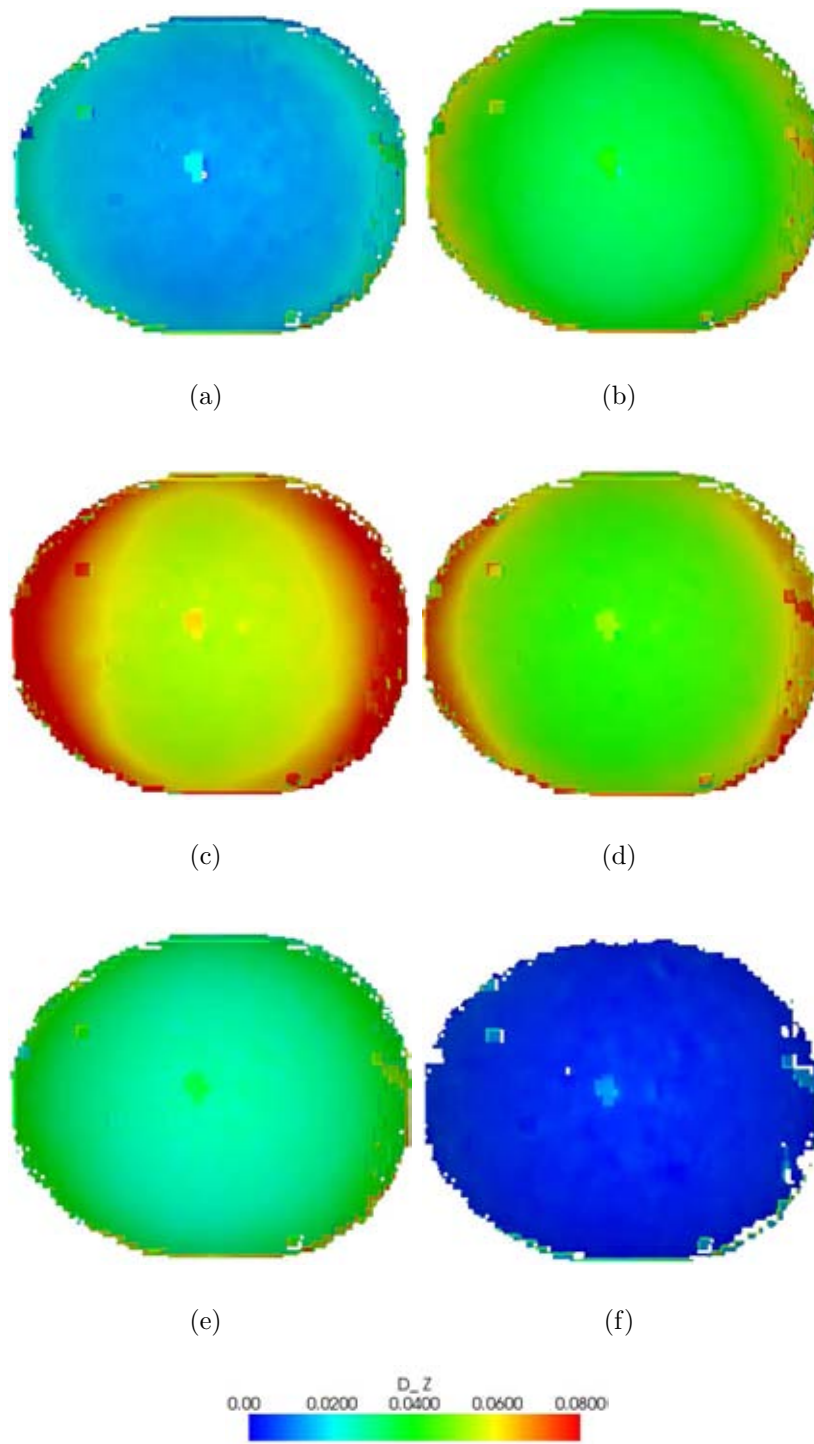


Figure 5.10. Cycle A : averaged displacements at $t=$ (a) $11s$, $5.07 kPa$; (b) $22s$, $6.53 kPa$; (c) $33s$, $8.00 kPa$; (d) $44s$, $6.53 kPa$; (e) $55s$, $5.07 kPa$; (f) $66s$, $3.60 kPa$;

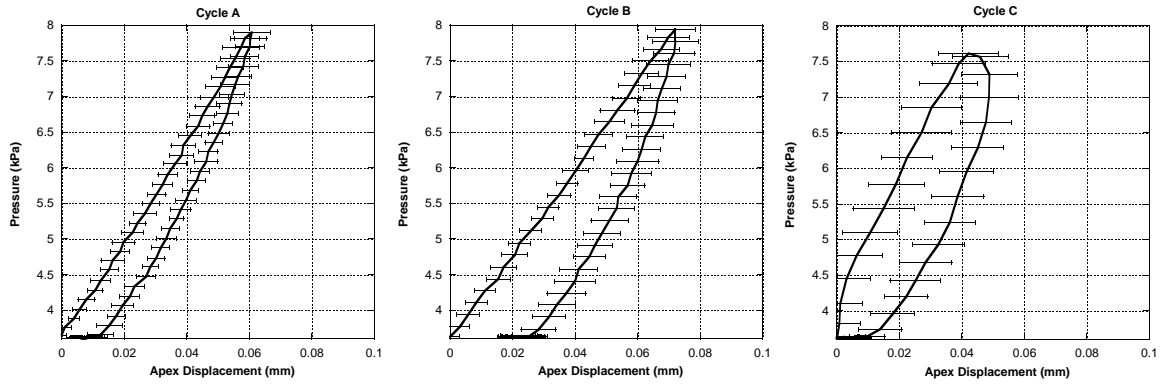


Figure 5.11. The average apex displacement at a function of applied pressure during triangular loading cycles A, B, and C, corresponding to pressurization rates of 0.036, 0.0045, and 0.29 kPa/s , respectively. Error bars indicate 1 standard deviation.

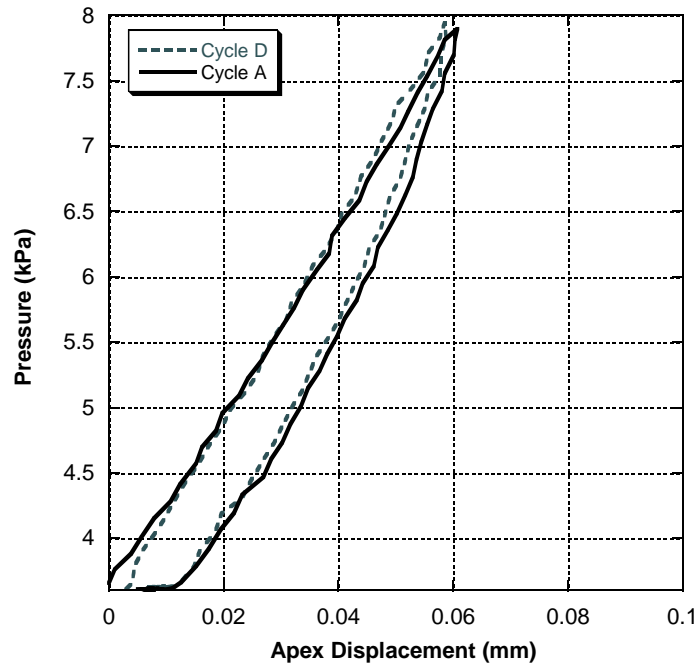


Figure 5.12. A comparison of average apex displacement for two nominally identical cycles in the loading regimen.

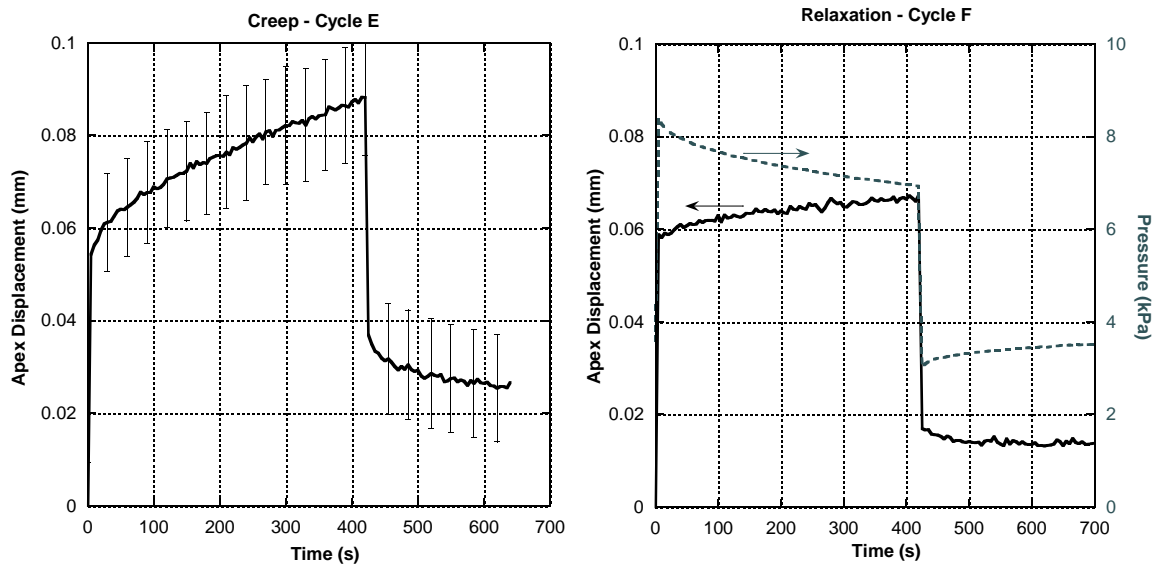


Figure 5.13. Creep and relaxation during cycles E and F, respectively.

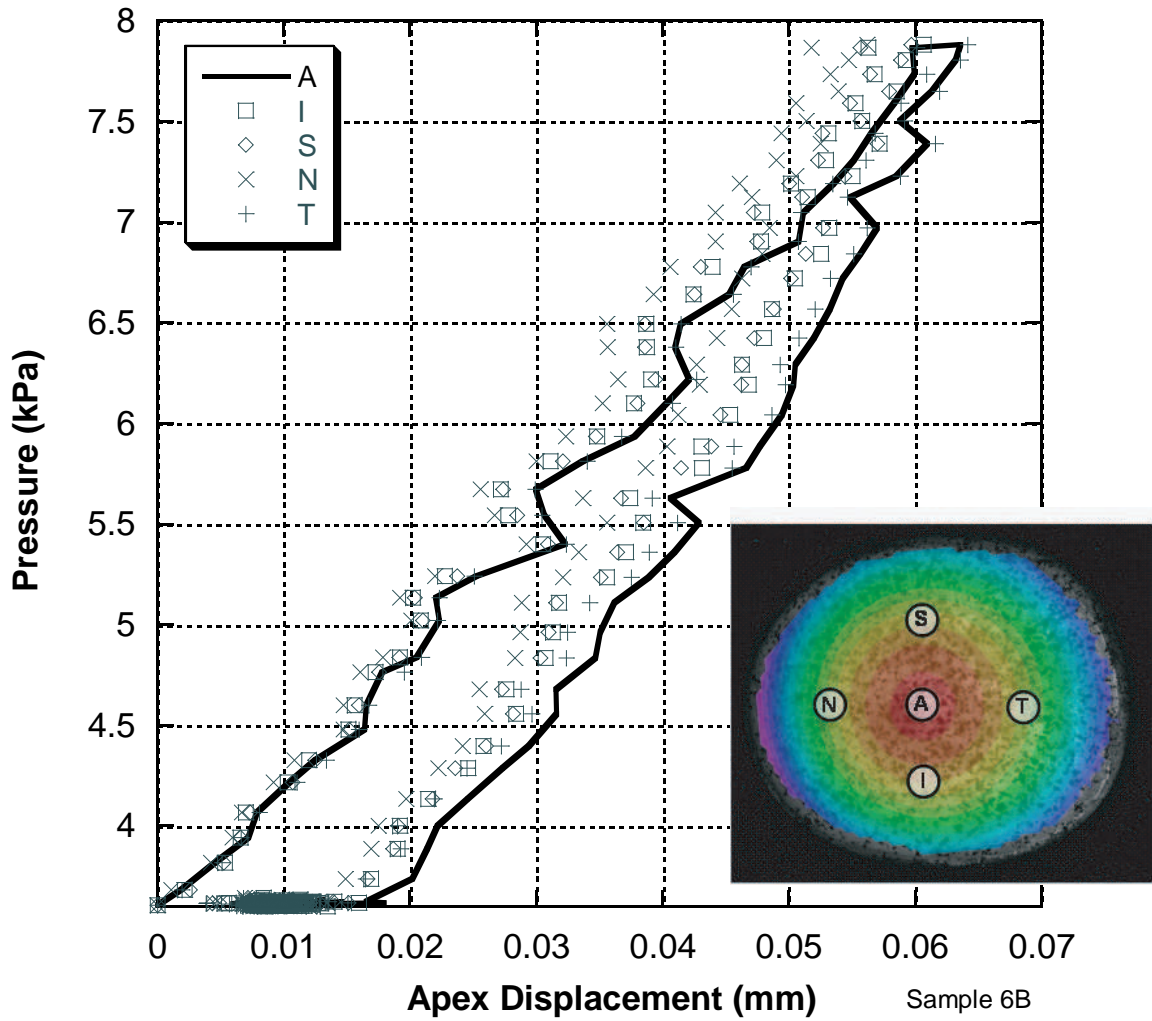


Figure 5.14. Local mid-periphery displacement values compared to the apex displacement.

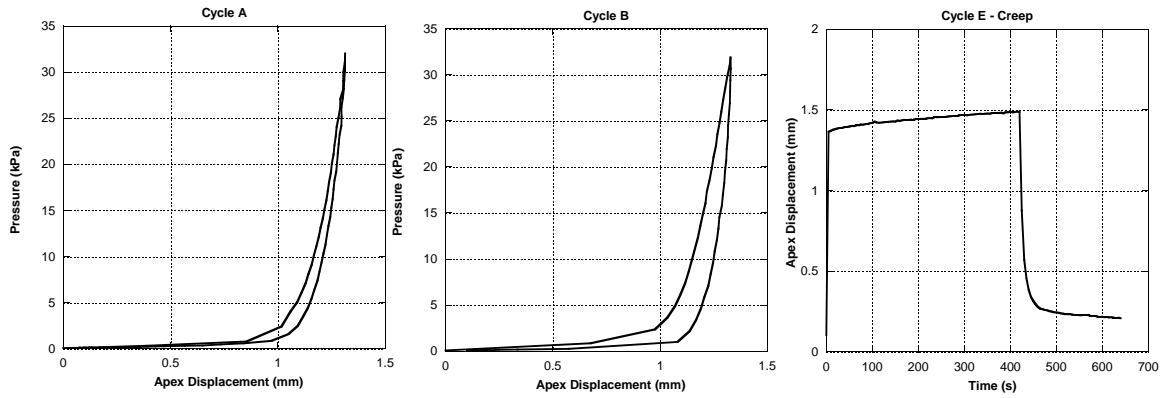


Figure 5.15. Response to pressures 0 – 32 kPa.

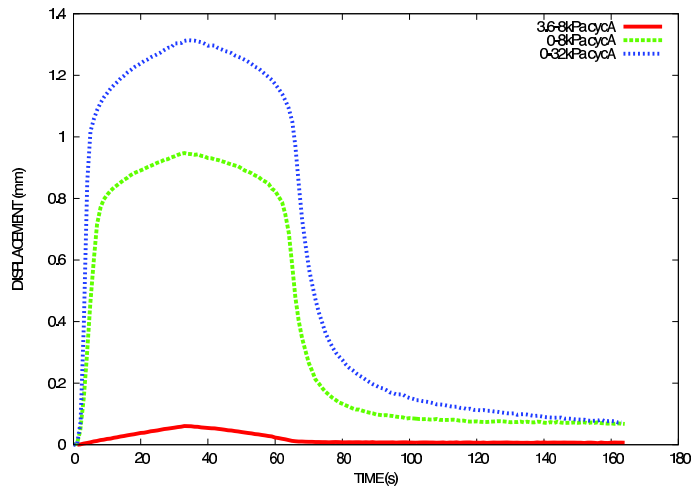


Figure 5.16. Comparison of the apex displacement for the three regimens.

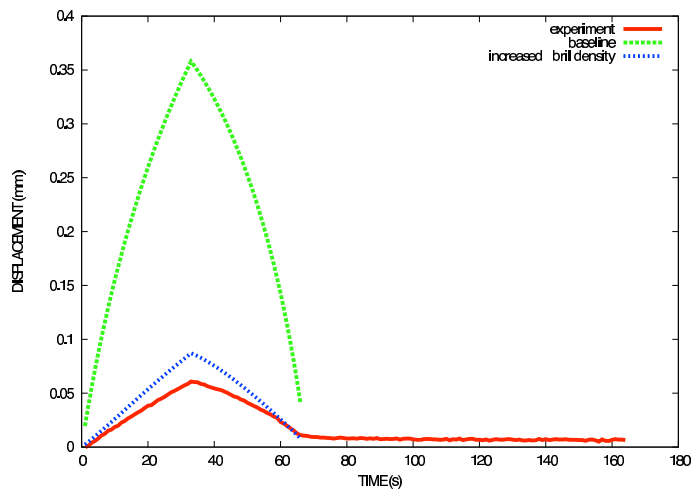


Figure 5.17. Comparison of the experimental apex displacement to the nominal model and one with increased fibril density.

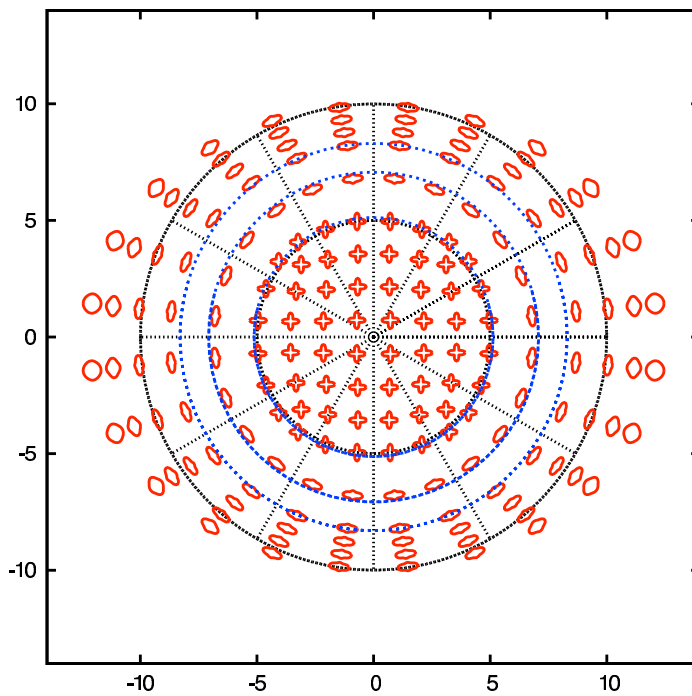


Figure 5.18. Fibril density at selected points across the cornea

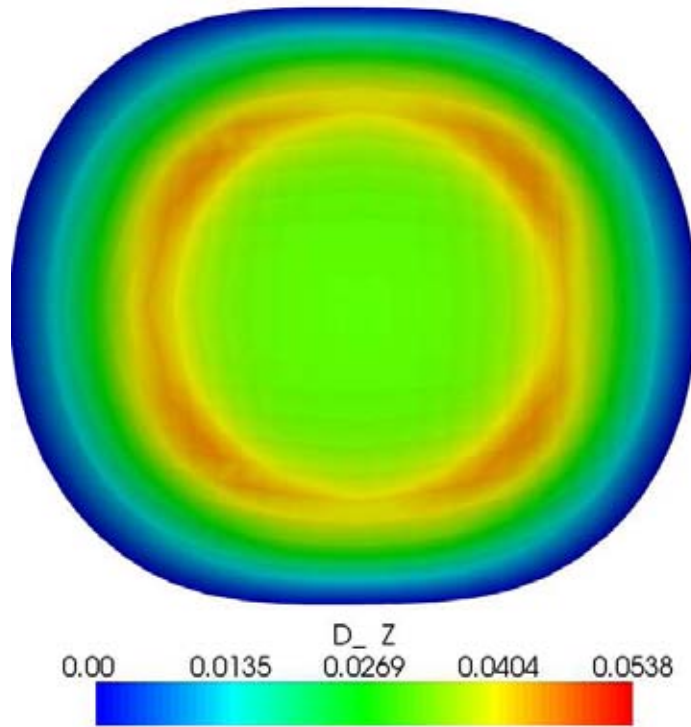


Figure 5.19. Simulated vertical displacements showing strong center cornea and relatively weak periphery

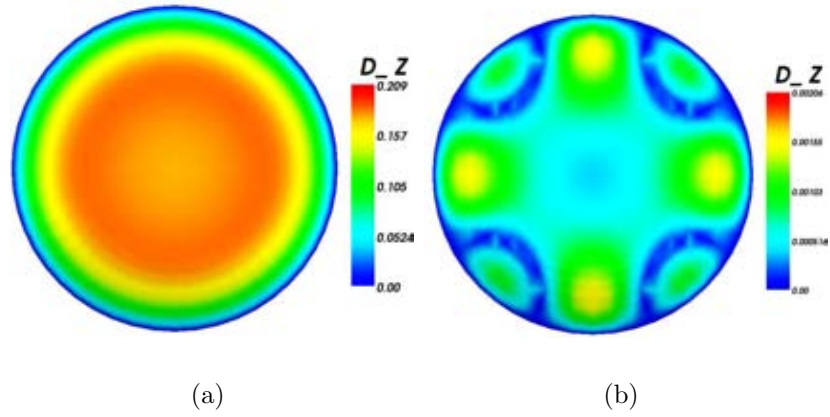


Figure 5.20. Displacements of the central region only: (a) total displacements for a primarily NT-IS oriented fibril density, and (b) the deviations of this deformation map with an isotropic (in-plane) arrangement of fibrils

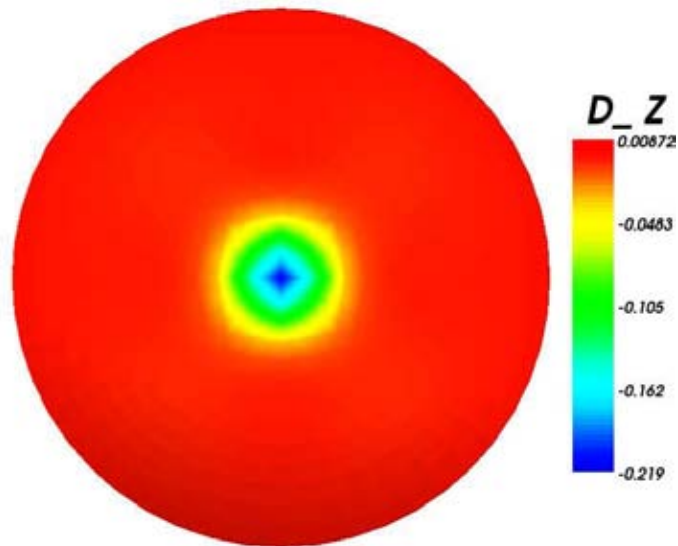


Figure 5.21. Applanation of a human cornea

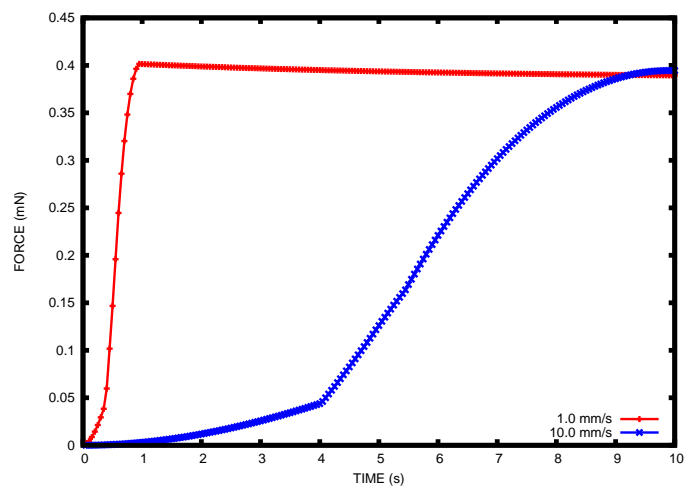


Figure 5.22. Applanation reaction force due to loading at 1.0 mm/s and 10.0 mm/s .

References

- [1] H. Aghamohammadzadeh, R. H. Newton, and K. M. Meek. X-ray scattering used to map the preferred collagen orientation in the human cornea and limbus. Structure, 12:249–256, 2005.
- [2] T. T. Andreassen, A. H. Simonsen, and H. Oxlund. Biomechanical properties of keratoconous and normal corneas. Experimental Eye Research, 31:435–441, 1980.
- [3] T. T. Andreassen, A. H. Simonsen, and H. Oxlund. Biomechanical properties of keratoconus and normal corneas. Experimental Eye Research, 31(4):435 – 441, 1980.
- [4] E. M. Arruda and M.C. Boyce. A three-dimensional constitutive model for the large stretch behavior of rubber elastic materials. J. Mech. Phys. Solids, 41:389–412, 1993.
- [5] J. S. Bergstrom and M.C. Boyce. Constitutive modeling of the large strain time-dependent behavior of elastomers. J. Mech. Phys. Solids, 46:931–954, 1998.
- [6] J.S. Bergstrom and M.C. Boyce. Constitutive modeling of the time-dependent and cyclic loading of elastomers and application to soft biological tissues. Mechanics of Materials, 3:523–530, 2001.
- [7] J. E. Bischoff, E. M. Arruda, and K. Grosh. A microstructurally based orthotropic hyperelastic constitutive law. Trans. ASME, J. App. Mech., 69:570–579, 2002.
- [8] J. E. Bischoff, E. M. Arruda, and K. Grosh. A rheological network model for the continuum anisotropic and viscoelastic behavior of soft tissue. Biomechanics and Modeling in Mechanobiology, 3:56–65, 2004.
- [9] J.P. Boehler. On irreducible representations for isotropic functions. Zeitschrift für Angewandte Mathematik und Mechanik, 57:323–327, 1977.
- [10] J.P. Boehler. A simple derivation of representation for non-polynomial constitutive equations in some cases of anisotropy. Zeitschrift für Angewandte Mathematik und Mechanik, 59:157–167, 1979.
- [11] C. Boote, S. Dennis, Y. Huang, A. Quantock, and K. M. Meek. Lamellar orientation in human cornea in relation to mechanical properties. J. Struct. Bio., 149:1 – 6, 2005.

- [12] C. Boote, S. Dennis, and K. M. Meek. Spatial mapping of collagen fibril organisation in primate cornea - an x-ray diffraction investigation. J. Struct. Biol., 146:359–267, 2004.
- [13] C. Boote, S. Dennis, R.H. Newton, H. Puri, and K. M. Meek. Collagen fibrils appear more closely packed in the prepupillary cornea: optical and biomechanical implications. Invest. Ophthalmol. Vis. Sci., 44:2941–2948, 2003.
- [14] B. L. Boyce, R. E. Jones, and T. D. Nguyen. Nonlinear tensile viscoelastic behavior of bovine cornea. J. Biomech., 2006. Accepted for publication.
- [15] B.L. Boyce, P.L. Reu, and C.V. Robino. The constitutive behavior of laser welds in 304l stainless steel determined by digital image correlation. Metall. Mater. Trans. A, 37A(7):2481–2492, 2006.
- [16] M. R. Bryant and P. J. McDonnell. Constitutive laws for biomechanical modeling of refractive surgery. Trans. ASME, J. Biomech. Eng., 118(4):473 – 81, Nov 1996.
- [17] K. A. Buzard. Introduction to biomechanics of the cornea. Refract. Corneal Surg., 8:127138, 1992.
- [18] E. O. Carew, A. Garg, J. E. Barber, and I. Vesely. Stress relaxation preconditioning of porcine aortic valves. Annals of Biomedical Engineering, 32(4):563 – 72, 2004.
- [19] D. G. Cogan. Applied anatomy and physiology of the cornea. Trans. Am. Acad. Ophthalmol., 55:329, 1951.
- [20] B. D. Coleman and M. E. Gurtin. Thermodynamics with internal state variables. Journal of Chemical Physics, 47:597–613, 1967.
- [21] A. Daxer and P. Fratzl. Collagen fibril orientation in the corneal stroma and its implications in keratoconus. Investigative Ophthalmology and Visual Science, 38:121–129, 1997.
- [22] T. C. Doehring, E. O. Carew, and I. Vesely. The effect of strain rate on the viscoelastic response of aortic valve tissue: a direct-fit approach. Annals of Biomedical Engineering, 32(2):223 – 32, 2004.
- [23] L. J. M. G. Dortmans, A. A. H. J. Sauren, and E. P. M. Rousseau. Parameter estimation using the quasi-linear viscoelastic model proposed by Fung. Trans. ASME, J. Biomech. Eng., 106(3):198 – 203, 1984.
- [24] D. M Elliott, P. S. Robinson, J. A. Gimbel, J. J. Sarver, J. A. Abboud, R. V. Iozzo, and L. J. Soslowsky. Effect of altered matrix proteins on quasilinear viscoelastic properties in transgenic mouse tail tendons. Annals of Biomedical Engineering, 31:599–605, 2003.

- [25] A. Elsheikh and K. Anderson. Comparative study of corneal strip extensometry and inflation tests. Journal of the Royal Society Interface, 2(3):177 – 85, 2005.
- [26] J. L. Ericksen and R. S. Rivlin. Large elastic deformations of homogeneous anisotropic materials. Archives of Rational Mechanics Analysis, 3:281–301, 1954.
- [27] P. J. Flory. Thermodynamic relations for highly elastic materials. Transactions of the Faraday Society, 57:829–838, 1961.
- [28] Y. C. Fung. Biomechanics: mechanical properties of living tissues. Springer-Verlag, New York, NY, second edition, 1993.
- [29] S. Govindjee and S. Reese. A presentation and comparison of two large deformation viscoelasticity models. Trans. ASME, J. Eng. Mater. Technol., 119:251–255, 1997.
- [30] M. S. Green and A. V. Tobolsky. A new approach to the theory of relaxing polymeric media. J. Comp. Phys., 14:80–92, 1946.
- [31] F. A. Guarnieri. Modelo biomechanico del ojo para diseno asistido por computadora de la cirurgua refractiva. Universidad Nacional del Litoral, Santa Fe, Argentina, 1999. Ph.D. Thesis.
- [32] J. Helm, S. McNeill, and M. Sutton. Three-dimensional image correlation for surface displacement measurement. Optical Eng., 35(7):1911–1920, 1996.
- [33] R. V. Hingorani, P. P. Provenzano, R. S. Lakes, A. Escarcega, and R. Vanderby Jr. Nonlinear viscoelasticity in rabbit medial collateral ligament. Ann. Biomedical Eng., 32(2):306–312, 2004.
- [34] J. O. Hjortdal. Regional elastic performance of the human cornea. J. Biomechanics, 29(7):931–942, 1996.
- [35] D. A. Hoeltzel, P. Altman, K. Buzard, and K. I. Choe. Strip extensometry for comparison of the mechanical response of bovine, rabbit, and human corneas. Trans. ASME, J. Biomech. Eng., 114(2):202 – 15, 1992.
- [36] D. A. Hoeltzel, P. Altman, K. Buzard, and K. I. Choe. Strip extensometry for comparison of the mechanical response of bovine, rabbit, and human corneas. Trans. ASME, J. Biomech. Eng., 114:202–215, 1992.
- [37] G. A. Holzapfel. On large strain viscoelasticity: continuum formulation and finite element applications to elastomeric structures. Int. J. Numer. Methods Eng., 39:3903–3926, 1996.
- [38] G. A. Holzapfel. Nonlinear solid mechanics: a continuum approach for engineers. John Wiley and Sons, LTD, Chichester, 2000.
- [39] G. A. Holzapfel and T. C. Gasser. A new constitutive framework for arterial wall mechanics and a comparative study of material models. J. Elast., 61:1–48, 2000.

- [40] G.A. Holzapfel, T.C. Gasser, and M. Stadler. A structural model for the viscoelastic behavior of arterial walls: Continuum formulation and finite element analysis. European Journal of Mechanics A/Solids, 21:441–463, 2002.
- [41] C. Y. Huang, V. C. Mow, and G. A. Ateshian. The role of flow-independent viscoelasticity in the biphasic tensile and compressive response of articular cartilage. Trans. ASME, J. Biomech. Eng., 123:410–417, 2001.
- [42] K. Huang. On the atomistic theory of elasticity. Proc. R. Soc. Lond. A, Math. Phys. Eng. Sci., 203:178–194, 1950.
- [43] D. W. L. Hukins. Collagen orientation. In D. W. L. Hukins, editor, Connective Tissue Matrix, volume 5, pages 212–240. Macmillan, London, 1984.
- [44] W. Jue and D. M. Maurice. The mechanical properties of the rabbit and human cornea. J. Biomech., 24:907–922, 1991.
- [45] J. Kampmeier, B. Radt, R. Birngruber, and R. Brinkmann. Thermal and biomechanical parameters of porcine cornea. Cornea, 19(3):355 – 363, 2000.
- [46] J. Kampmeier, B. Radt, R. Birngruber, and R. Brinkmann. Thermal and biomechanical parameters of porcine cornea. Cornea, 19:355–363, 2000.
- [47] J. C. Kennedy, R. J. Hawkins, R. B. Willis, and K. D. Danylchuk. Tension studies of human knee ligaments. J. Bone and Joint Surgery, 58A:350–355, 1976.
- [48] S. Klinkel, C. Sansour, and W. Wagner. An anisotropic fiber-matrix material model at finite elastic-plastic strains. Computational Mechanics, 35:409–417, 2005.
- [49] Y. Komai and T. Ushiki. The three-dimensional organisation of collagen fibrils in the human cornea and sclera. Investigative Ophthalmology and Visual Science, 32:2244–2258, 1991.
- [50] Y. Lanir. Constitutive Equations for Fibrous Connective Tissues. J. Biomech., 16:1–12, 1983.
- [51] J. Liao and I. Vesely. Relationship between collagen fibrils, glycosaminoglycans, and stress relaxation in mitral valve chordae tendineae. Journal of Biomedical Engineering, 2004:977–983, 2004.
- [52] G. Limbert and J. Middleton. A transversely isotropic viscohyperelastic material: Application to the modeling of biological soft connective tissues. Int. J. Solids Struct., 2004:4237–4260, 2004.
- [53] A. Lion. A constitutive model for carbon black filled rubber. Experimental investigations and mathematical representations. Continuum Mechanics and Thermodynamics, 8:153–169, 1996.

- [54] S. Liu. On representations of anisotropic invariants. International Journal of Engineering Science, 20:1099–1109, 1982.
- [55] J. Lubliner. A model of rubber viscoelasticity. Mechanics Research Communications, 12:93–99, 1985.
- [56] D. M. Maurice. The structure and transparency of the cornea. J. Physiol., 136:263–286, 1957.
- [57] D. M. Maurice. The cornea and sclera. In H. Davson, editor, The eye, pages 1–158. Academic Press, New York, New York, 1984.
- [58] K. M. Meek, T. Blamires, G. F. Elliott, T. J. Gyi, and C. Nave. The organization of collagen fibrils in the human corneal stroma: a synchrotron x-ray diffraction study. Current Eye Res., 6:841 – 846, 1987.
- [59] J. Merodio and R. W. Ogden. Mechanical response of fiber-reinforced incompressible non-linearly elastic solids. International Journal of Non-Linear Mechanics, 40:213–227, 2005.
- [60] K. Misof, G. Rapp, and P. Fratzl. A new molecular model for collagen elasticity based on synchrotron X-Ray scattering evidence. Biophys. J., 72:1376–1381, 1997.
- [61] H. K. P. Neubert. A simple model representing internal damping in solid materials. Aeronautical Quarterly, 14(2):187 – 210, 1963.
- [62] T. D. Nguyen, B. L. Boyce, and R. E. Jones. A nonlinear viscoelastic model for the tensile behavior of bovine cornea. ASME J. Biomech. Eng. (submitted), 2007.
- [63] T. D. Nguyen, S. Govindjee, Kleinm P. A., and H. Gao. A rate-dependent cohesive continuum model for crack dynamics. Comp. Meth. App. Mech. Engr., 193:3239–3265, 2004.
- [64] G. W. Nyquist. Rheology of the cornea: experimental techniques and results. Exp. Eye Res., 7:183–188, 1968.
- [65] R. W. Ogden. Nearly isochoric elastic deformations: application to rubber-like solids. J. Mech. Phys. Solids, 26:37–57, 1978.
- [66] R. W. Ogden. Non-linear Elastic Deformations. Dover Publications, Inc, Mineola, New York, 1997.
- [67] A. Pandolfi and F. Manganiello. A model for the human cornea: constitutive formulation and numerical analysis. Biomechanics and Modeling in Mechanobiology, 2006. In press.
- [68] P. M. Pinsky and D. V. Datye. A microstructurally-based finite element model of the incised human cornea. J. Biomech., 24:907–922, 1991.

- [69] P. M. Pinsky, D. van der Heide, and D. Chernyak. Computational modeling of mechanical anisotropy in the cornea and sclera. Journal of Cataract and Refractive Surgery, 31:136–145, 2005.
- [70] D. P. Pioletti, L. R. Rakotomanana, J.-F. Benvenuti, and P.-F. Leyvraz. Viscoelastic constitutive law in large deformations: application to human knee ligaments and tendons. J. Biomechanics, 31:753–757, 1998.
- [71] P. P. Provenzano, R. Lakes, T. Keenan, and R. Vanderby. Nonlinear ligament viscoelasticity. Annals of Biomedical Engineering, 29:908–14, 2001.
- [72] R. Puxkandl, I. Zizak, O. Paris, J. Keckes, W. Tesch, S. Bernstorff, P. Purslow, and P. Fratzl. Viscoelastic properties of collagen: synchrotron radiation investigations and structural model. Philos. Trans. R. Soc. Lond. Ser. B-Biol. Sci., 357:191–197, 2002.
- [73] S. Reese. Meso-macro modelling of fibre-reinforced rubber-like composites exhibiting large elastoplastic deformation. Int. J. Solids Struct., 40:951–80, 2003.
- [74] S. Reese and S. Govindjee. A theory of finite viscoelasticity and numerical aspects. Int. J. Solids Struct., 35:3455–82, 1998.
- [75] Carlo Sansour and Jozef Bocko. On the numerical implications of multiplicative inelasticity with an anisotropic elastic constitutive law. Int. J. Numer. Methods Eng., 58:2131–2160, 2003.
- [76] AAH J. Sauren and E. P. M. Rousseau. A concise sensitivity analysis of the quasi-linear viscoelastic model proposed by Fung. Trans. ASME, J. Biomech. Eng., 105(1):92 – 5, 1983.
- [77] T. J. Shin, R. P. Vito, L. W. Johnson, and B. E. McCarey. The distribution of strain in the human cornea. J. Biomech., 30(5):497–503, 1997.
- [78] J. C. Simo, R. L. Taylor, and K. S. Pister. Variational and projection methods for the volume constraint in finite deformation elasto-plasticity. Comp. Meth. App. Mech. Engr., 51:177–208, 1985.
- [79] A. J. M. Spencer. Theory of invariants. In A.C. Eringen, editor, Continuum Physics, volume I, pages 239–353. Academic Press, New York, 1971.
- [80] E. Spoerl, M. Huhle, and T. Seiler. Induction of cross-links in cornea tissue. Exp. Eye Res., 66:97–103, 1998.
- [81] C. J. Stone. A Course In Probability and Statistics. Duxbury Press, Belmont, CA, first edition, 1995.
- [82] A. Sverdlik and Y. Lanir. Time-dependent mechanical behavior of sheep digital tendons, including the effects of preconditioning. Trans. ASME, J. Biomech. Eng., 124(1):78 – 84, 2002.

- [83] D. R. Veronda and R.A. Westmann. Mechanical characterization of skin - finite deformation. J. Biomech., 3:11–124, 1970.
- [84] C. C. Wang. On a general representation theorem for constitutive relations. Archives of Rational Mechanics Analysis, 33:1–25, 1969.
- [85] J. A. Weiss, J. C. Gardiner, and C. Bonifasi-Lista. Ligament material behavior is nonlinear, viscoelastic and rate-independent under shear loading. J. Biomechanics, 35:943–950, 2002.
- [86] G. Wollensak, E. Spoerl, and T. Seiler. Stress-strain measurements of human and porcine corneas after riboflavin-ultraviolet-a-induced cross-linking. Journal of Cataract and Refractive Surgery, 29(9):1780 – 1785, 2003.
- [87] G. Wollensak, E. Spoerl, and T. Seiler. Stress-strain measurements of human and porcine corneas after riboflavin-ultraviolet-a-induced cross-linking. Journal of Cataract and Refractive Surgery, 29:1780–1785, 2003.
- [88] S. L.-Y. Woo, A. S. Kobayashi, W. A. Schlegel, and C. Lawrence. Nonlinear material properties of intact cornea and sclera. Exp. Eye Res., 14:29–39, 1972.
- [89] Y. J. Zeng, J. Yang, K. Huang, Z. H. Lee, and X. Y. Lee. A comparison of biomechanical properties between human and porcine cornea. J. Biomechanics, 34:533 – 537, 2001.

This page intentionally left blank.

DISTRIBUTION:

- 1 Prof. R.A. Regueiro
Department of Civil, Environmental, and Architectural Engineering
1111 Engineering Dr.
428 UCB, ECOT 441
Boulder, CO 80309-0428

- 1 Prof. Thao Nyugen
Department of Mechanical Engineering
Whiting School of Mechanical Engineering
Johns Hopkins University
223 Latrobe Hall
3400 North Charles Street
Baltimore, Maryland 21218-2681

- 1 MS 9001
P.J. Hommert, 8000

- 1 MS 9405
R.W. Carling, 8700

- 1 MS 0885
D.B. Dimos, 1800

- 1 MS 9004
J.M. Hruby, 8100

- 1 MS 9153
C.L. Knapp, 8200

- 1 MS 9001
P.A. Spence, 8000

- 1 MS 0885
J.E. Johannes, 1810

- 1 MS 9404
D.M. Kwon, 8770

- 1 MS 9161
A.E. Pontau, 8750

- 1 MS 9042
E.P. Chen, 8776

- 1 MS 9042
M.L. Chiesa, 8774
- 1 MS 0889
J.S. Custer, 1824
- 1 MS 9409
C.D. Moen, 8757
- 7 MS 0889
B.L. Boyce, 1824
- 3 MS 0889
J.M. Grazier, 1824
- 3 MS 9409
R.E. Jones, 8776
- 1 MS 9018
Central Technical Files, 8944 (electronic copy)
- 1 MS 0899
Technical Library, 9536 (electronic copy)
- 1 MS 0123
D. Chavez, LDRD Office, 1011